

AITN014PJM Canard Design Notes

The purpose of this study:



Minimising the drag of a land speed record vehicle is a critical element in the attainment of the record. Apart from aerodynamic drag there is also rolling resistance, and this can be quite considerable. It was a primary reason why the Thrust SSC with nearly 40,000 lbs thrust only just managed to break the sound barrier. The rolling resistance is a function of the vehicle mass and the surface that upon it travels. Vehicles are heavy the A15R is expected to have a mass more than 9 tonnes. The form of the vehicle will create lift or downforce depending upon its relative angle of attack to the airflow. Too negative and the effect will be for the vehicle to plough itself into the ground, too positive and it will tend to lift off. There is a balancing act to achieve during the vehicle setup. That set up also has to take into account transient effects. One of those effects is the deployment of the airbrakes. This is set to occur progressively from the moment the run has been completed though the full deployment angle of around 60 degrees isn't planned until the vehicle reduces in velocity to Mach 0.9.

Because of the height of the airbrakes that deployment sets up a pitching moment that tends to lift the nose. If the vehicle is set at a marginal angle of attack to minimise the resultant vertical force then during braking the moment could be sufficient to cause the nose to rise sufficiently to cause the vehicle to flip. A canard wing at the front of the vehicle offers a method to overcome this braking induced moment. The required angle to achieve this is about 8 degrees negative, but if this is kept as a constant angle then at supersonic velocities (when the airbrakes aren't deployed) the force becomes excess and nose wheel ploughing becomes a risk. So the requirement is a canard that's angle of attack changes. Moving aerodynamic surfaces aren't strictly allowed and driver adjustments during the record mile run prohibited. Realistically as that mile is achieved in under 4 seconds, it is impossible.

The solution is to use a floating canard arrangement and use known aerodynamic effects to one's advantage. As the velocity of the free stream approaches and passes through the speed of sound, the centre of pressure of the wing moves rearward. It is called Mach tuck. A characteristic of a delta planform is a smooth rearward movement (Figure 1) of the centre of pressure. So if the canard has its pivot point ahead of the centre of pressure then as the velocity increases the moment twisting it about the axis increases.

If on the trailing edge of the canard a small flap is added (Gurney) in a direction that opposes the moment created by the centre of pressure then the moments that they create work against each other.

If the gurney is on the underside on the canard and the canard set at a negative angle of attack to the airflow then the nett results are:

At transonic velocities, the steady state angle of attack is at its minimum, and as the velocity reduces, so the angle of attack reduces, i.e., it becomes more negative.

This report is the record of the study of that solution. The canard is counter-weighted, it is dampened and has a limited range of movement. All of which is intended to be adjustable, because in reality there are so many assumptions made on an incomplete design it would be unwise to do otherwise.

The operation is represented in Figure 2.

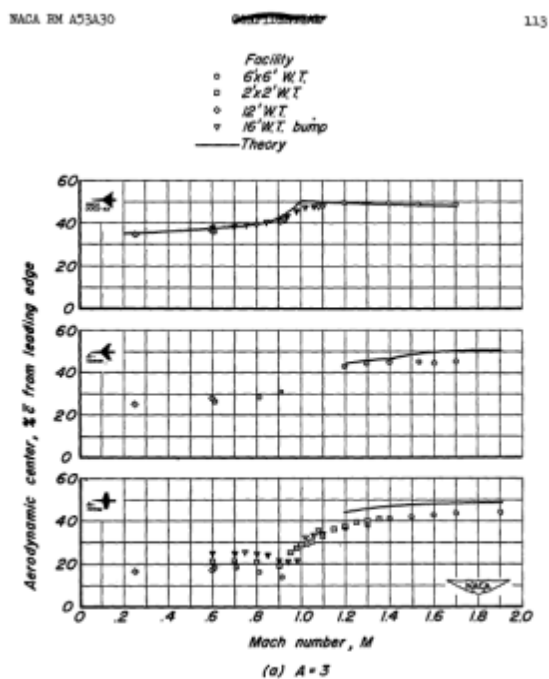


Figure 15.—The aerodynamic center for plane wings 3 percent thick and having different types of plan form.

Figure 1 Showing centre of pressure movement with Mach number for various plan-forms

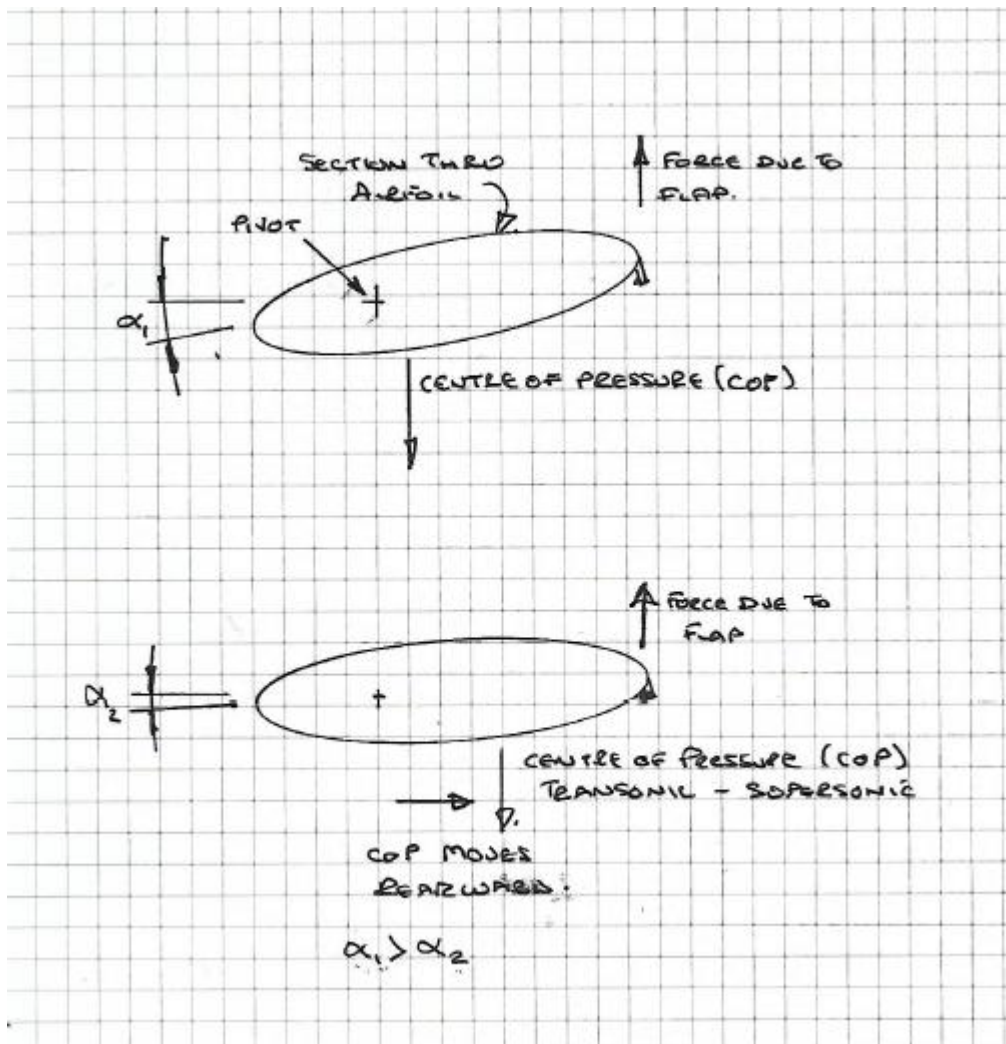


Figure 2 Showing the angle of attack changed as a result of the rearwards movement of CoP.

Introduction

Inevitably, when developing any world leading venture with limited resources, the trade-off tends to be time and scope. Previous experiences with other aero features of the vehicle lead to the conclusion that there may be a significant gestation period before this structure is manufactured and installed, these notes have been created to capture the salient decisions and their reasons during the design process of the canard. Issued as a draft version because there is detailed packaging work that will result in some dimensional changes.

Canard's purpose;

The canard is a multifunctional device.

Its primary function is to generate a downforce at the front of the vehicle that forms an opposing moment to that created by the aerodynamic drag experienced during deceleration. The downforce should thus be sufficient so that the load on the front wheels is not adversely affected to the degree that compromises stability.

The canard for the AI5R will see the highest changes in the angle of attack which will be negative and circa 8 degrees (see Appendix A), and this will be transitional. It is dependent upon the instantaneous airbrake deployment angle and velocity at the time. It is assumed that maximum deployment occurs in the subsonic velocity range, specifically $< M 0.9$.

The canard's secondary function is to "tune" the front to rear downforce split driven primarily by the tailplane incidence and will see a permanent set. Achieved using an aero device or through a locked angle mechanism, or counterbalancing or a mixture of two or more.

Its tertiary function is to assist in maintaining a level trajectory, without pilot input, during the qualifying run distance.

The existence of a canard has some negative effects.

- It potentially moves the centre of pressure of the whole system forward. For pitch stability, the optimum situation is to have the centre of pressure rearward of the centre of gravity (Figure 3).
- A fixed canard contributes to the overall lift coefficient rate (CL/α) of the vehicle. This means if the vehicle angle changes either positively or negatively the lift of the canard changes proportionally. It has no dampening effect. If it floats, which is a common technique used on high manoeuvrability fighter aircraft (but not limited to them), see Figure 4, a CL value may be set so that the CL contribution can be utilised, but the CL/α contribution can be zero. This report details the design of a floating canard.

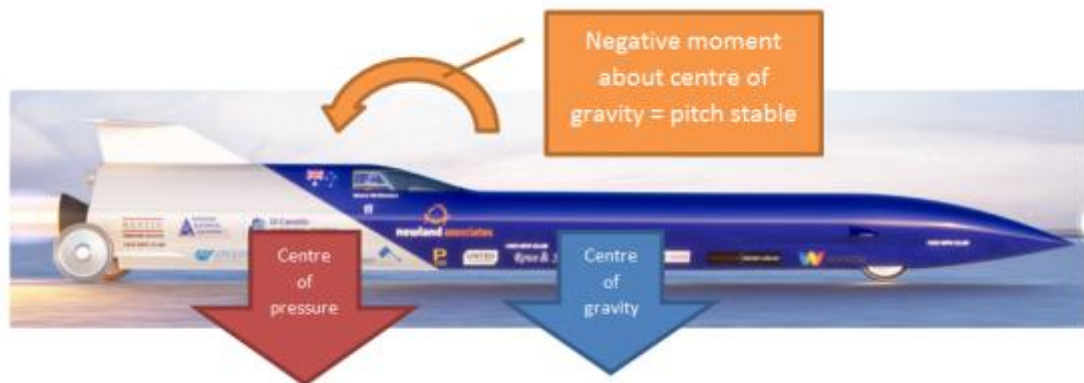


Figure 3 showing ideal centre of pressure /centre of gravity relationship. ERRATUM>>> Negative moment should say Positive.

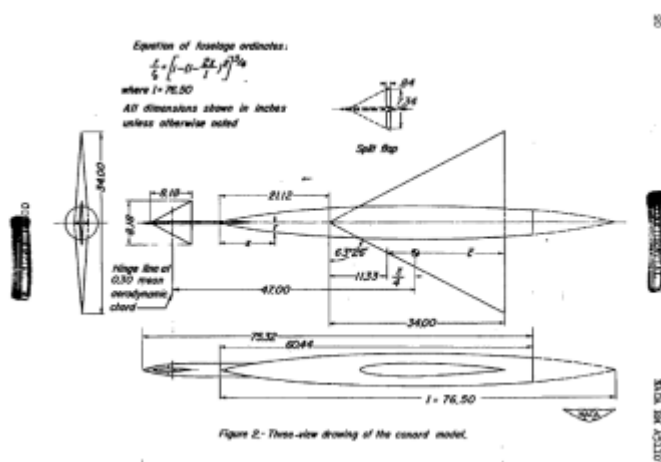


Figure 4 showing floating canard arrangement on NACA model circa 1950

Initial sizing.

The primary factor in determining size was the constraint of the tailplane. Specifically, its area and the relative moment arm from the centre of gravity and centre of pressure. Designing any wing is an iterative process, with effect felt upstream and downstream in the design process and, this sizing only sets the start point.

In the case of the plan area, a reference to Tom Morel's work on Blue Flame suggested he was looking for a canard area of 0.168 the nose cone base area which was probably about right when the lift from the suspension struts was taken into consideration. Ignoring the effect of other elements of the vehicle

such as the body wheels etc., the sizing equations (Figure 7 and Figure 8) were used for design point calculations. These are sizing tools used for aircraft, and so it was considered a reasonable place to start. The results are summarised in Figure 9. Factors that are likely to vary include, the lift coefficient of the wings and their relative areas. Centre of gravity of the vehicle was taken initially as a 50/50 split. All of these will change. The lift coefficients will rise disproportionately up to Mach 1 and then tend to drop off again. The vehicle mass will change as fuel is spent and the split will alter.

Parenthetically, these calculations also determine the maximum area of the canard in relation to the tailplane.

The goal is to ensure that the pitching moment rate ($C_{M/\alpha}$) remains negative. For an aircraft the for stability that a pilot can control easily, the value should be between $-0.025 < C_{M/\alpha} < -0.008$, but for LSR without pilot input, the goal is for it to be slightly negative.

This pitching coefficient is sensitive to velocity changes. The lift coefficient rate for the proposed delta canard was calculated at 0.06/ degree at M 0.7, 0.062/ degree at M 0.9 and 0.066/ degree at M 1.3. Going from M 0.7 to M 1.3 effectively reduces the pitching moment rate by 50%, i.e., the value calculated in Figure 9 of -0.101 would drop to -0.055, but that isn't the full picture. Mach 1.0 is a singularity and difficult to calculate the wing performance there. However, it is usually the peak point for lift coefficients, and as such it is most likely for the $C_{L/\alpha}$ value to be higher than that at M 1.3 and so erode this margin further.

An unfavourable rearward change in the centre of gravity of approximately 5% in split reduces the $C_{M/\alpha}$ value. It doesn't take many of this element to conspire together to reduce the $C_{M/\alpha}$ value to zero. But fortunately, there are other elements of the vehicle that can be tweaked to yield a stable solution. With so many unknowns, it is unwise to declare a "guaranteed" solution without shake-down tests. The caveat is that the proposed solution is highly tuneable and ultimately easy to replace with an alternative if required

Plan-form requirements

The basic shape of the plan-form is shown in Figure 10 from which it will be tugged, pulled, twisted and morphed into the final solution. To minimise wave drag, the aim was to have the leading edge angle less than the Mach cone angle M 1.3 see Figure 6.



Parenthetically, with $\tan \varepsilon = \tan (90-42.4) = 1.095$ and $\tan \mu = \tan 50.3 = 1.204$, $\tan \varepsilon / \tan \mu = 0.905$ suggesting the planform is 0.8 that of the 2-D supersonic value. This equates to $C_{L/\alpha}$ of 0.067/degree. ESDU graphs confirmed this with a value of 0.066 at M 1.3

In reality, the strong shockwave won't exist at the apex of the wing but detached from the nose of the vehicle which is at least 3.75 m away.

The canard centre of pressure movement through the whole speed range should tend rearwards. There should be no Mach or transonic tuck, this is a forward movement of the centre of pressure at transonic velocities, and this is achievable through sweepback.

To achieve the trailing edge requirement, the shape will trend towards a delta planform. A delta wing generates a significant proportion of its lift through the creation of a stable leading edge vortex. This is a function of the leading edge angle and velocity operating envelope. The canard wants to perform at its best at M 0.9 which would suggest a low degree of sweepback. However, as it operates in the transonic/ low supersonic range also the higher wave drag associated with supersonic leading edges should be avoided if possible. In the operating velocity range expected; the required vortex lift is achievable with a less than 50-degree leading edge sweep delta (Figure 5)

To minimise the wave drag the leading edge angle should be within the Mach cone minimum angle $\mu = \sin^{-1}(1/M)$ at M 1.3 this is 50 degrees measured from the chord centreline, i.e., a 40-degree leading edge sweep value. An allowance of +/- 2 degrees should be allowed for the possibility of vehicle yaw during a run.

The pivot point at the root needs to be as far forward of the centre of pressure panel to maximise the restoring moment of the floating panel.

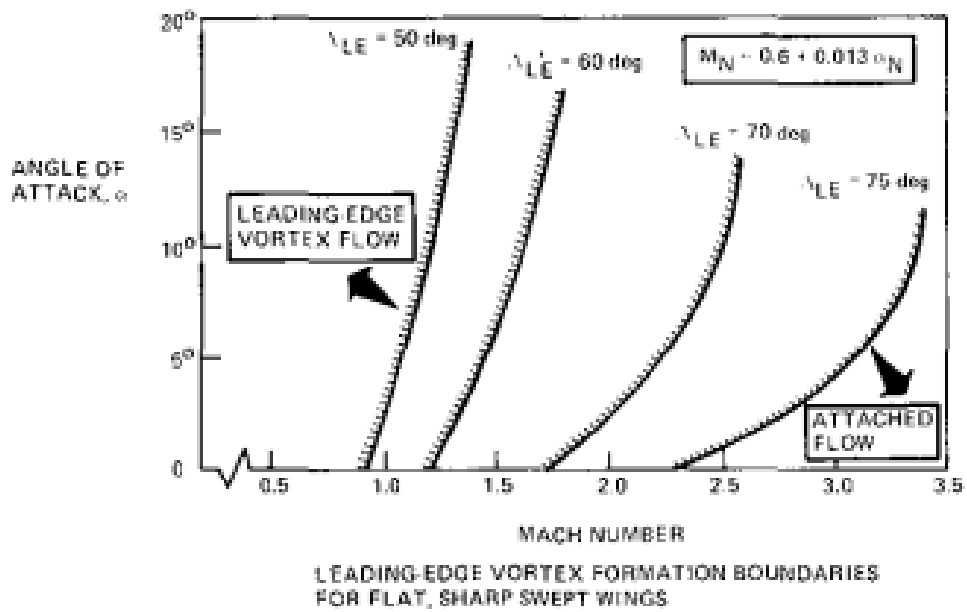
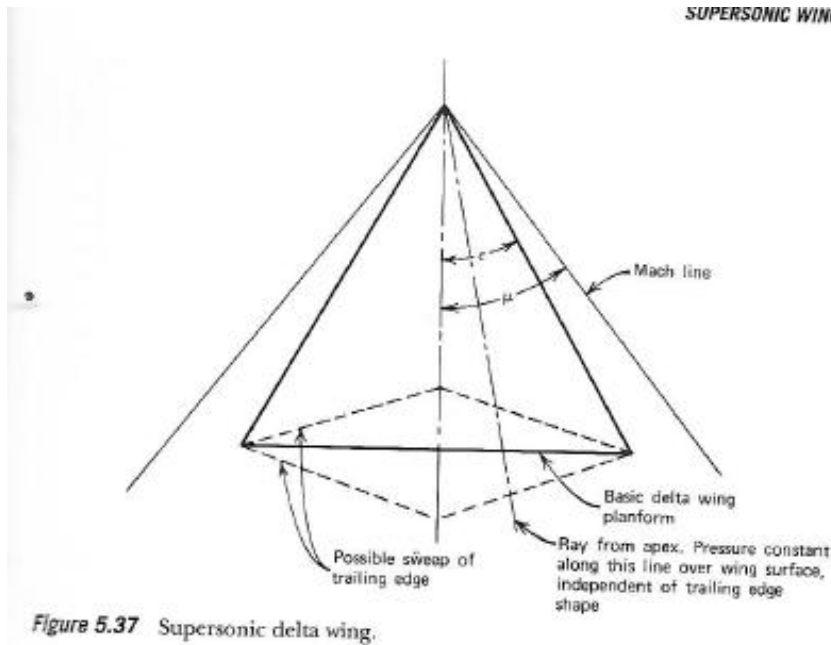


Figure 5 showing the effect of leading edge angle on leading edge vortex generation

SUPERSONIC WINGS 2



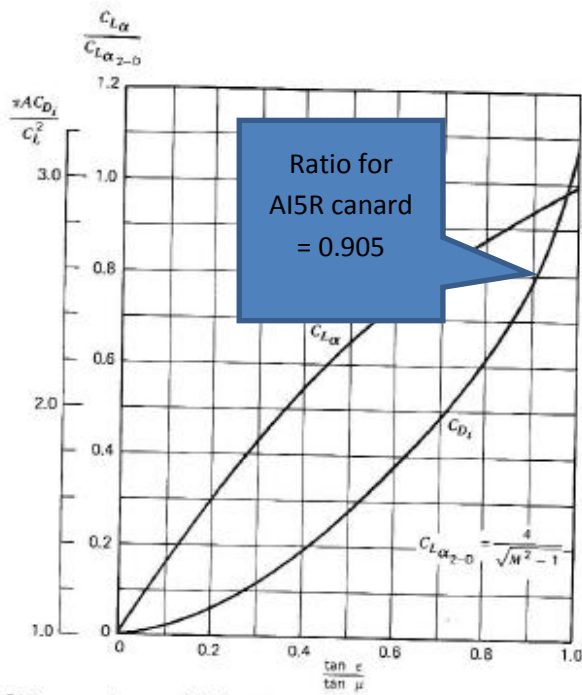


Figure 5.39 Lift curve slope and induced drag coefficient for delta wings with subsonic leading edges.

Figure 6. showing reasoning behind Canard leading edge angle being close to M 1.3 shockwave angle

Where: C_{m_0} = Coefficient of moment at zero AOA
 C_{m_α} = Change in coefficient of pitching moment due to AOA
 $C_{m_{\delta_e}}$ = Elevator authority; change in coefficient of pitching moment due to elevator deflection

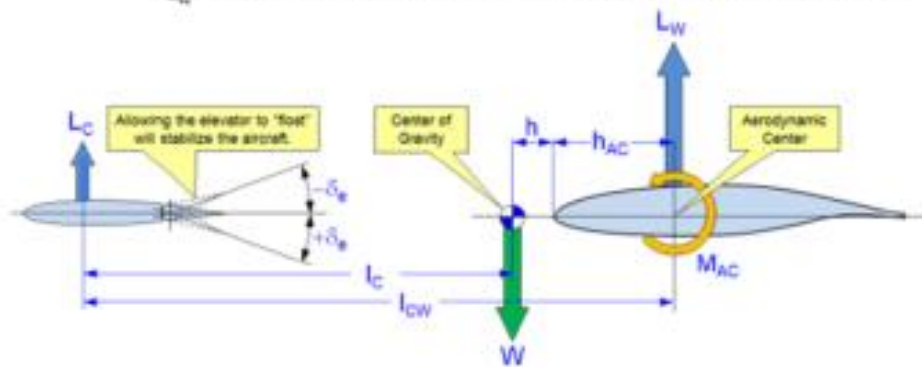


Figure C2-4: Wing-Canard system used to derive Equation (C2-4).

Both of the above terms can be determined for this system using the following expressions:

$$C_{m_0} = V_c \cdot C_{l_{\alpha_c}} + C_{m_{\alpha_c}} - C_{m_{\alpha_w}} \quad (C2-2)$$

$$C_{m_\alpha} = V_c \cdot C_{l_{\alpha_c}} + C_{m_{\alpha_c}} - \frac{(h_{AC} + h)}{C_{MGC}} C_{l_{\alpha_w}} \quad (C2-3)$$

Where: C_{MGC} = Mean Geometric Chord
 h_0 = Physical location of the CG at which $C_{m_0} = 0$; i.e. the stick-fixed neutral point
 h_{AC} = Physical location of the Aerodynamic Center
 l_c = Arm between the aerodynamic center of the canard and CG
 l_{CW} = Arm between the aerodynamic center of the canard and the wing
 S = Reference wing area
 S_c = Planform area of the canard
 V_c = Canard volume = $\frac{S_c \cdot l_c}{S \cdot C_{MGC}} = \frac{S_c \cdot (l_{CW} - h - h_{AC})}{S \cdot C_{MGC}}$
 $C_{m_{\alpha_c}}$ = Longitudinal stability contribution of components other than the wing
 $C_{m_{\alpha_w}} = C_{l_{\alpha_w}} (h_{AC} + h)$ = Wing pitching moment due to airfoil camber
 $C_{l_{\alpha_c}}$ = Canard lift coefficient at zero AOA
 $C_{m_{\alpha_c}}$ = Longitudinal stability contribution of components other than the wing
 $C_{l_{\alpha_c}}$ = Lift curve slope of the canard
 $C_{l_{\alpha_w}}$ = Wing lift curve slope

Figure 7 showing basic canard sizing formulae for aircraft

$$C_m = C_{m_0} + C_{m_\alpha} \cdot \alpha + C_{m_{\delta_e}} \cdot \delta_e$$

Figure 8 showing the governing moment equation

Canard	C_{MGC}	0.300	m					
Tailplane	C_{MGC}	0.540	m					
	h	5.510	m	weight distribution				
	h_{ac}	0.098	m					
	l_c	5.316	m	.6 m in front of RW centreline				
	l_{cw}	10.935	m					
	S	0.324	m ²					
	S_c	0.140	m ²	aspect ratio	2.57	fraction of base area	0.18	
	V_c	7.656	m ³			Blue Flame target	0.168	
	C_{moAC}	0.000						
	C_{moW}	0.000	bi convex					
	C_{LOC}	0.000						
	$C_{m\alpha AC}$	0.000						
	$C_{L\alpha C}$	0.060						
	$C_{L\alpha W}$	0.054	with endplates					
	C_{mo}	0.000		In practice, for human pilots to control with ease:				
	$C_{m\alpha}$	-0.101		$-0,025 \text{ deg}^{-1} < C_{M,\alpha} < -0,008 \text{ deg}^{-1}$				
	C_m	-0.101						

Figure 9 showing a summary of first pass calculations

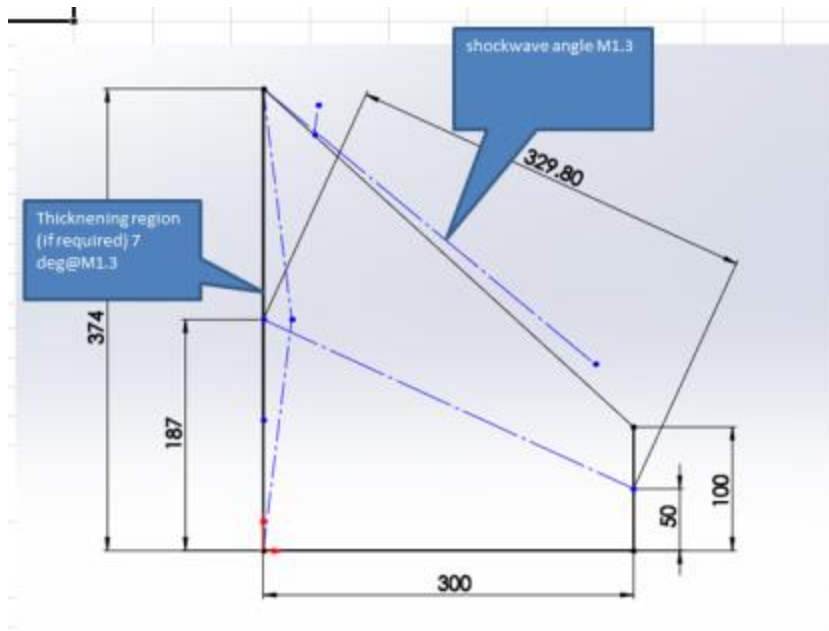


Figure 10 showing basic shape derived from first pass calculations

Determination of Panel Overall Lift Coefficients.

Three methods were used.

- A model was created (Figure 11) and analysed using a vortex lattice method. This yielded a CL/degree value of 0.048 (Figure 12).
- The second approach was to use the Polhamus method (Figure 13 and Figure 14) yielding a value of 0.045/ degree.

The above two methods do not correct for compressibility. The Prantl-Glauert method can be used, but it becomes increasingly less accurate as it predicts infinity at the M 1.0 singularity. At M 0.7 the error is likely to be low, and the correction factor $\sqrt{1/(1-M^2)}$ lifts the expectation of the values derived from the two previous approaches to between 0.063 and 0.067.

- The third method used was ESDU graphs this yielded a figure of 0.060 for M0.7 and 0.062 for M 0.9 (Figure 27 and Figure 28). These were the value used for future calculations.

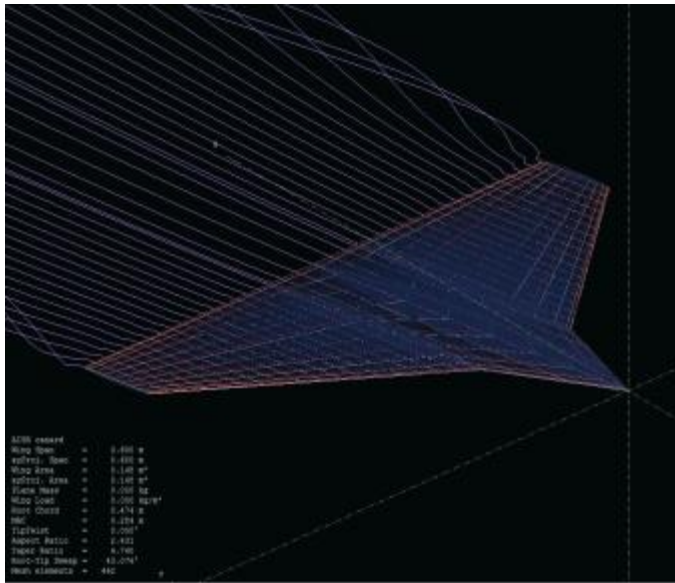


Figure 11 showing vortex lattice model

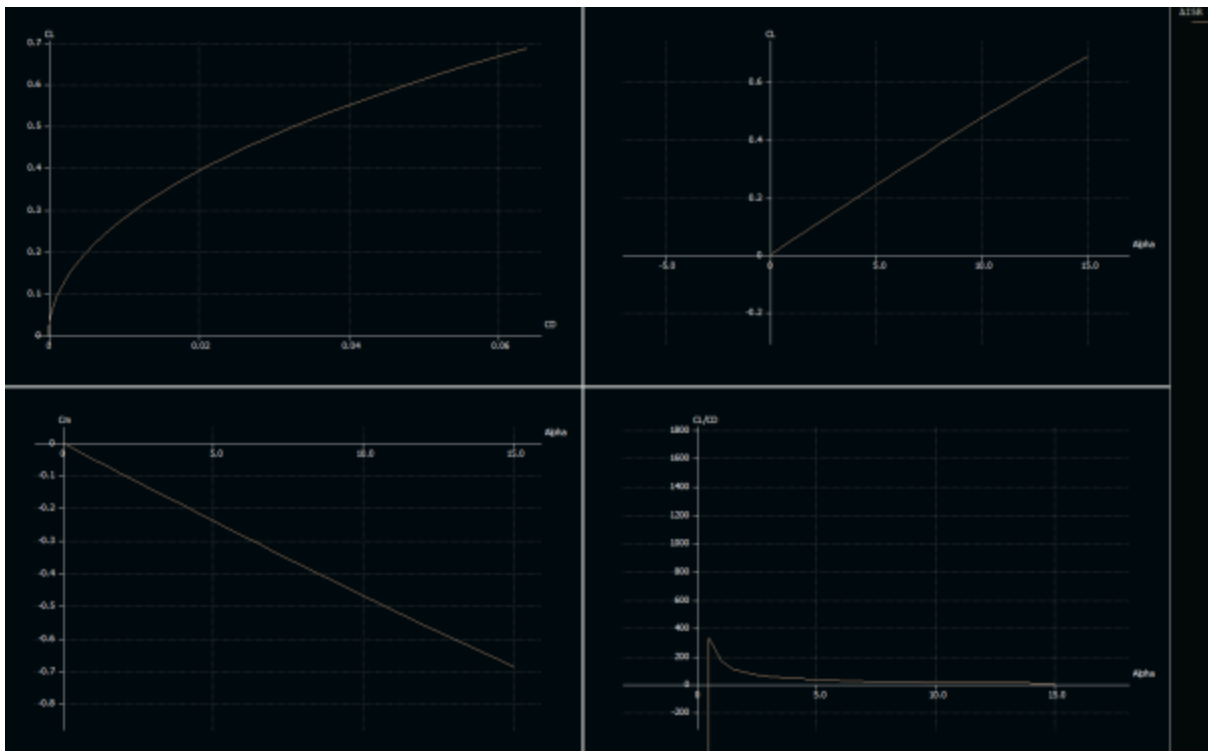


Figure 12 showing various output graphs from vortex lattice method including C_L vs. Angle Top RHS

Using Polhamus' Law						
$C_L = (\text{potential flow lift}) + (\text{vortex lift})$						
$C_L = K_p \sin \alpha \cos^2 \alpha + K_v \cos \alpha \sin^2 \alpha$						
the angle of attack α degrees		1	2	3	4	5
the angle of attack α radians		0.0175	0.0349	0.0524	0.0698	0.0873
$\sin \alpha$		0.0175	0.0349	0.0523	0.0698	0.0872
$\sin^2 \alpha$		0.0003	0.0012	0.0027	0.0049	0.0076
$\cos \alpha$		0.9998	0.9994	0.9986	0.9976	0.9962
$\cos^2 \alpha$		0.9997	0.9988	0.9973	0.9951	0.9924
K_p	AR = 2.57	2.5100	2.5100	2.5100	2.5100	2.5100
K_v	AR = 2.57	3.2000	3.2000	3.2000	3.2000	3.2000
C_L		0.0448	0.0914	0.1398	0.1898	0.2413
C_L/α Radians		2.565	2.618	2.669	2.718	2.765
C_L/α degrees		0.045	0.046	0.047	0.047	0.048

Figure 13 showing calculations using Polhamus rules

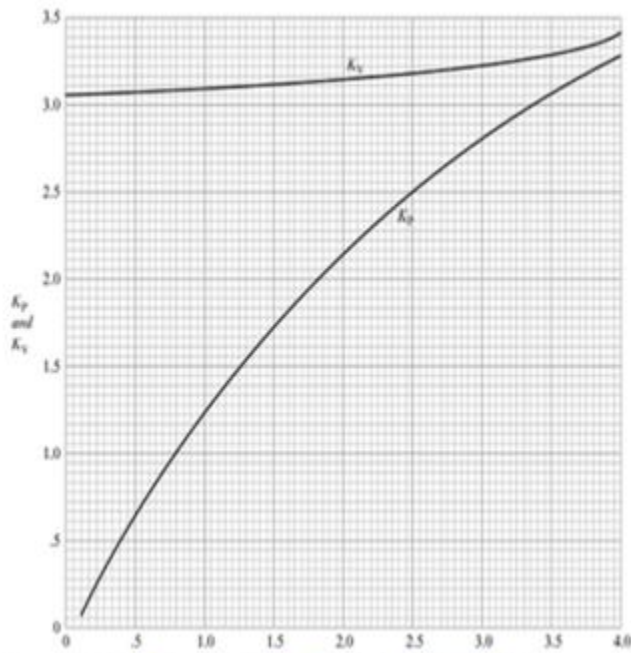


Figure 6.31. Values of K_p and K_v for a delta wing at $M=0$ (Polhamus, 1968).

Figure 14 showing Polhamus constants vs. aspect ratio using in calculations of Figure 13.

Sectional shape requirements for the canard.

- To adjust the floating angle of attack Gurney flaps of various heights may be used which are attached to the trailing edge. For example, a Gurney positioned on the underside (Figure 15) will result in an anticlockwise moment about the pivot point resulting in a negative angle of attack. If the canard centre of pressure is rearward of the trunnion pivot point, the negative angle of attack will create an opposing downforce and moment that will counteract and equalise the gurney induced moment. The result is the wing will take up a stable negative angle. This method is used on various aircraft (Figure 16) though, in such cases, the control mechanism is such that the pilot can adjust the pitch of the tailplane during flight. Making the trailing edge of the canard straight and normal to the centre-line of the vehicle will make installation of the Gurneys easier.

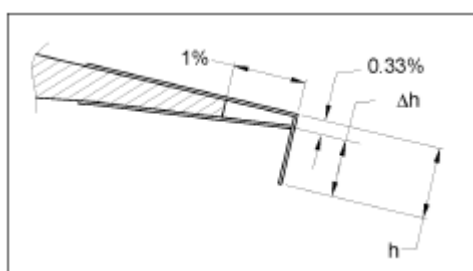


Figure 15 showing a typical trailing edge Gurney flap arrangement

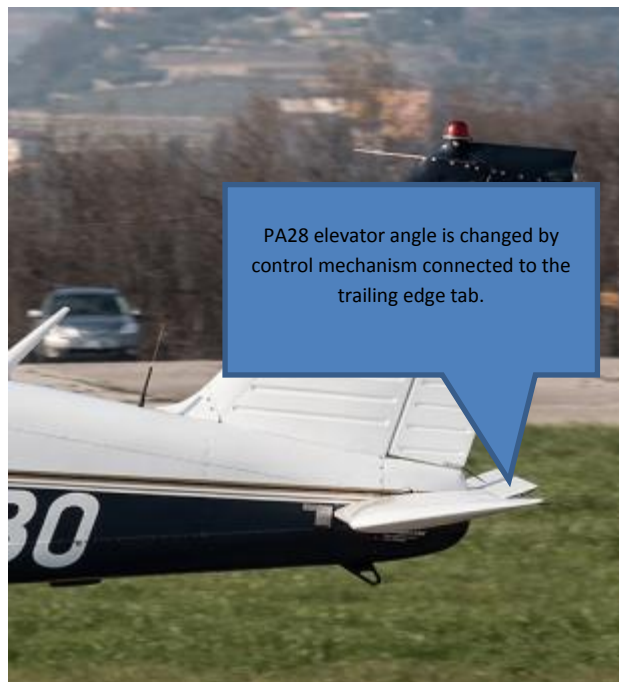


Figure 16 showing a light aircraft using a trailing edge tab to control the elevator

Addition requirements: Leading Edge Root Extension

At high angles of attack, a leading edge root extension (LERX) can be used to reinvigorate the suction surface and maintain the velocity (Figure 18). It may also help due to the uncertainty of the flow near the root of the canard due to lateral flow around the body induced by the wheel blockage. The feature exists by default due to the thickness requirements of the trunnion pivot and the need to maximise the distance between this point and the centre of pressure.

Note that for fighter aircraft the LERX commonly has a gothic plan-form (as shown in Figure 18), and sometimes coupled with fences; it is designed to position the vortex to encourage the airflow to maintain attached over the empennage and thus maintaining control effectiveness as extreme angles of attack. In the case of the AI5R canard, the goal is to energise the leading edge vortex of the panel. Thus the shape will take the form of a delta creating a double delta planform overall.

There is another reason for the LERX, and this was to do with the formation of shockwaves. If it is assumed that the body of the vehicle approximate to an ellipsoid, then the velocity may be described as follows

$$\frac{V_{surf}}{U_{\infty}} = \frac{u_{max}}{U_{\infty}} \sqrt{\frac{1-x^2}{1-x^2y^2}} \quad \text{with } y = \sqrt{1-r^2}$$

Where x is the distance from the mid-point in units so that the length is 2.0. Where r is the radius (or in these units the ratio of the diameter to the length.

The maximum velocity is;

$$\frac{u_{max}}{U_{\infty}} = \frac{2}{2-B} \quad \text{with } B = \frac{2(1-y^2)}{y^3} (\tanh^{-1} y - y)$$

The cross-sectional area of the vehicle at 3.75 m is 0.779 m². The shape is akin to a medieval kite shield (Figure 17), but for calculation purposes, it is assumed round with an equivalent diameter of 0.996 m. Using 15.45 m as the overall vehicle length results in y=0.9979. Thus B = 0.0205 and u_{max} is 1.01 U_∞, suggesting that when the vehicle reaches Mach 1.0, there is a chance that a weak shockwave will form in this region.

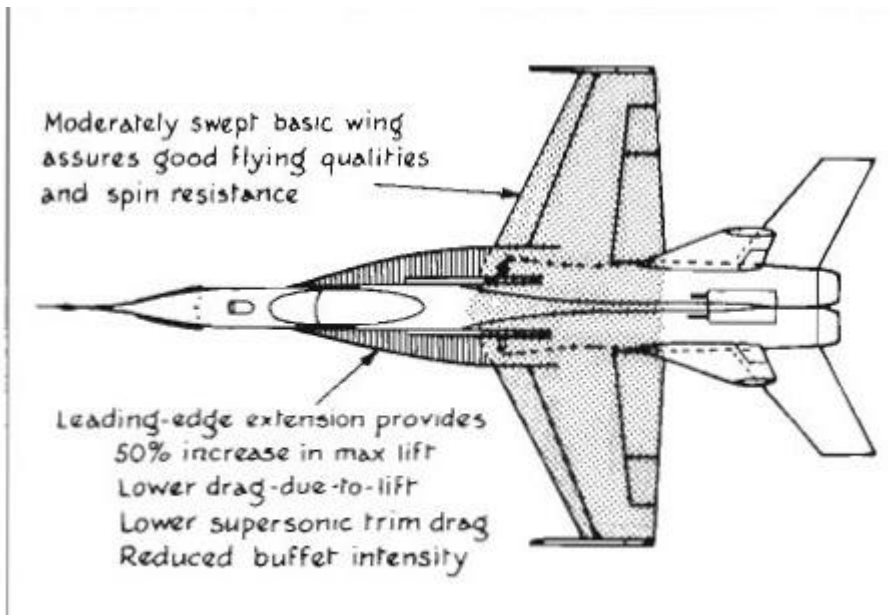


Figure 18 showing example fo leading edge root extension



Figure 19 showing a transonic transient shockwave formation at M 1.08 at maximum area point

Centre of pressure location

Selecting a delta planform meets the criteria that the centre of pressure should not move forward throughout the velocity range (Figure 200).

The calculation of the centre of pressures are shown in the spreadsheet extracts (Figure 21 and Figure 22). As expected, for a delta wing the centre of pressure will move backwards as velocity increases. The terminology and ESDU graphs used are shown in Figure 24. The centre of pressure and lift curve slopes were determined (see Figure 25, Figure 26, Figure 27 and Figure 28).

The span-wise centre of pressures was derived by extending the plan-form in Figure 31. Applying a parallel axis theorem to determine the corrected distance for a truncated tip Delta see Figure 29, Figure 30 and Figure 31. This approach yielded a value of 161 mm for M 0.9 and 153 mm for M 1.3. The distances being measured from the root. A pictorial representation of the centre of pressure movement with velocity is shown in Figure 32.

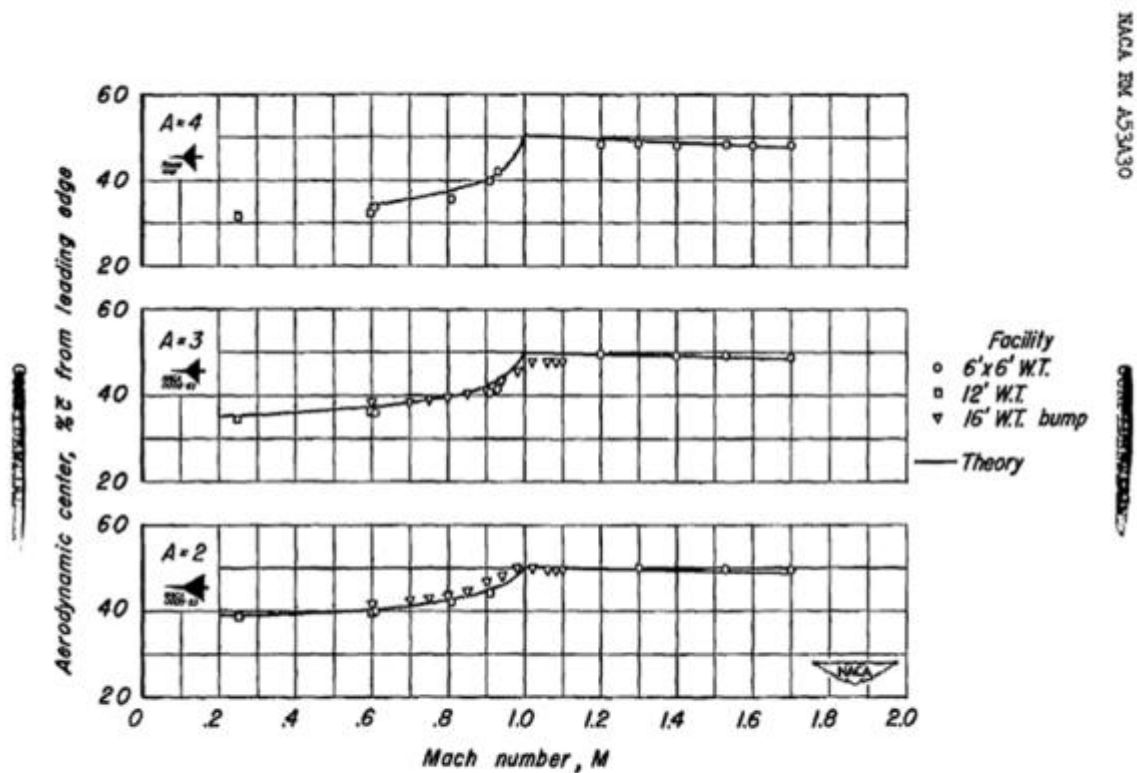


Figure 9.—The location of the aerodynamic center of plane triangular wings 3 percent thick.

Figure 20 showing rearward progression of centre of pressure for delta wing planform

Outer element subsonic	M0.7				
root chord	0.3470	m			
tip chord	0.1000	m			
taper ratio λ	0.2882				
mean aerodynamic chord (MAC) \bar{c}	0.246	m			
total area	0.140	m ²			
geometric mean chord	0.224	m			
panel span (b)	0.3000	m			
total span	0.6000	m			
1/2 chord sweep angle $\Lambda_{1/2}$	0.4285	Radians	24.55	degrees	
leading edge sweep angle Λ	0.7401	Radians	42.41	degrees	
a_0	6.2832				
Aspect Ratio A	2.5714				
e_w	0.8500	<i>an assumption</i>			
k	0.9700				
βA	1.84	M0.7			
$A \tan \Lambda_{1/2}$	1.17				
interplotion of \bar{x} / \bar{c} at M0.7	0.265				
distance from trailing edge to \bar{x} at MAC (m)	0.181				
pivot point of trunnion from trailing edge (m)	0.261	55% of 474mm actual root cord			
distance between trunnion centre line and centre of pressure (m)	0.080				

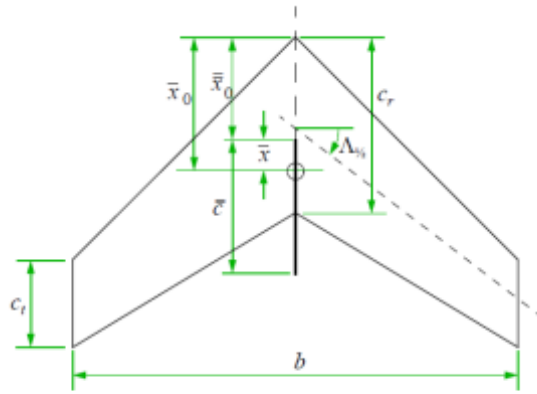
Figure 21 Showing a summary of centre of pressure calculations for M 0.9

Outer element subsonic M0.9					
root chord	0.3470	m			
tip chord	0.1000	m			
taper ratio λ	0.2882				
mean aerodynamic chord (MAC) cbarbar	0.246	m			
total area	0.140	m ²			
geometric mean chord	0.224	m			
panel span (b)	0.3000	m			
total span	0.6000	m			
1/2 chord sweep angle $\Lambda_{1/2}$	0.4285	Radians	24.55	degrees	
leading edge sweep angle Λ	0.7401	Radians	42.41	degrees	
a_0	6.2832				
Aspect Ratio A	2.5714				
e_w	0.8500	<i>an assumption</i>			
k	0.9700				
βA	1.12	M0.9			
$A \tan \Lambda_{1/2}$	1.17				
interplotion of xbar/cbarbar at M0.9	0.265				
distance from trailing edge to Xbar at MAC (m)	0.181				
pivot point of trunnion from trailing edge (m)	0.261	55% of 474mm actual root cord			
distance between trunnion centre line and centre of pressure (m)	0.080				

Figure 22 Showing summary of centre of pressure calculations for M 0.9

Outer Element supersonic	M1.3					
root chord	0.3470	m				
tip chord	0.1000	m				
taper ratio λ	0.2882					
mean aerodynamic chord (MAC) \bar{c}	0.246	m				
total area	0.140	m ²				
geometric mean chord	0.224	m				
panel span (b)	0.3000	m				
total span	0.6000	m				
1/2 chord sweep angle $\Lambda_{1/2}$	0.4285	Radians	24.55	degrees		
leading edge sweep angle Λ	0.7401	Radians	42.41	degrees		
a_0	6.2832					
Aspect Ratio A	2.5714					
e_w	0.8500	<i>an assumption</i>				
k	0.9700					
βA	2.14	M1.3				
$A \tan \Lambda_{1/2}$	1.17					
$\beta A - A \tan \Lambda_{1/3}$	0.96					
interplotion of \bar{x} / \bar{c} at M1.3	0.43					
distance from trailing edge to \bar{x} at MAC (m)	0.140					
pivot point of trunnion from trailing edge (m)	0.261	55% of 474mm actual root cord				
distance between trunnion centre line and centre of pressure (m)	0.120					

Figure 23 showing summary of centre of pressure calculations for M 1.3



Sketch 1.1 Wing notation

		<i>SI</i>
A	aspect ratio, b^2/S	
b	wing span, see Sketch 1.1	m
C_L	lift coefficient	
c_r	root chord, see Sketch 1.1	m
c_t	tip chord, see Sketch 1.1	m
\bar{c}	aerodynamic mean chord, see Sketch 1.1	m
M	free-stream Mach number	
n	fraction of chord	
S	wing area	m^2
\bar{x}	distance of aerodynamic centre aft of leading edge of aerodynamic mean chord, see Sketch 1.1	m
\bar{x}_0	distance of aerodynamic centre aft of leading edge of root chord, see Sketch 1.1	m
$\bar{\bar{x}}_0$	distance of leading edge of aerodynamic mean chord aft of wing apex, see Sketch 1.1	m
α	wing incidence	rad
β	compressibility parameter, $(1 - M^2)^{1/2}$	
Λ_n	sweepback of n^{th} -chord line	deg
$\Lambda_{1/2}$	sweepback of mid-chord line, see Sketch 1.1	deg
$\Lambda_{1/2M}$	$\tan^{-1} [(\tan \Lambda_{1/2})/\beta]$, see Appendix C	deg
λ	taper ratio, c_t/c_r	#

Figure 24 showing the canard nomenclature used

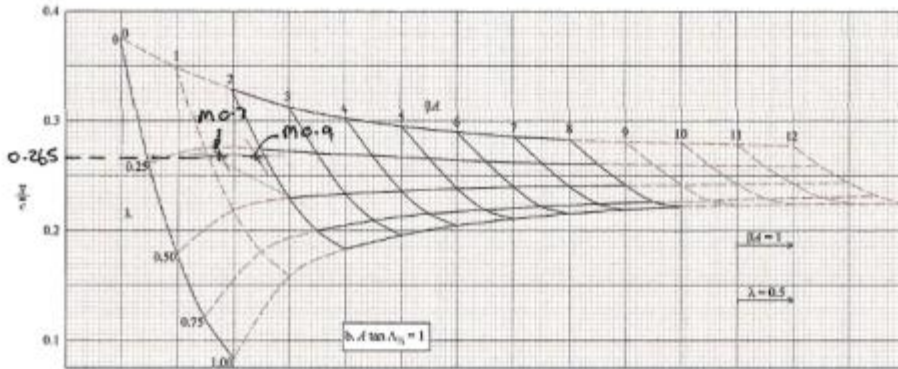


FIGURE 2b AERODYNAMIC CENTRE $A \tan A_{1/2} = 1$

ESDU 70011

Figure 25 showing ESDU charts for determination of subsonic centre of pressure

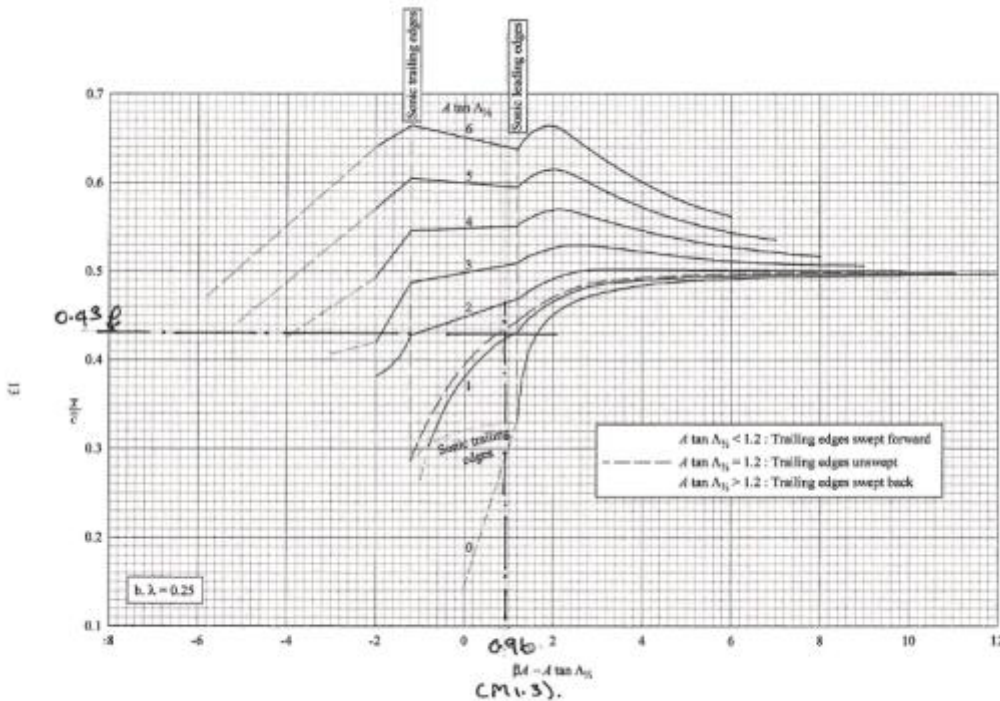


FIGURE 2b AERODYNAMIC CENTRE POSITION $\lambda = 0.25$ According $\lambda = 0.2882$

ESDU

70012

Figure 26 showing ESDU charts for determination supersonic of centre fo pressure

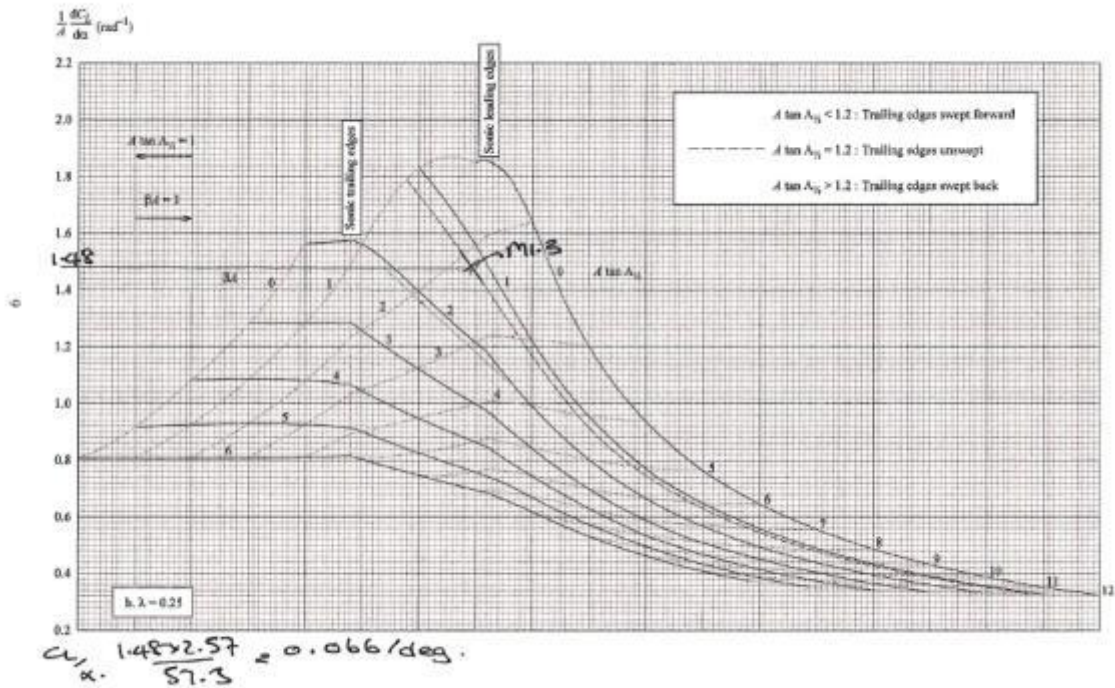


FIGURE 1b LIFT-CURVE SLOPE $\lambda = 0.25$

Figure 27 showing ESDU charts for determining lift coefficient rate for supersonic conditions

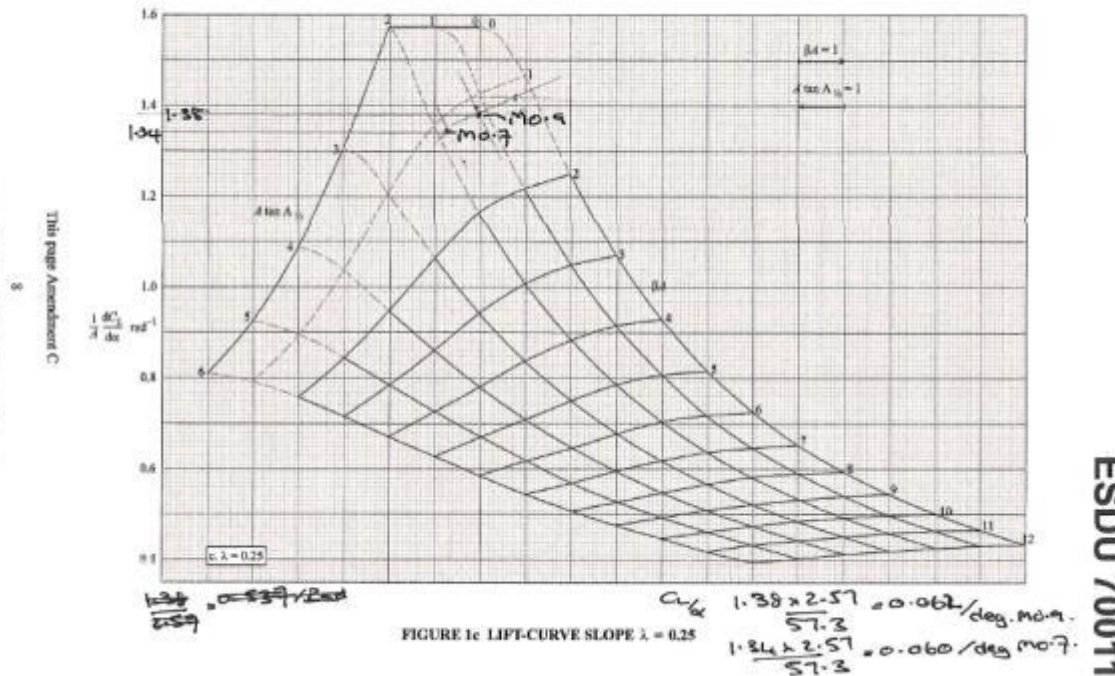


FIGURE 1c LIFT-CURVE SLOPE $\lambda = 0.25$

Figure 28 showing ESDU charts for determining lift coefficient rate for subsonic conditions

The span-wise centre of pressure				
			distance from root to virtual tip (m)	0.300
			distance from root to actual tip (m)	0.410
			virtual tip extension length (m)	0.110
			the total virtual area from CAD (m ²)	0.080
			actual tip chord(m)	0.100
			virtual tip area (m ²)	0.005
			panel area (m ²)	0.074
			subsonic spanwise centre of pressure	42.5%
			area moment of virtual area	0.014
			area moment of a virtual tip from the root	0.002
			resultant area moment	0.012
			the centre of pressure from the root (m)	0.161
			leading edge angle (Rad) ω_0	0.740
			Mach no.	1.3
			$\cos^{-1}(1/M\tan\omega_0)$	32.6
			supersonic spanwise centre of pressure	40.50%
			area moment of virtual area	0.013
			area moment of a virtual tip from the root	0.002
			resultant area moment	0.011
			the centre of pressure from the root (m)	0.153

Figure 29 showing span-wise centre of pressure calculations subsonic and supersonic (M 1.3)

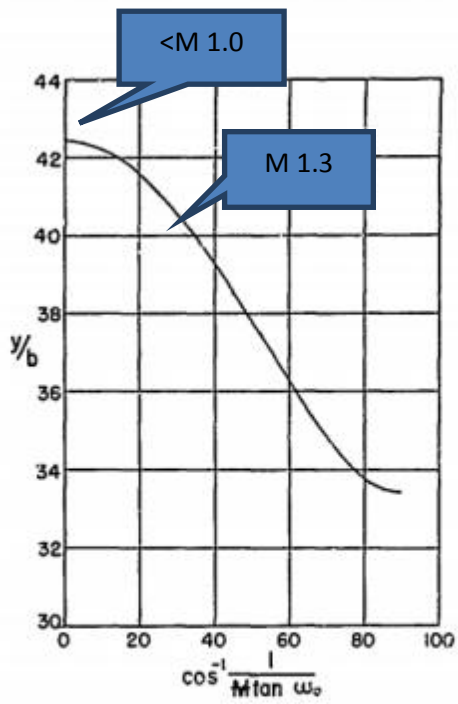


Fig. 12
SPANWISE CENTER OF PRESSURE
LOCATION - DELTA WINGS

Figure 30 showing span-wise centre of pressure graph used for supersonic values in Figure 29

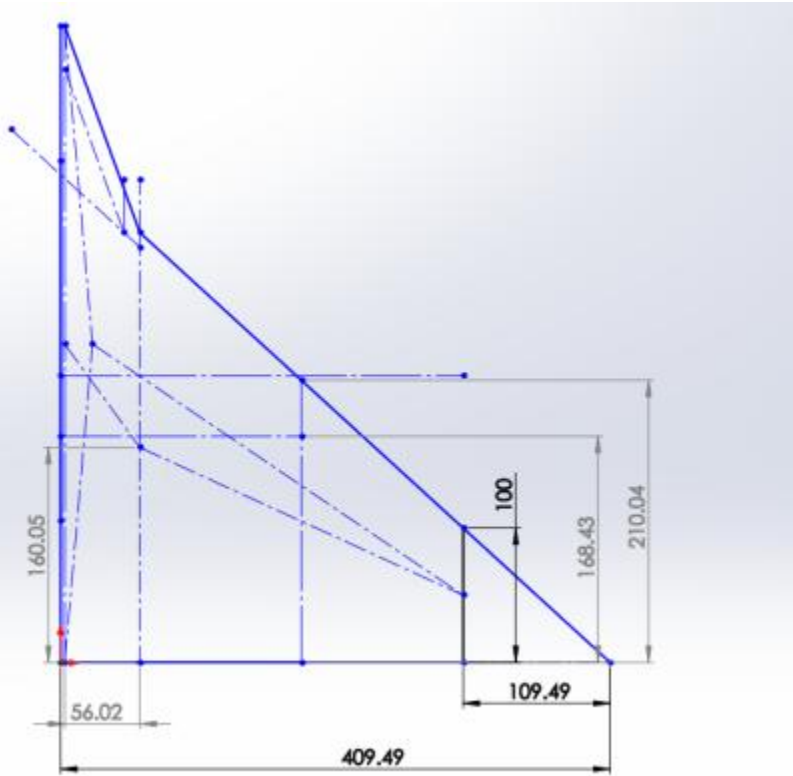


Figure 31 showing extrapolated plan-form used to calculate spanwise centre of pressure

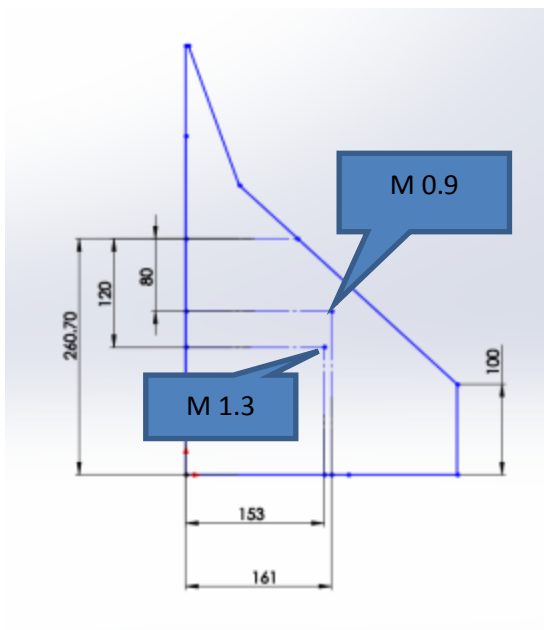


Figure 32 showing calculated centres of pressure

Trunnion space envelope

The trunnion acts as a pivot point and as such all the moments generated as a result of the lift or mass balances act through this point. Inevitably this will require a thickening of the section to add local strength and stiffness. Thickening of the section, especially a supersonic one, usually leads to a significant rise in the drag. Fortunately being at the root some of this additional thickness is shielded by the boundary layer. The following exercise was to determine the displacement boundary layer and the boundary layer thicknesses as an aid to setting a maximum size for the thickened region.

The boundary layer displacement thickness (Figure 33) creates an increase in the effective body size as seen by the airflow. The boundary layer is the layer or thickness of air immediately next to the surface under consideration that is affected by surface friction and viscous forces. It is considered the region up to the point where the local velocity reaches a value of at least 99% the free stream velocity. To simplify matters calculations using flat plate formula have been used (Figure 34). The boundary layer displacement thickness (δ^*) does not behave the same as the boundary layer as velocity increases, and compressibility effects are factored in. As Mach number and subsequent Reynolds number increases both the boundary layer (δ) and displacement thickness reduces. However, the proportions change (Figure 35). Without factoring in compressibility effects the ratio between δ/δ^* is approximately 8. This changes with compressibility and the displacement thickness graph (Figure 36) can be extrapolated to yield values for the vehicle operating in the transonic region

A distance of 3.750 m from the nose apex the boundary layer and boundary layer displacement thicknesses were calculated (Figure 37), Both get thinner as velocity increases. At M 1.3 the displacement thickness (δ^*) is about 5 mm and the full boundary layer (δ) extends to about 36 mm. In the case of the full boundary layer that means at a distance of 36 mm, the velocity in the boundary layer is about 99% of the free stream.

In summary, it means anything in δ^* will have minimal effect on drag (or flow) and for δ it can be assumed that the drag of anybody within that region is the ratio of its height to the boundary layer height x the drag expected in the free stream.

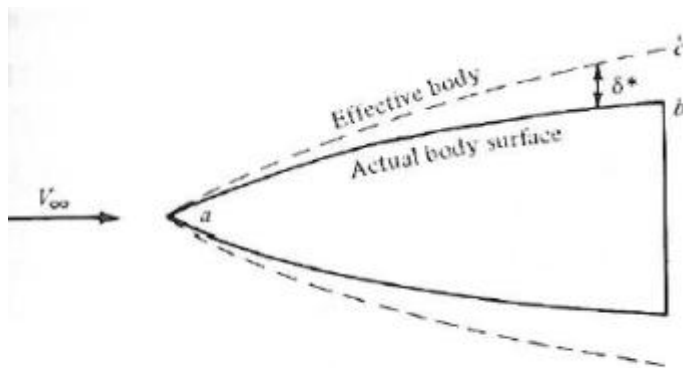


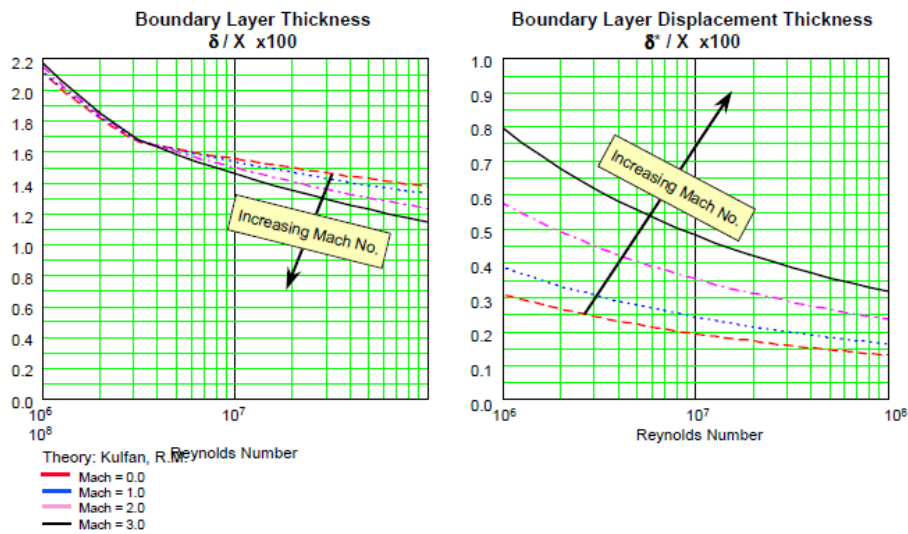
FIGURE 17.6
The "effective body," equal to the actual body shape plus the displacement thickness distribution.

Figure 33 showing the effect of the boundary layer displacement to body thickness

(b)	
Turbulent ^(†)	
$\frac{\delta}{x} \cong$	$\frac{0.38}{(Re_x)^{1/5}}$
$\frac{\delta^*}{x} \cong$	$\frac{0.048}{(Re_x)^{1/5}}$
$\frac{\theta}{x} \cong$	$\frac{0.037}{(Re_x)^{1/5}}$
$C_{f,x} \cong$	$\frac{0.059}{(Re_x)^{1/5}}$

Figure 34 showing boundary layer formulae used

Compressibility Effects on Boundary Layer Thickness



Boundary layer thickness and displacement thickness have been calculated for a range of Reynolds numbers and Mach numbers from 0 to 3 using the methods presented in this paper. The overall boundary layer thickness is seen to be relatively insensitive to Mach number. The boundary layer displacement thickness, however, grows rapidly as Mach number increases.

Figure 35 showing the change with Mach No. of boundary layer and boundary layer displacement thickness

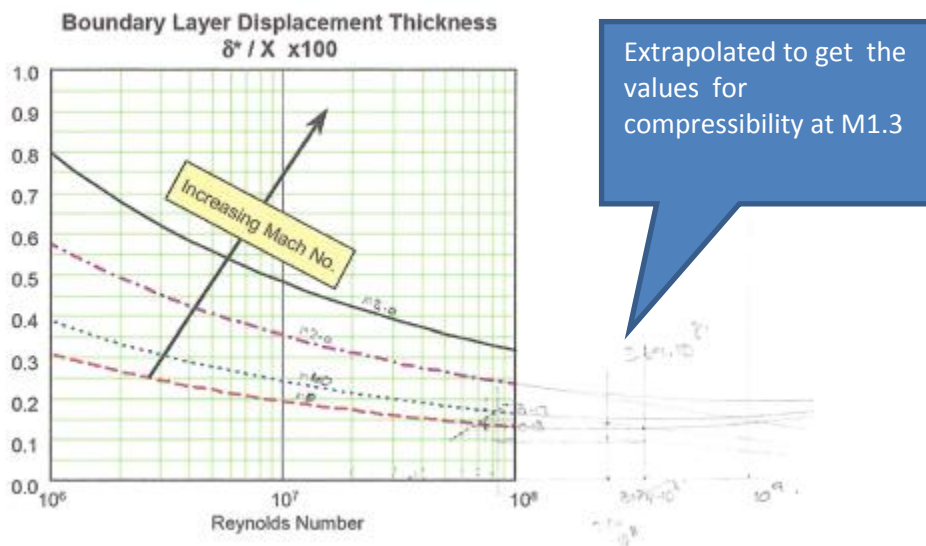


Figure 36 showing extrapolated values used to determine compressible displacement thickness

	Displacement Boundary layer thickness				δ^*	.048x/Re _x ^{1/5} incompressible								
	vRe _x	local Reynolds Number			68459	*Vx								
a=		343 m/s												
	Mach No	0.6	0.7	0.8	0.9	1	1.1	1.2	1.3					
	X (mm)	V	205.8	240.1	274.4	308.7	343	377.3	411.6	445.9				
Reynolds number per metre			1.41E+07	1.64E+07	1.88E+07	2.11E+07	2.35E+07	2.58E+07	2.82E+07	3.05E+07	all turbulent after 1 m			
approximate distance to leading ed	3.75													
local Reynolds number			5.28E+07	6.16E+07	7.04E+07	7.92E+07	8.81E+07	9.69E+07	1.06E+08	1.14E+08	1006*/x			
Boundary layer displacement thickness	δ^*		0.005	0.005	0.005	0.005	0.005	0.005	0.004	0.004	0.117	incompressible		
Boundary layer thickness	δ		0.041	0.039	0.038	0.037	0.037	0.036		0.006	0.17	compressible		

Figure 37 showing boundary layer thicknesses calculated vs. Mach No.

Sectional options

Two options were studied, a double wedge / double diamond and a bi-convex/elliptical. The double wedge advantage is that it is potentially easier to machine. Most of the initial analysis and sizing was done on the double wedge because of its modelling simplicity, especially when it came to discretising during FEA modelling.

The airfoil is limited to a maximum thickness percentage (t/c ratio) of 10% before drag becomes too great. As the canard is near to the front wheel to mitigate the unloading effect due to airbrakes and base drag increment, the canard needs to create a total downforce of about 4kN. However, the nominal set point of the vehicle is a negative 1-degree angle of attack which means a pitching change (especially as a result of a compliant surface and or suspension) can quickly result in an overall positive CL, leading to lift beyond that produced by the moment alone.

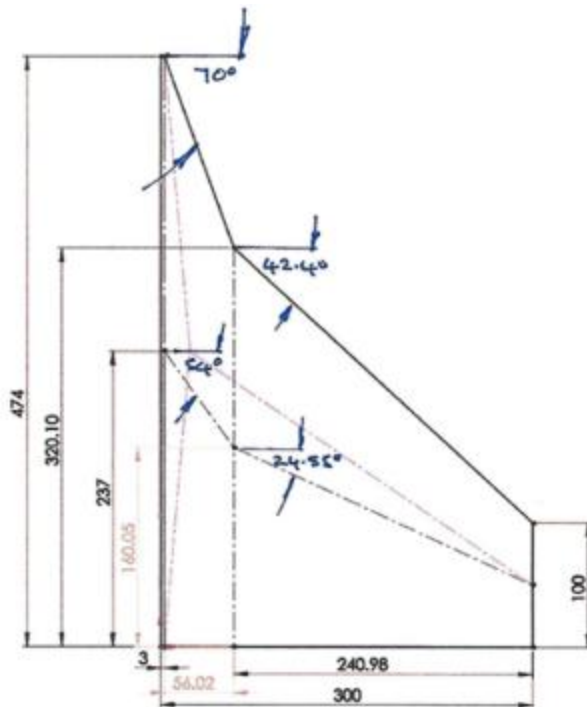


Figure 38 showing canard proposed "True" planform

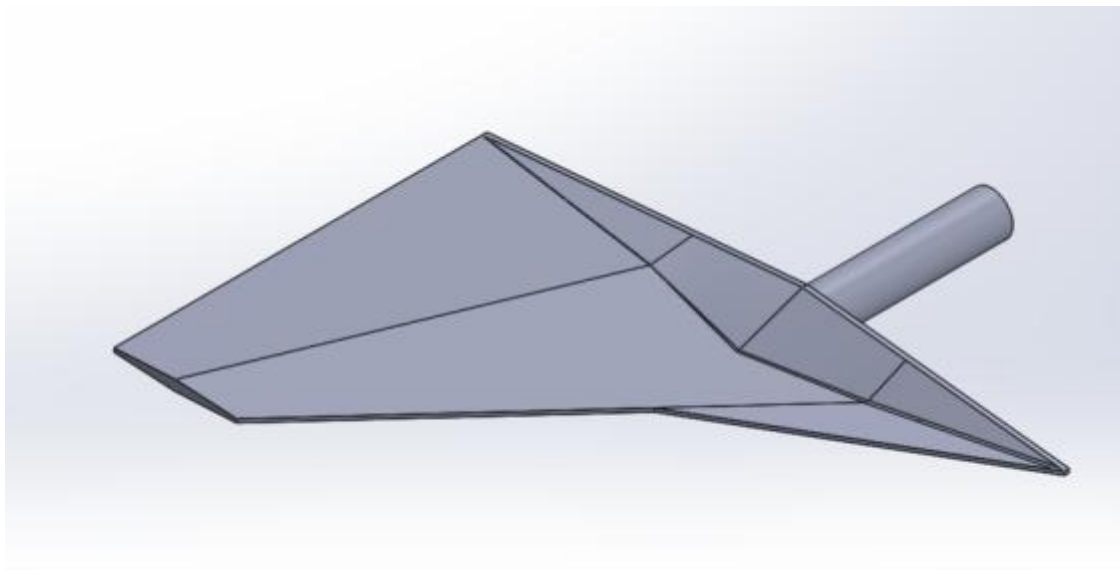


Figure 39 showing a pictorial view on initial double wedge / double diamond proposal

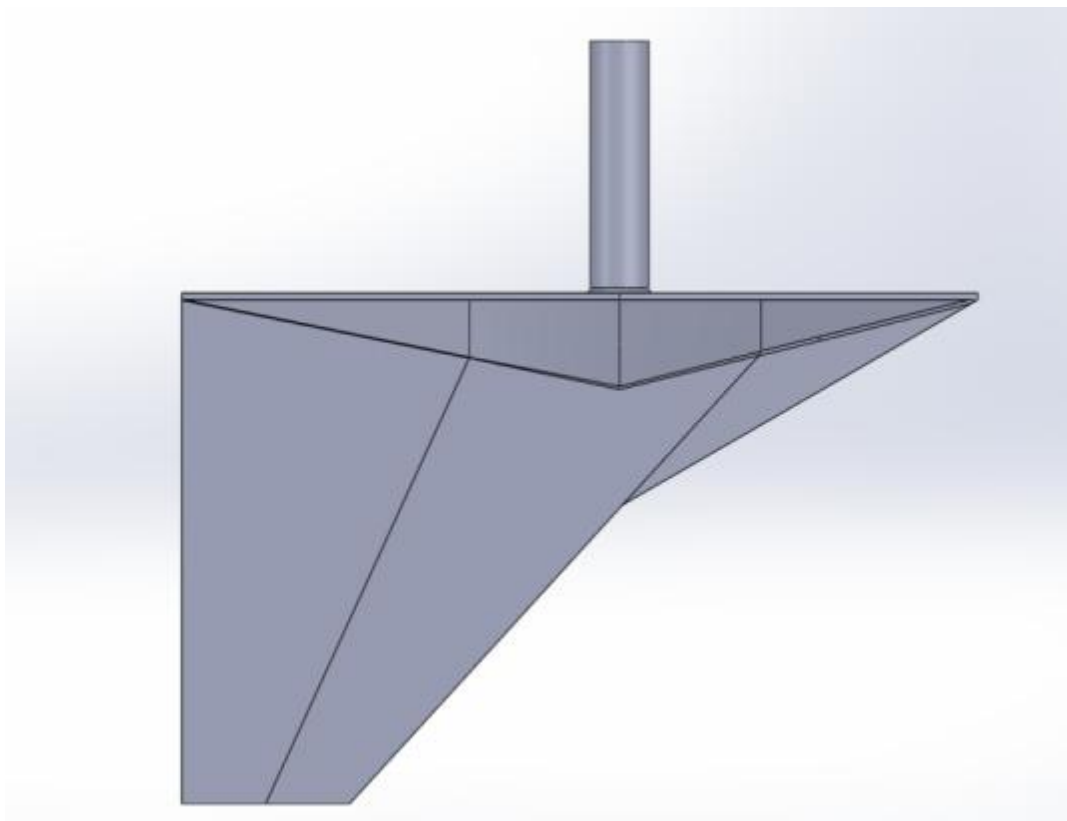


Figure 40 Plan view on initial canard proposal

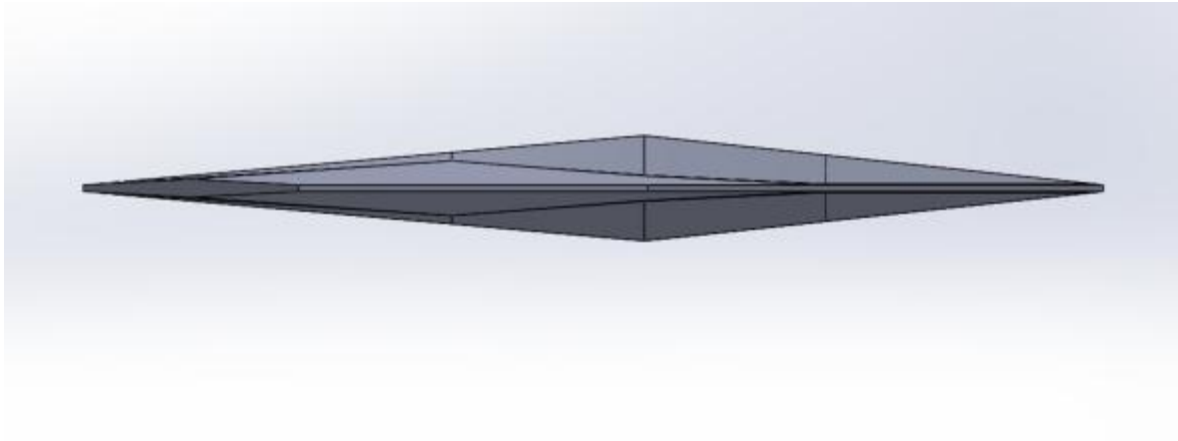


Figure 41 Side view on initial canard proposal

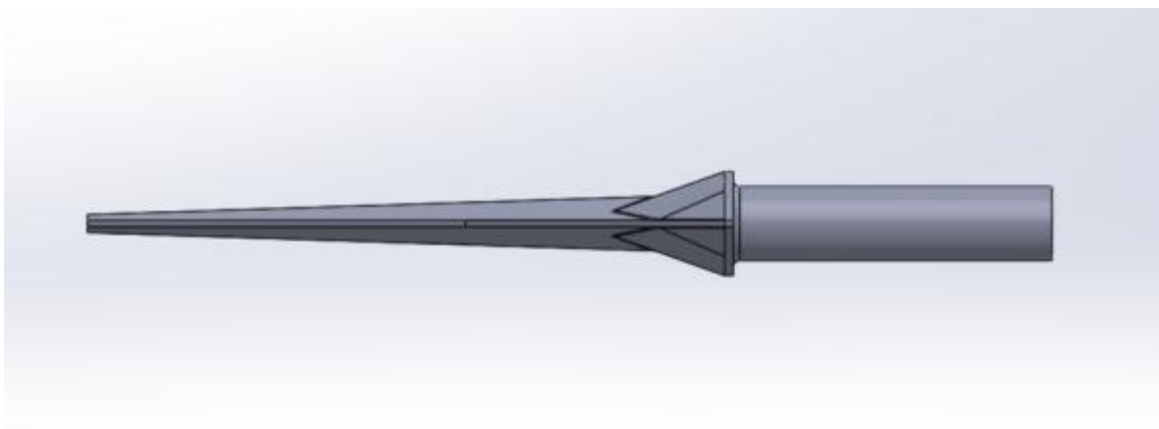


Figure 42 Front view on initial canard proposal

Laminar boundary layer trip features.

Because the dimensions of the canard are relatively small and the Reynolds number will also be low compared to say a fighter aircraft using a delta planform. At low angles of attack, it is possible for laminar flow to exist.

This is disadvantageous for two reasons;

Firstly, because the additional lift component of a delta is created through a leading edge vortex which requires separation to exist.

Secondly, because laminar flow can create a hysteresis effect in the lift curve slope, detaching early as the angle is increased but reattaching late as the angle is decreased.

As the wing is designed to float, it is possible that the operating angles of attack although transient will be both positive and negative. Any non-linear effect makes set up and tuning onerous and unpredictable. It is common when testing wind tunnel models where the model Reynolds number is expected to be many times smaller than the full sized application to utilise a trip wire or feature. In this manner, the transition becomes a controlled point rather than a floating one, and the hysteresis effect is either reduced or eliminated.

Reference NACA MEMO 10-5-58 A, a delta-winged model was used to determine the effect upon the lift to drag ratios by the application of leading edge flaps to simulate a conical profile. The Reynolds number for the baseline drag tests was 3.68 Million for the MAC (Figure 43). The trip wire used in this test was 0.25 mm diameter and was located on a ray from the nose apex to the dimension 1.33" as shown. At the point of the Mean Aerodynamic Chord (MAC), it represents 8.7% chord. (At the tip this represents approximately 46% of the chord). In this example, the trip had to fit around the flap features that were being evaluated as part of the test and arguably if there was no flap it could have run parallel. From the table shown in Figure 44, the trip appears to coincide with the limit of the laminar boundary layer at M 1.0. The laminar limit is taken as a Reynolds number of 500,000 or less. As the velocity increases then the distance over the wing or surface before the flow becomes turbulent reduces and this can be seen in Figure 44 with the 500k transition (Figure 45) point being 35.7 mm at M 1.0 reducing to 16.48 mm at M 1.3. The setup Figure 43 uses a trip wire that follows a ray path from the nose apex. In a delta wing, the pressure along a ray is the same thus separation with migrating along the ray. The advantage of a ray trip features rather than say a feature that is simply parallel to the leading

edge is that the constant in length will compensate for any variation in operating velocity. This approach should be incorporated into the canard wing (Figure 46). Machining of a 0.25 mm step would be difficult; one solution is to use 0.010" self-adhesive shim as shown in Figure 47. Another solution would be to mask up the leading edge and lacquer the rest of the wing, creating a small step in the coat.

A further study of the sections at the tip, MAC and root with chords 100 mm, 246 mm and 374 mm respectively. This used a modified N1600-4PR airfoil which is quasi-elliptical, 6 % thick. The trailing edge was modified in each case and thickened to 2 mm to reflect a minimum manufacturing condition. Reynolds numbers for a range of Mach numbers as a list in Figure 48, the upper and lower surface boundary transition position as a ratio of the chord are shown in Figure 49, suggesting that separation occurs almost at the leading edge with angles of attack greater than 1 degrees.

Due to its chord length, the tip suggests some hysteresis would be present at or around 0-degrees +/-1 degree showing at that angle the position of transition to be 80 mm back from the leading edge at M 0.9. As velocity decreases, this hysteresis will increase, and results are shown in Figure 50 at M 0.6.

Applying a boundary layer trip (BLT) at 46% and 20% (Figure 51) removes the hysteresis, in fact, any trip forward of the maximum thickness point is likely to achieve this. The effect on lift curve slope is minimal though there is the loss of the drag bucket at a low angle of attack. Some of the gains in drag may be negated by moving the BLT to the 20% position.

Similar results were seen for the MAC, though in this case the trips were placed at 8.7% and 3.8% (Figure 53 and Figure 54). The value of 3.8% being of the same proportion as the 20% to 46% used on the tip.

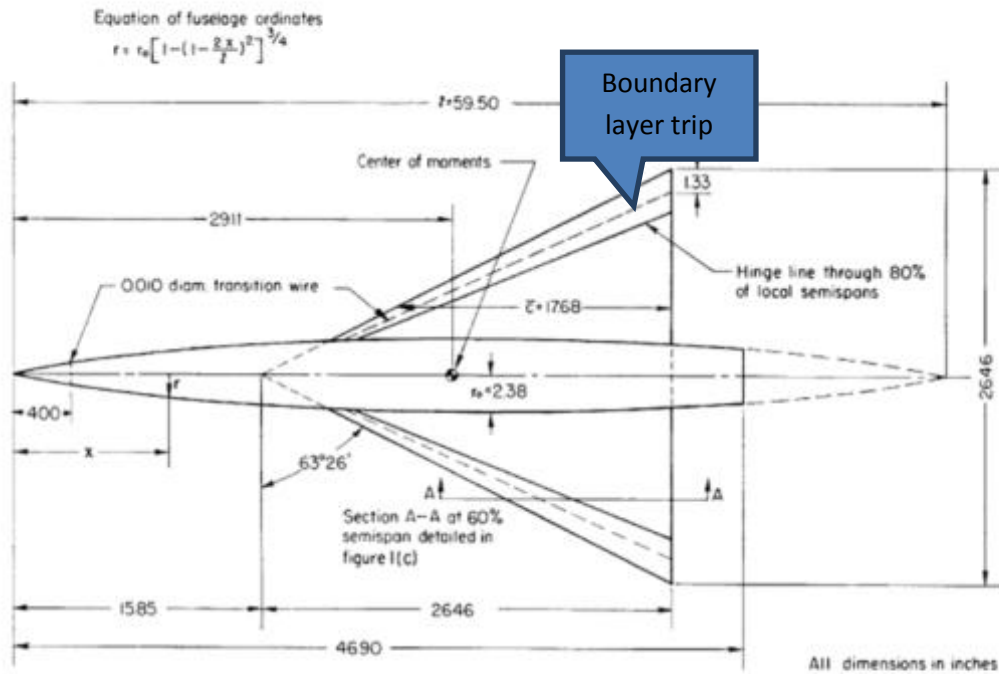
Conclusion: Set the trip up, so it coincides with the 20% chord position at the tip.

Boundary layer trip thickness.

The NACA model used a 0.25 mm trip. Figure 55 calculates the boundary thickness as approximately 1 mm so as a rule-of-thumb the trip height is 25%. This trip needs to be out of the displacement thickness at 20mm from the leading edge this is less than 0.1 mm. The size used will probably come down to what is easily available. Adhesive backed peelable shim is available in 0,125 mm thickness.

Conclusion . The BLT height should be between 0.1 and 0.15 ideally to minimise drag.

Parenthetically, the machining considerations lead to the need to create a finite thickness leading and trailing edge. Pragmatically this cannot be less than 2 mm in thickness. This abruptness may lead to a leading edge boundary layer trip condition.



(a) Dimensional sketch of model.

Figure 1.- Model details and dimensions.

Figure 43 showing the boundary layer trip

Boundary layer trip										
					MAC					
local chord base airfoil (m)		0.374	0.328	0.283	0.246	0.237	0.191	0.146	0.100	
local Reynolds Number x 10⁶		68459	Vx	a		341	m/s			distance back from leading edge for Renold'sNumber <500k i.e. laminar (mm)
local Reynolds Number Mach No.	0.6	5.24	4.60	3.96	3.45	3.32	2.68	2.04	1.40	35.70
local Reynolds Number Mach No.	0.7	6.11	5.37	4.62	4.02	3.87	3.13	2.38	1.63	30.60
local Reynolds Number Mach No.	0.8	6.98	6.13	5.28	4.60	4.43	3.57	2.72	1.87	26.77
local Reynolds Number Mach No.	0.9	7.86	6.90	5.94	5.17	4.98	4.02	3.06	2.10	23.80
local Reynolds Number Mach No.	1	8.73	7.66	6.60	5.75	5.53	4.47	3.40	2.33	21.42
local Reynolds Number Mach No.	1.1	9.60	8.43	7.26	6.32	6.09	4.91	3.74	2.57	19.47
local Reynolds Number Mach No.	1.2	10.48	9.20	7.92	6.90	6.64	5.36	4.08	2.80	17.85
local Reynolds Number Mach No.	1.3	11.35	9.96	8.58	7.47	7.19	5.81	4.42	3.04	16.48
trip feature distance back from leading edge at specific station (mm)										21.42

Figure 44 showing position of start of turbulent boundary layer

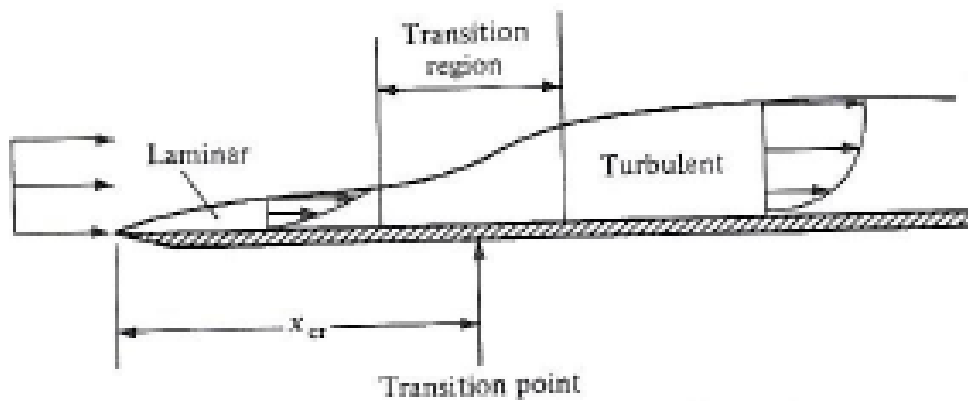


Figure 45 showing transition from laminar to turbulent boundary layer circa Re 500,000

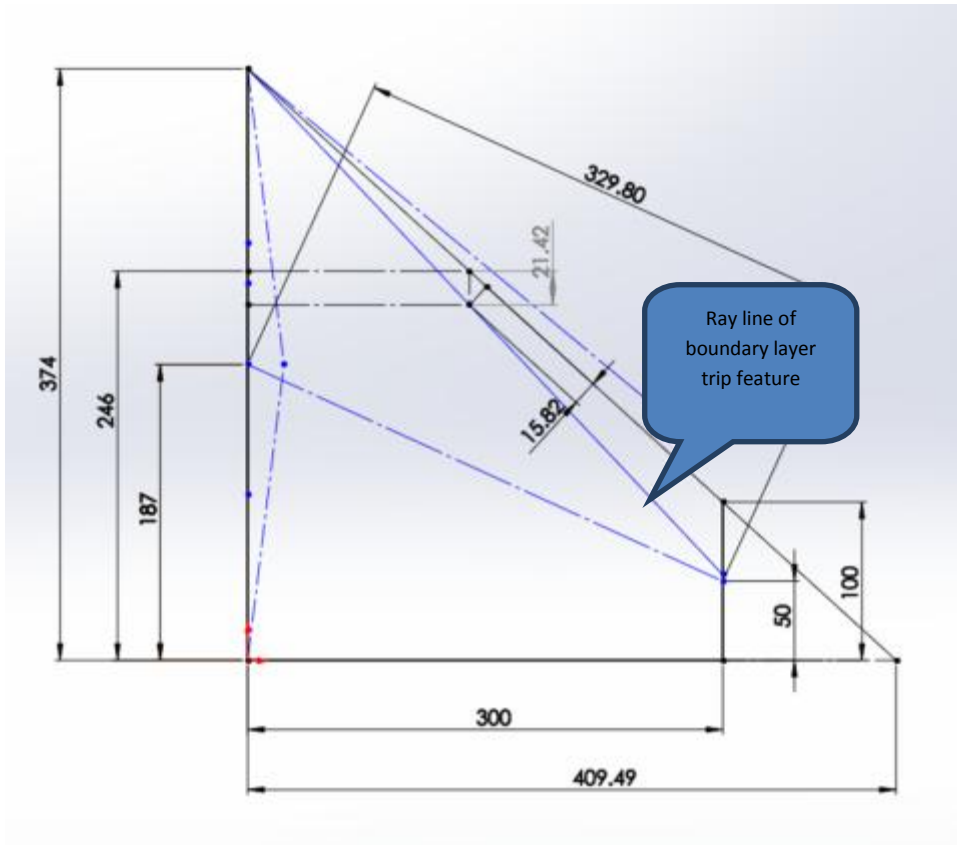


Figure 46 showing the idealised platform of canard used for general calculations

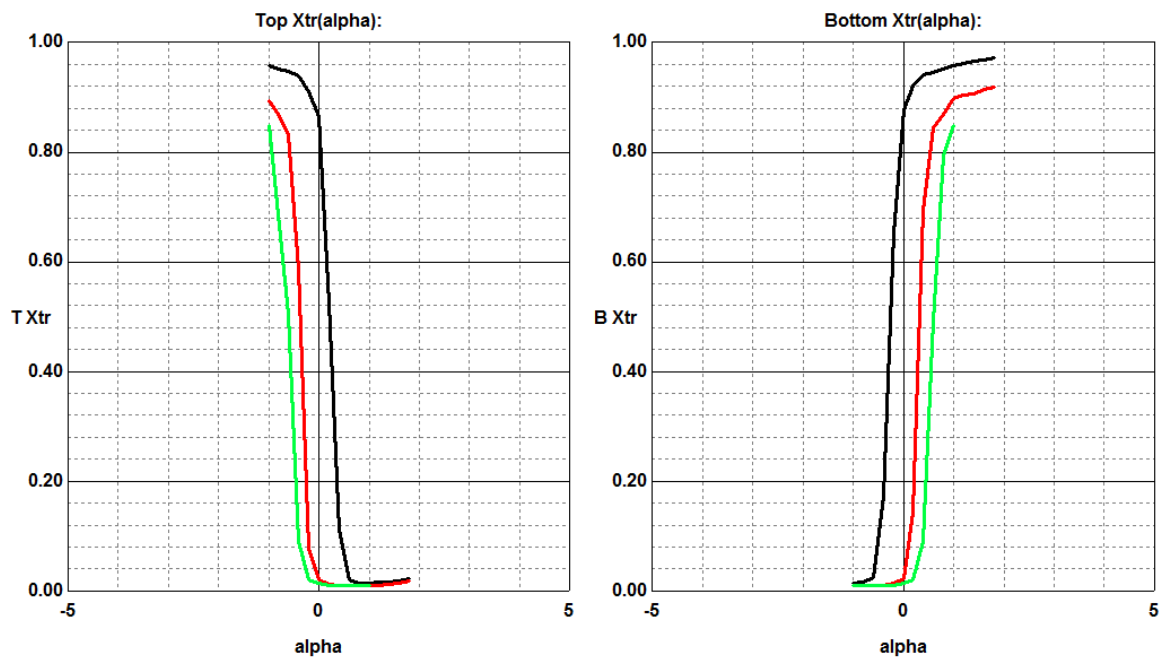


Figure 47 showing a boundary layer trip created using adhesive backed peelable shim steel applied to a missile fin

	$\sqrt{Re_x}$	local Reynolds Number		68459 * V_x							
	a=	343 m/s									
		Mach No	0.6	0.7	0.8	0.9	1	1.1	1.2	1.3	
	X (m)	V	205.8	240.1	274.4	308.7	343	377.3	411.6	445.9	
Reynolds number per metre			1.41E+07	1.64E+07	1.88E+07	2.11E+07	2.35E+07	2.58E+07	2.82E+07	3.05E+07	
canard root 347 mm	0.374		5.269	6.147	7.026	7.904	8.782	9.660	10.538	11.417	$\times 10^6$
canard MAC	0.246		3.466	4.044	4.621	5.199	5.776	6.354	6.932	7.509	$\times 10^6$
Canard tip 100 mm	0.1		1.409	1.644	1.879	2.113	2.348	2.583	2.818	3.053	$\times 10^6$

Figure 48 showing local chord Reynolds number as a function of vehicle velocity

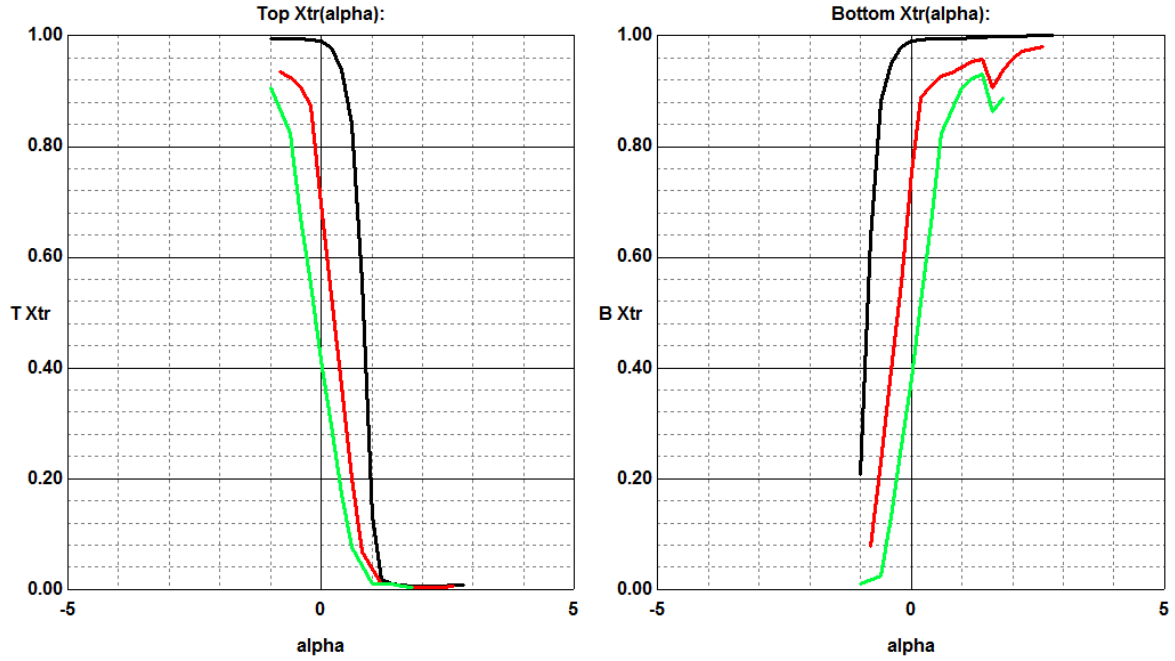
- 'N16004PR-006-TE 2mm at 100mm' at 2113000 Re - Mach=0.9000 - NCrit=9.00
- 'N16004PR-006-TE 2mm at 246' at 5199000 Re - Mach=0.9000 - NCrit=9.00
- 'N16004PR-006-TE 2mm at 374' at 7904000 Re - Mach=0.9000 - NCrit=9.00



Page 4 of 5 - Drawn by Profili 2.30b Pro on data processed by XFOil - Copyright (C) 1995-2014 - All rights reserved.

Figure 49 showing the upper and lower surface boundary layer turbulent transition points as a percentage of local chord and AofA

- 'N16004PR-006-TE 2mm at 100mm' at 1401000 Re - Mach=0.6000 - NCrit=9.00
- 'N16004PR-006-TE 2mm at 246' at 3466000 Re - Mach=0.6000 - NCrit=9.00
- 'N16004PR-006-TE 2mm at 374' at 5269000 Re - Mach=0.6000 - NCrit=9.00



Page 4 of 5 - Drawn by Profili 2.30b Pro on data processed by XFOil - Copyright (C) 1995-2014 - All rights reserved.

Figure 50 showing boundary layer transition position at M 0.6

- 'N16004PR-006-TE 2mm at 100mm' at 1401000 Re - Mach=0.6000 - NCrit=9.00
- 'N16004PR-006-TE 2mm at 100mm' at 1401000 Re - Mach=0.6000 - NCrit=9.00 - turb.: upper at 20.00%, lower at 20.00%
- 'N16004PR-006-TE 2mm at 100mm' at 1401000 Re - Mach=0.6000 - NCrit=9.00 - turb.: upper at 45.85%, lower at 45.85%

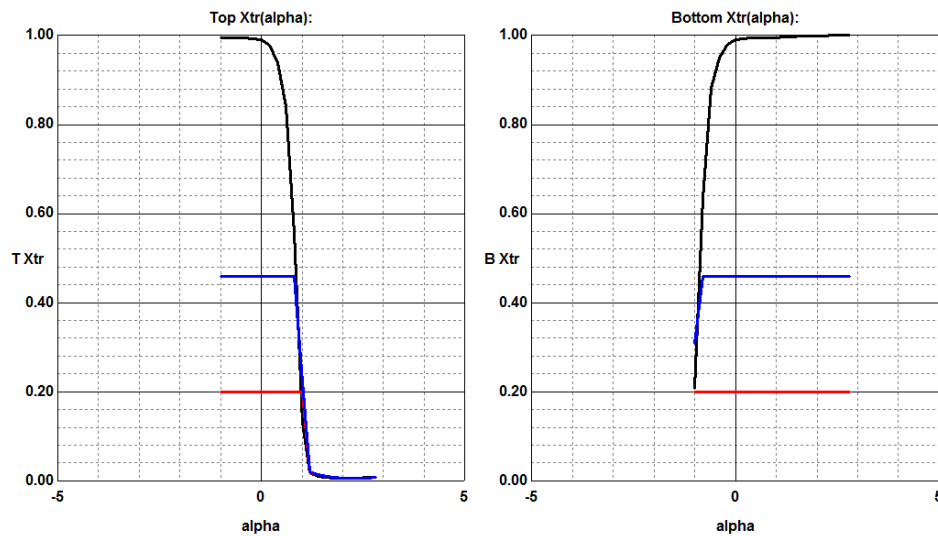


Figure 51 showing trips positioned at 20% & 46% of tip chord

- 'N16004PR-006-TE 2mm at 100mm' at 1401000 Re - Mach=0.6000 - NCrit=9.00
- 'N16004PR-006-TE 2mm at 100mm' at 1401000 Re - Mach=0.6000 - NCrit=9.00 - turb.: upper at 20.00%, lower at 20.00%
- 'N16004PR-006-TE 2mm at 100mm' at 1401000 Re - Mach=0.6000 - NCrit=9.00 - turb.: upper at 45.85%, lower at 45.85%

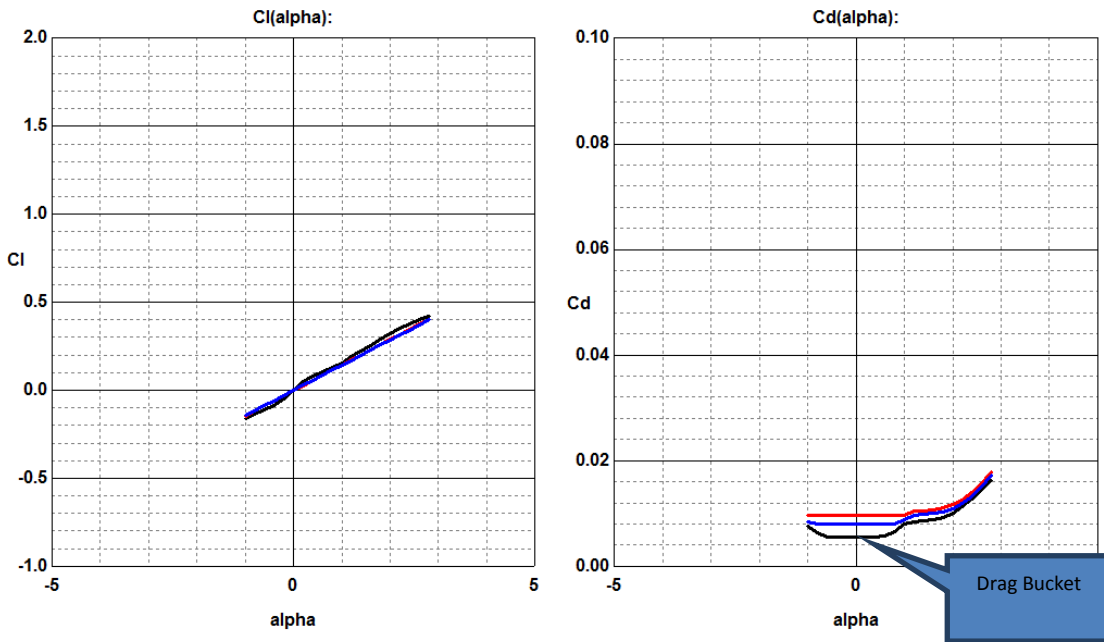


Figure 52 showing the effect of boundary layer trips (BLT) on Cl & Cd on tip

- 'N16004PR-006-TE 2mm at 246' at 3466000 Re - Mach=0.6000 - NCrit=9.00
- 'N16004PR-006-TE 2mm at 246' at 3466000 Re - Mach=0.6000 - NCrit=9.00 - turb.: upper at 8.70%, lower at 8.70%
- 'N16004PR-006-TE 2mm at 246' at 3466000 Re - Mach=0.6000 - NCrit=9.00 - turb.: upper at 3.78%, lower at 3.78%

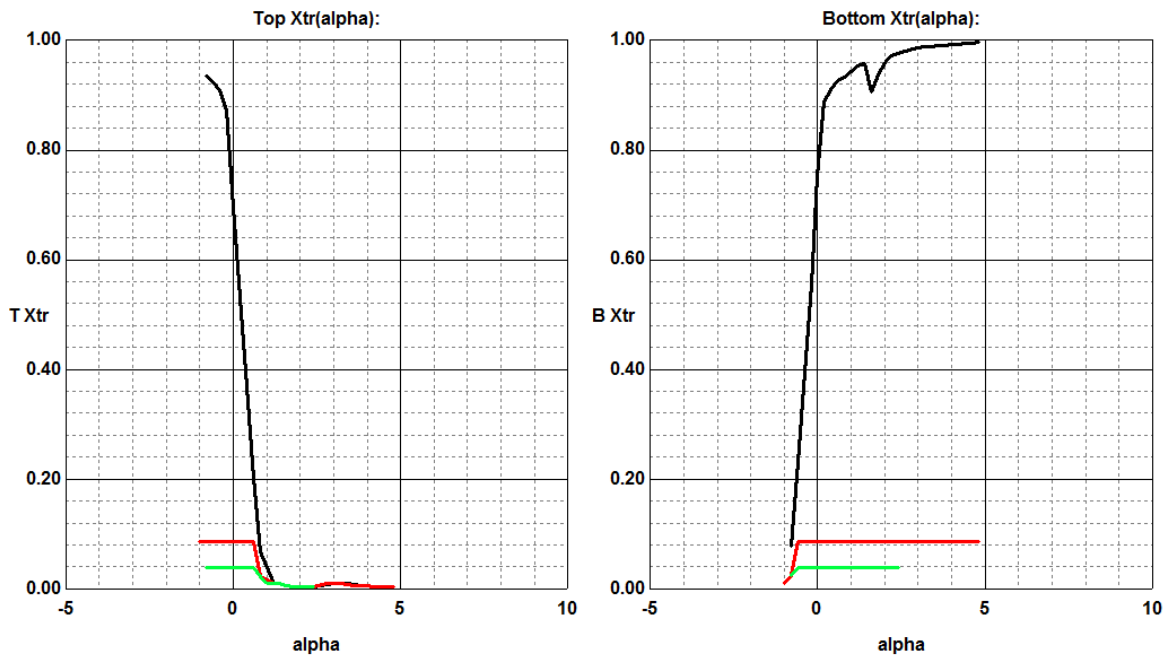


Figure 53 showing effect of BLT at the MAC position (chord =246 mm)

- 'N16004PR-006-TE 2mm at 246' at 3466000 Re - Mach=0.6000 - NCrit=9.00
- 'N16004PR-006-TE 2mm at 246' at 3466000 Re - Mach=0.6000 - NCrit=9.00 - turb.: upper at 8.70%, lower at 8.70%
- 'N16004PR-006-TE 2mm at 246' at 3466000 Re - Mach=0.6000 - NCrit=9.00 - turb.: upper at 3.78%, lower at 3.78%

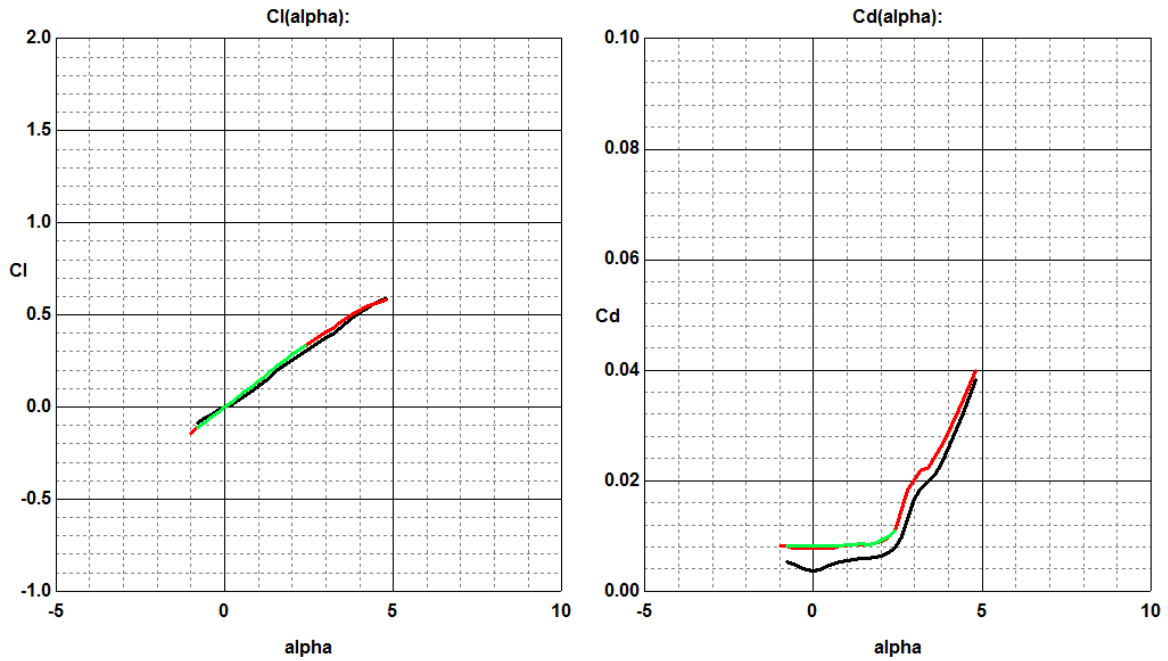


Figure 54 showing effect of BLT of Cl & Cd on MAC

	$\sqrt{Re_x}$	local Reynolds Number				68459	*Vx				
	a=	343 m/s									
		Mach No	0.6	0.7	0.8	0.9	1	1.1	1.2	1.3	
	X (m)	V	205.8	240.1	274.4	308.7	343	377.3	411.6	445.9	
Reynolds number per metre			1.41E+07	1.64E+07	1.88E+07	2.11E+07	2.35E+07	2.58E+07	2.82E+07	3.05E+07	
canard root 347 mm	0.374		5.269	6.147	7.026	7.904	8.782	9.660	10.538	11.417	
canard MAC	0.246		3.466	4.044	4.621	5.199	5.776	6.354	6.932	7.509	
Canard tip 100 mm	0.1		1.409	1.644	1.879	2.113	2.348	2.583	2.818	3.053	
Boundary layer thickness (mm) at 20% of 100mm chord	$\frac{\delta}{x} \cong \frac{0.38}{(Re_x)^{1/5}}$		0.62	0.60	0.58	0.57	0.56	0.55	0.54	0.53	
Boundary layer displacement thickness (mm) at 20% of 100mm chord	$\frac{\delta^*}{x} \cong \frac{0.048}{(Re_x)^{1/5}}$		0.08	0.08	0.07	0.07	0.07	0.07	0.07	0.07	
Boundary layer displacement thickness (mm) at 46% of 100mm chord	$\frac{\delta^*}{x} \cong \frac{0.048}{(Re_x)^{1/5}}$		0.15	0.15	0.14	0.14	0.14	0.13	0.13	0.13	
Boundary layer thickness (mm) at 39mm into MAC of NACA model	$\frac{\delta}{x} \cong \frac{0.38}{(Re_x)^{1/5}}$		1.05	1.02	1.00	0.97	0.95	0.93	0.92	0.90	

Figure 55 showing the δ and δ^* thicknesses for trips at 20 & 40% and the NACA model @8.7% of MAC

Flap modelling

The existence of a canard tends to move the vehicle centre of pressure forward and as previously discussed this reduces pitch stability. To negate this effect, a floating canard is used in conjunction with a Gurney flap. The whole principle is likened to a reflexed trailing edge used on flying wings where the camber-line is reflexed at the rear to neutralise the pitching moment, as there is no tailplane.

Though the expected Gurney height needed can be estimated it is customary to make a range of sizes to tune the vehicle during shakedown tests. One reason for this is that it is assumed the airflow runs parallel with the ground in reality and depending upon the effective angle of attack the air will spill around the side of the slender body and present itself at some angle to the canard. This can be seen in Figure 70 though this is a very extreme case, in the case of the AI5R, the front wheel is ahead and close to the canard and it will shed vortices. Ideally, the angle of incidence (static position) that the canard is set up to should be determined at the very least using preliminary tuft or oil film testing as even a negative angle of incidence may result in a positive angle of attack.

The other reason is that the theory is based on linear values of CL per degree. As with most engineering assumptions, this is a simplification as the slope will be non-linear to some degree.

It is relatively easy to change gurney heights by interchanging them. They only need to be bolted on.

There are two ways that a self-controlling floating wing can be created. The first is to adjust the camber and the second is to use a Gurney flap. Both act in a similar manner, they create a pitching moment in the rear portion of the wing that is counteracted by the lift created as the wing takes up an angle of attack as a result of this pitching moment. The moments eventually equate, and a steady state angle is taken up. It is then possible by adjusting the camber or Gurney flap to have the wing run at a target angle at a target velocity. The wing needs to take up a negative angle of attack of approximately 8 degrees to generate the downforce required to offset the predicted moment induced by the rise in base drag during braking. The 8 degrees emanates from base drag calculations (see Appendix A).

Parenthetically, the final design has steered a solution towards a combination of both. To avoid the need for complex curvature gurney flap machining the underside of the canard has had a flat plane added. This is similar to a camber change. On top of this flat plane, a simpler Gurney (strip) can be bolted.

There is a classical theoretical method to predict the effect of a change in the camber line of an airfoil. A flap is a change in a camber line though it does have a somewhat abrupt change in angle.

Though there are many experimental data theoretical models to predict the change in the sectional lift due to the incorporation of a Gurney flap appears non-existent. This is probably because the effort that previously when into classic aerodynamic theory is now assigned to computational techniques. As such one had to be created. The confidence level is considered reasonable as it has not been verified by experimental testing. But it was based upon the thin airfoil theory, and the model does suggest that the Gurney would only have to be around 2% to meet the moment requirements which is in the expected range for such devices.

So there is a trade-off, the theory for camber line prediction for a change to a wing's performance is well-established, and such camber line change can be machined into the wing, but it becomes permanent. The gurney flap is less predictable but easy to change and tune.

The theory for camber line is well understood. To determine it's accuracy a model was created for a rectangular wing with an aspect ratio of 6 using an airfoil section NACA 23012. This was selected because of the volume of test data available for this section. The calculated results could then be compared with the experimental and a confidence level established. A model was created with a 20% flap chord and the results calculated (Figure 56) for a 10 and 40 degrees deflection.

Calculations were then taken about a chord of 260.7mm, and this becomes the reference. At this spanwise chord, the leading edge of the section corresponds to the centreline position of the trunnion pivot and thus makes simplifies moment calculations.

The results appear favourable when the results were compared with the experimental results (Figure 58). These were based upon the improvement to the maximum lift coefficient. For comparison purposes, and it was assumed that the maximum lift position was 20 degrees (Figure 57). A consideration when making the comparison needs to be made to the pre-existing camber line of the NACA 23012 airfoil as this will bias the figures. This bias was removed by averaging the results for the positive and negative values of flap deflection. The non-linearity of the experimental curve reflects the progressive breakdown of the flow on the suction surface. This was why the split flap begins to outperform the plane flap. The split flap by its design, only deflects on the low (pressure surface) of the airfoil and thus the pressure gradient on the suction surface (because it doesn't change angle) is less effected and so there is a delay in detachment. Arguably this has similarities to the flow field a Gurney creates, as the flow does not separate on the suction surface. In fact, the vortex moves the stagnation point further round and encourages attachment allowing higher angles of attack to be attained (Figure 58). This has and added advantage if an elliptical section is adopted. This effect manifests itself in a change in lift curve slope when using a Gurney flap is shown in Figure 64. There is also a change in the

lift curve slope for a plain or split flap by the effect is not as dramatic for small deflection angles.

Typically a trailing edge displacement for a 20 chord plane flap of 1% airfoil chord is about 2.9 degrees.

An empirical formula for the effect that connects the Gurney flap height with the increase in maximum lift coefficient is shown in Figure 65,

This shows good correlation using digital techniques (Figure 66), and the results are calculated in the table shown in Figure 68 and also suggests a good correlation. However, experimental studies on an NACA 23012 suggests that the gain averaged over is about 12% (3-D) compared to an average of 5% of 18.5% (2-D) But when a correction is made for the aspect ratio the two values coincide. A Gurney flap model was created using the plan flap theory. In this case based on previous studies, a chord of 3.75% was used. A deflection angle of approximately 20 degrees is resulting in an equivalent gurney flap height of 1.35%. Such height should yield the desired steady state angle of attack position of -7.84 degrees.

When the wing is presented with the supersonic flow, the centre of pressure of the plan-form moves rearward as expected. As such the steady state angle of attack will reduce. The nature of supersonic flow around a body compounds this effect. A model using a flapped supersonic section is shown and suggests the angle of attack if left free to rotate, will reduce to about 1.75 degrees see Figure 69.

Whether either the camber or Gurney flap method is adopted, with a free floating arrangement this is a self-correcting solution that arguably addresses the FAI requirements for an LSR vehicle.

Exploitation of a hidden benefit of the Gurney.

Referencing Figure 59 one of the effects of a Gurney flap is that it maintains the Kutta condition at the trailing edge and where previously the angle of attack was too great, and separation was occurring it can force reattachment. One limitation of a supersonic section is the need for it to be thin. Whether the section is a double diamond or bi-convex a low thickness/chord ratio (t/c) results in a low second and polar moments of the area leading to reduce flexural stiffness resulting in potential bending, torsional and flutter issues. An elliptical profile leads to superior moment area characteristics. However, the downside is that the flow will separate before the trailing edge. This increases drag and lowers the effective working area of the wing where the lift is concerned. For the same t/c ratio, an ellipse is not likely to be as poor as a double diamond section for subsonic separation and arguably can be as good as a bi-convex. A more complex section could be selected such as an NACA 66 series, but this adds significantly to the complexity of manufacturing, and with the small chord at the tip and relatively low Reynolds Number value it incurs it is unlikely to make any difference. However, this desire for the airflow to prematurely detach at the trailing edge is likely to be negated with the Gurney, certainly in the case of the



bi-convex and elliptical section cases. Possibly not so in the double wedge profile because detachment will most likely be at the apex of the thickness which is approximately 50% of the chord.

The advantages of bi-convex and double diamond at supersonic velocities are primarily associated with the leading edge angle. If the angle is smaller than the maximum permissible deflection angle for a particular Mach number, then any shockwave will remain attached. Above this angle and it detaches, and drag goes up. For manufacturing reasons the nose cannot be a point and has a minimum bluntness of 2 mm whatever section is chosen, so any shockwave that forms will detach negating any advantage.

Version 8 convergence.

It was found that when modelling with a modified N-16 section nominally at 6% thickness that this airfoil could be closely approximated by the creation of an ellipse between the nose and the 50% chord point and then an arc from the 50% to the trailing edge. This applied to the 374 mm chord. The 100 mm chord could only be approximated closely using a biconvex (arc) method. The driver for the choice of modelling was the 2 mm thick truncated nose, this being driven by manufacturing consideration. The profiles used can be seen in Figure 62 and Figure 63

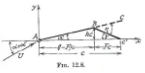
REF. Aerodynamics for Students Houghton & Brock. Subsonic Model							
							
		Gurney model for 1% chord			Camber model to give target base drag angle	Gurney model to give target base drag angle	Gurney model to give target base drag angle
Chord	1	0.2607	1	0.2607	0.2607	0.2607	0.2607
flap proportion F	0.2	0.2	0.2	0.5	0.2	0.0375	0.07671653
unflapped proportion UF	0.8	0.8	0.8	0.5	0.8	0.9625	0.92328347
flap deflection angle (deg)	10	2.862685	40	1.145847	5.648376	19.850957	14.7133071
flap deflection angle η (Radians)	0.174551	0.049968	0.698202	0.020001	0.098593	0.34649951	0.25682156
flap deflection distance (m)	0.035269	0.002608	0.167844	0.002607	0.005157	0.00352988	0.00525242
equivalent Gurney percentage	3.53%	1.00%	16.78%	1.00%	1.98%	1.35%	2.01%
α'	0.035254	0.010002	0.166294	0.010001	0.01978	0.01353917	0.02014465
$\cos\phi$	-0.6	-0.6	-0.6	0	-0.6	-0.925	-0.8465669
ϕ	2.214297	2.214297	2.214297	1.570796	2.214297	2.75183192	2.58029844
Initial angle of attack α (Rad)	0	0	0	0	0	0	1
camber peak height (h) when AofA is adjusted	0.028215	0.008002	0.134275	0.005001	0.015826	0.01303225	0.01860174
$A_2 = (\eta \sin 2\phi) / \pi$	-0.05334	-0.01527	-0.21335	7.8E-19	-0.03013	-0.0775301	-0.0736741
$A_1 = 2 \sin \phi \cdot \eta / \pi$	0.088898	0.025449	0.355591	0.012733	0.050213	0.08381635	0.08702692
$A_0 = \alpha + \alpha' + h/F - (\phi/\pi)(h/UF + h/F)$	0.052037	0.014761	0.24616	0.010001	0.029193	0.04479479	0.04691859
$C_{M.L.E.}$	0.033828	-0.07515	-1.1128	-0.03571	-0.14839	-0.2629139	-0.2682646
$C_{M.L.E.} \times \text{chord}$		-0.01959	-1.1128	-0.00931	-0.03869	-0.0685417	-0.0699366
$CL_{\text{increment}} = 2\pi A_0 + \pi A_1$	0.606237	0.172695	2.663793	0.102842	0.341176	0.54477082	0.56820134
h/F	0.141076	0.040008	0.671376	0.010002	0.079131	0.34752663	0.24247366
ϕ/π	0.704833	0.704833	0.704833	0.5	0.704833	0.87593531	0.8213345
wing aspect ratio	6	2.57	6	2.57	2.57	2.57	2.57
efficiency factor	0.99	0.99	0.99	0.99	0.99	0.99	0.99
$a_e \text{ (Rad}^{-1}\text{)}$	6.283185	6.283185	6.283185	6.283185	6.283185	6.28318531	6.28318531
$a_e \text{ (deg}^{-1}\text{)}$	0.109673	0.109673	0.109673	0.109673	0.109673	0.10967333	0.10967333
$a_{\text{wing}} \text{ (Rad}^{-1}\text{)}$	4.665265	3.498098	4.665265	3.498098	3.498098	3.49809811	3.49809811
$a_{\text{wing}} \text{ (deg}^{-1}\text{)}$	0.081432	0.061059	0.081432	0.061059	0.061059	0.06105949	0.06105949
$a_{\text{wing}} \text{ (Rad}^{-1}\text{) from test}$	4.296	4.296	4.296	4.296	4.296	4.296	4.296
$a_{\text{wing}} \text{ (Rad}^{-1}\text{) } 2\pi\alpha \text{ theoretical 2-D}$	2.193467	2.193467	2.193467	2.193467	2.193467	2.19346668	2.19346668
stall angle of wing (deg)	20.00	20.00	20.00	20.00	20.00	20.00	20.00
stall angle of wing (Rad)	0.349101	0.349101	0.349101	0.349101	0.349101	0.34910106	0.34910106
CL at stall onset theoretical	1.50	1.50	1.50	1.50	1.50	1.50	1.50
CL at stall onset experimental RE 8.4M	1.5	1.5	1.5	1.5	1.5	1.5	1.5
$CL_{2-D} + CL_{\text{increment}}$	2.106237	1.672695	4.163793	1.602842	1.841176	2.04477082	2.06820134
percentage increase due to $CL_{\text{increment}}$ used only to estimate the accuracy of this approach using test data	29%	10%	64%	6%	19%	26.6%	27%
correction value for 3-D Gurney flap only						0.56445892	0.56445892
$C_{L3-D} + C_{L3-D \text{ increment}}$						1.15418913	1.1674147
distance from leading edge to c of p (m)		0.079708		0.079708	0.079708	0.07970803	0.07970803
lift curve slope of delta (Rad ⁻¹)		3.5466	from ESDU	3.5466	3.5466	3.5466	3.5466
Steady state angle (Rad)		-0.07		-0.033	-0.137	-0.137	-0.140
Steady state angle (Deg)		-3.97		-1.887	-7.840	-7.841	-8.000
Target angle (deg)					-8.00	-8.00	-8.00

Figure 56 Showing a summary of flap performance base on subsonic camber-line theory

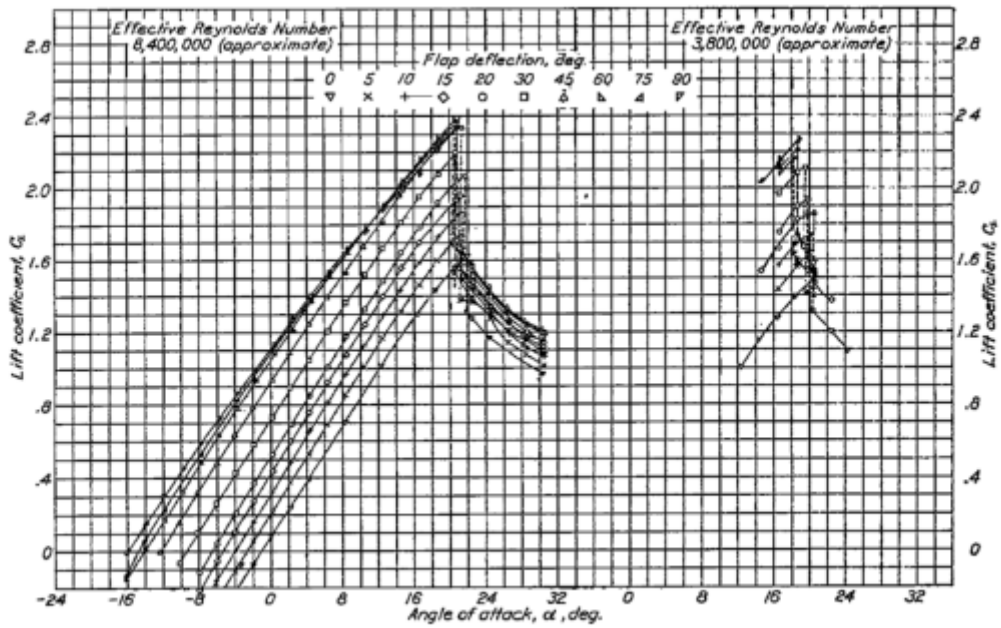


FIGURE 5.—Lift for the N. A. C. A. 23012 rectangular wing of aspect ratio 8 with 0.20c full-span split flap.

Figure 57 Showing NACA23012 maximum lift points for various flap deployment angles

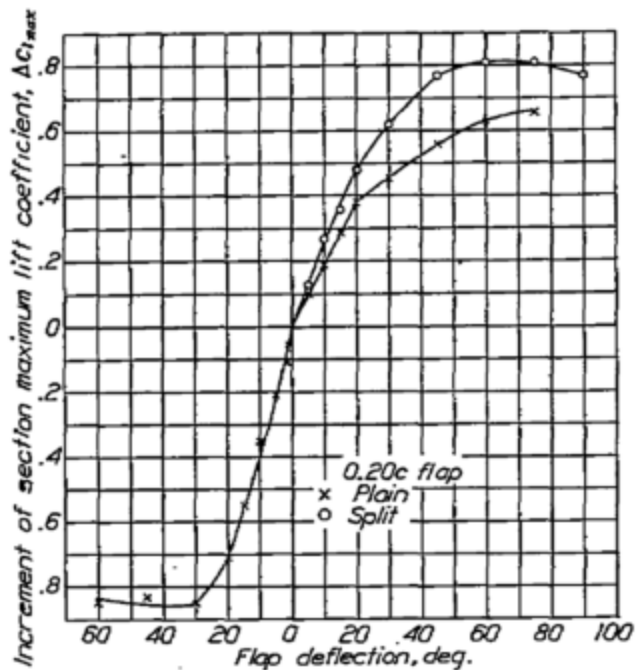


FIGURE 10.—Variation with flap deflection of the increment of section maximum lift coefficient caused by 0.20c plain and split flaps on the N. A. C. A. 23012 airfoil.

Figure 58 Showing NACA 23012 incremental lift coefficient for various flap angles deployed

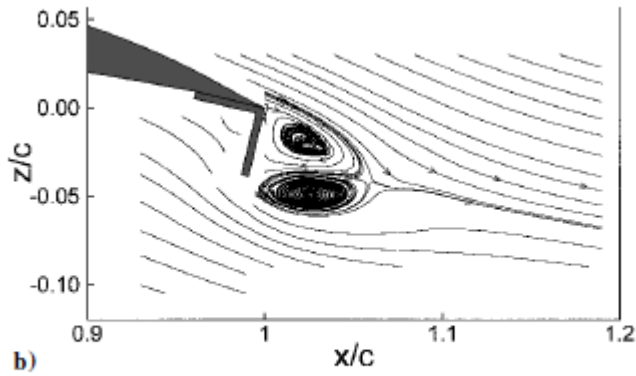


Fig. 7 Time-averaged LDA results: a) mean-velocity vectors, and b) streamlines (4% Gurney, $\alpha = 0.0$ deg).

Figure 59 Showing trailing edge vortex induced by Gurney flap

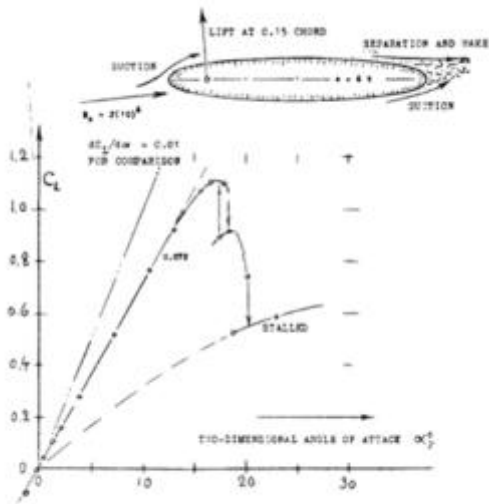


Figure 12. Lifting characteristics of a round-edged, elliptical section.

Figure 60 showing the trailing edge separation.

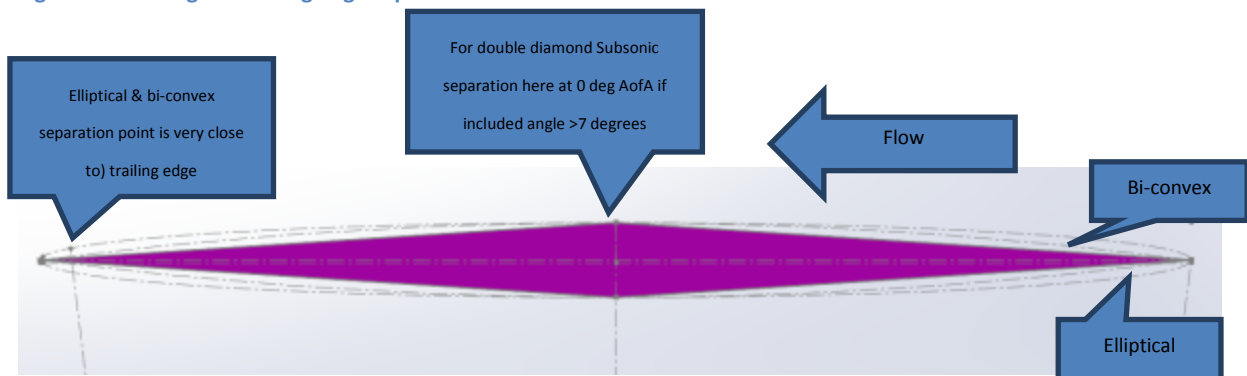


Figure 61 showing the relative sectional areas for a constant t/c value

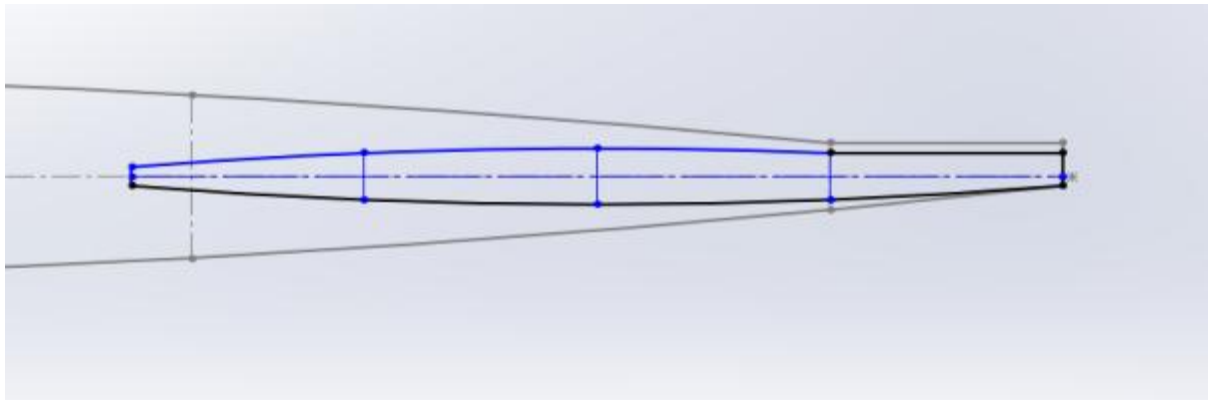


Figure 62 showing tip 100 mm chord section with truncated nose & integral face for Gurney flap location

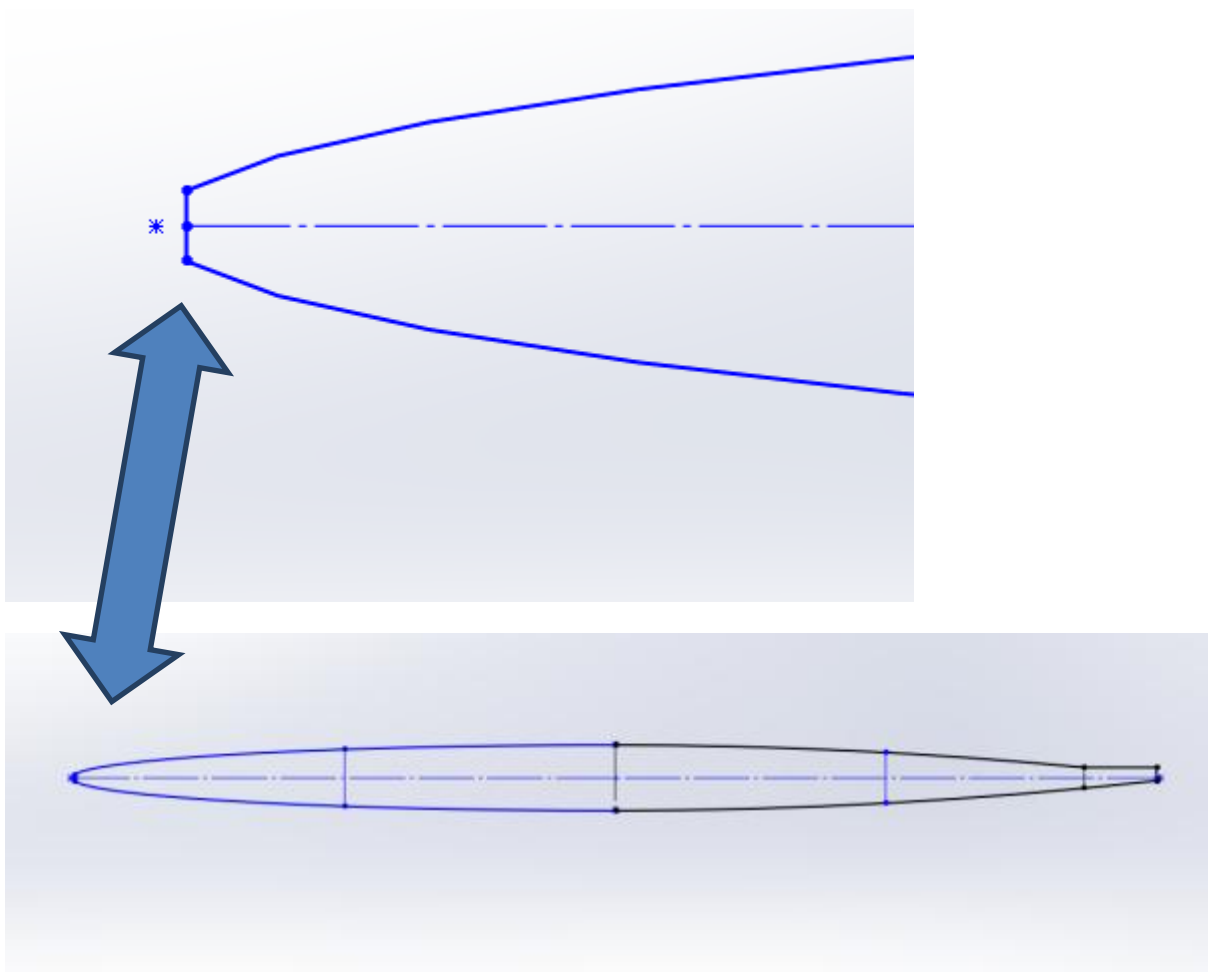


Figure 63 showing root 373 mm section with truncated nose & integral face for Gurney flap location

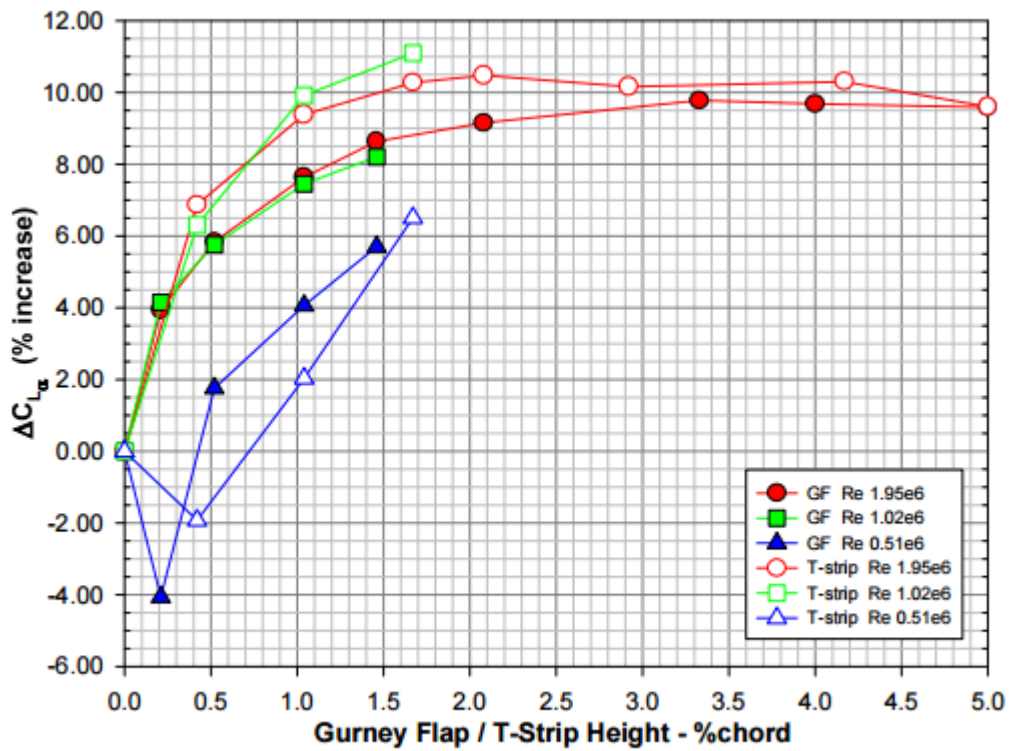


Figure 8. Wing Lift Curve Slope Increase Due to Gurney Flaps and T-Strips

Figure 64 Showing increase in lift coefficient rate due to gurney flap

$$C_{L\max} / C_{L0\max} = 1 + 1.9661 * (\Delta h / c)^{0.5442}$$

Figure 65 Showing empirical formula for Gurney flap of maximum CL

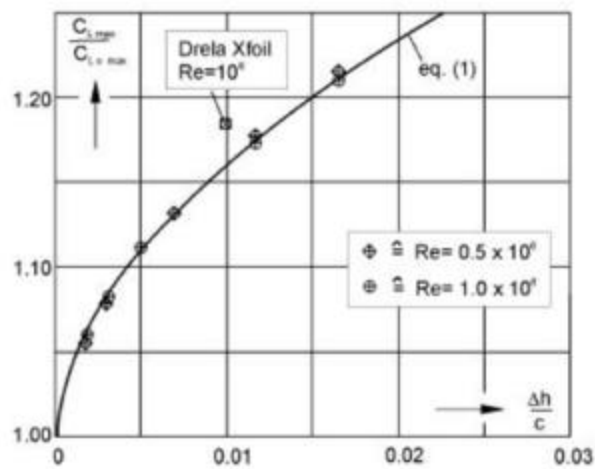


Fig. 8. The dependence of device drag and lift increase on Gurney flap height.

Figure 66 Showing correlation confident of Figure 65

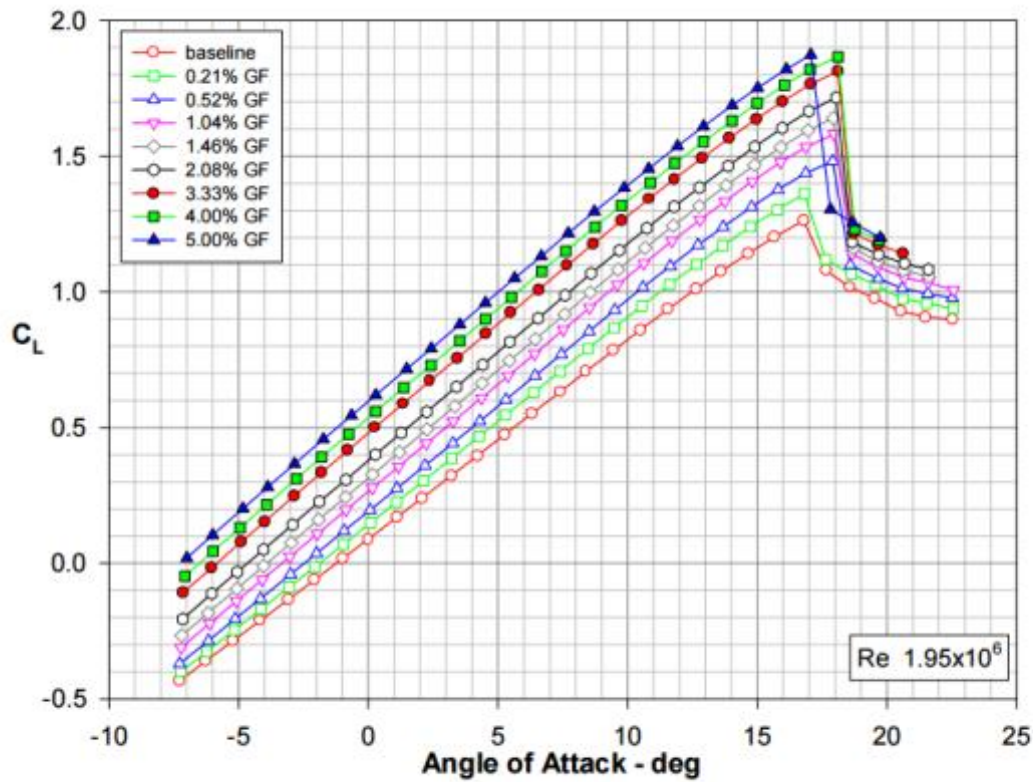


Figure 4. Effect of Gurney Flaps on Wing Lift Curve, $Re\ 1.95 \times 10^6$

Figure 67 Showing effect fo Gurney on lift curve slope change

Gurney h/c	C_{Lmax}/C_{L0max}
0.01	1.160
0.02	1.234
0.03	1.292
0.04	1.341
0.05	1.385
average per percent flap height	1.185

Figure 68 Showing empirically derived improvement rate per percentage of Gurney

Supersonic Model @M1.3	
	Gurney model to give target base drag angle
Chord	0.2607
flap proportion F	0.2
unflapped proportion UF	0.8
flap deflection angle (deg)	5.648376
flap deflection angle η (Radians)	0.098593
flap deflection distance (m)	0.005157
equivalent Gurney percentage	1.98%
Delta $C_N = F\eta \cos \eta$	0.019623
delta CN corrected for 3-D	0.0155
Moment arm from LE to flap midpoint (m)	0.23463
$C_{M LE}$	0.003637
Lift curve slope (From ESDU)	3.8036
Lift curve slope (2-D)	4.815434
distance from LE to cofp	0.12
CN induced moment (m/Rad)	0.12
Steady state angle (Rad)	0.03
Steady state angle (deg)	1.75

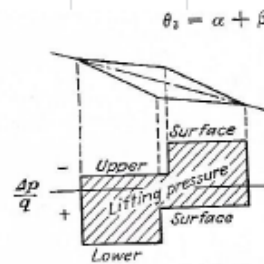


FIG. 4-4. Pressure distribution over symmetric double-wedge airfoil.

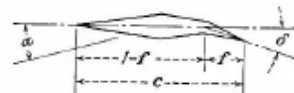


FIG. 4-15. Double-wedge airfoil with flap.

$$C_N = \frac{4\alpha}{\sqrt{M^2 - 1}} (1 - f) + \frac{4(\alpha + \delta \cos \delta)}{\sqrt{M^2 - 1}} f$$

$$= \frac{4}{\sqrt{M^2 - 1}} (\alpha + f\delta \cos \delta)$$

Figure 69 Showing prediction of flap effectiveness using supersonic theory

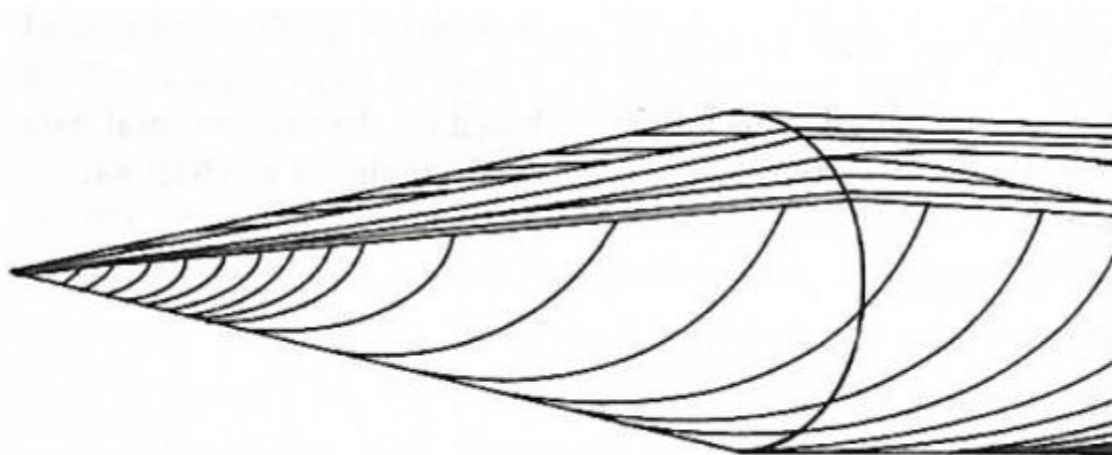


Figure 70 Showing 3-Dimensional flow over a conical form

Converging on a final configuration

Because the gurney flap depth is in the order of 2% of the chord thickness, this leads to a thin structure. Pragmatically this may prove difficult to machine, and so the following solution is proposed to see Figure 71, Figure 72 and Figure 73.

Some of the required flap height is used to make a flat portion on the underside of the canard surface. To give a nominal width at the 260.7mm chord station of 20mm. This will then become a permanent built-in camber change to the profile. Onto this surface strips of steel of varying thickness from 2 to 5 mm thick are then to be bolted in place. The strips may be tapped with an M5 thread to remove the need to use nuts. To opposite surface has a spot face and countersink so that a countersunk M 5 set screw may be used. This should be maintained in position using Loctite or similar. Thus keeping disruption to the flow on that side to a minimum.

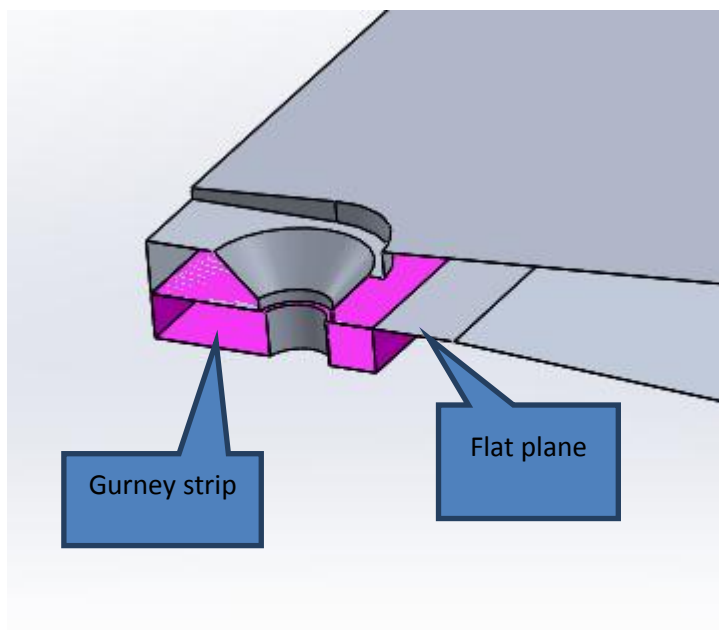


Figure 71 showing a local section through Gurney strip proposal

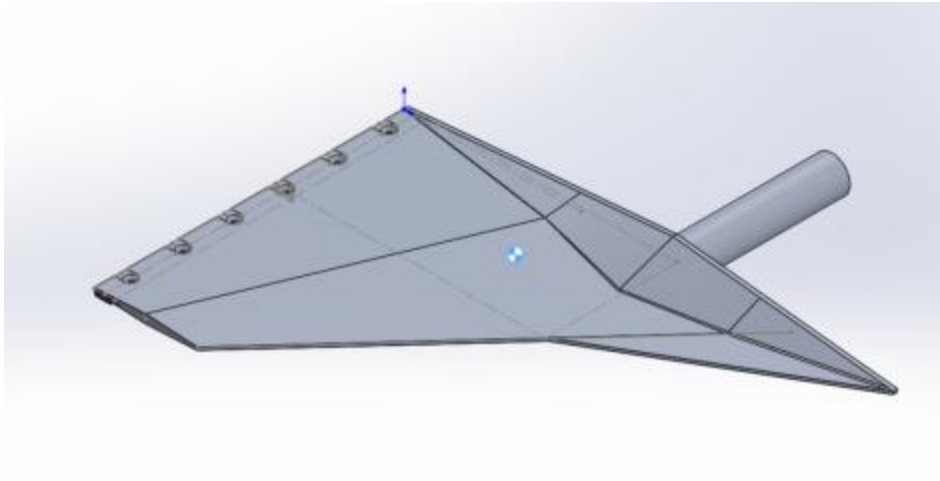


Figure 72 showing the countersinking details on the upper surface

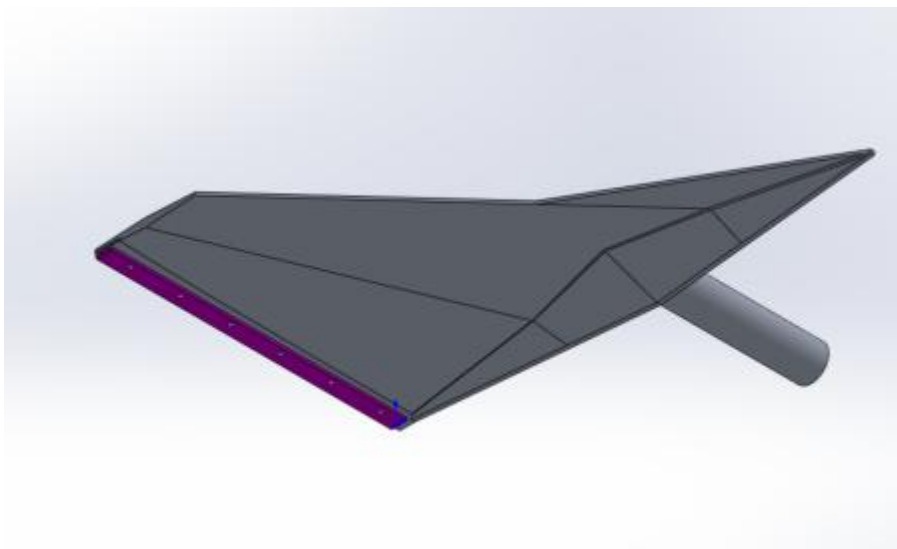


Figure 73 showing the Gurney strip in-situ on the lower surface

Canard first-pass stress calculations.

General.

Initial calculations were carried out on the double wedge proposal. They are inherently simplified and are designed for quick iterations and as a means to verify later FEA results. The bending and shear stresses were calculated at intervals of 50 mm from an offset distance of 4 mm from the root, see Figure 76 and Figure 77. The section used initially was a 3.5 % thickness triangular shape. To avoid the leading and trailing edges being a knife point (which would be difficult to machine but an ideal situation for a delta) the triangular sections sandwich a 3 mm thick plate, thus giving a 7.7% t/c ratio at the root and 10% at the tip. The root section chord is 374 mm which is a projection of the leading edge line to the root. The real root chord is 474 mm, but this is to ensure that there is sufficient sectional thickness for the trunnion placement. The minimum factor of safety is, in fact, the trunnion and is in the region of 4.57 based on using 7075 aluminium and represents less than 1500 microstrains. It would be possible to use a lower cost 6061-T6 with a yield of 276 MPa reducing the FOS to a healthy 2.37 but as we will see modifications would be required in the bearing region. The properties for 7075 are shown in Figure 75 though these have knock-down factors. The Yield value for 7076 T6 is quoted at 503 MPa, and this was used to calculate tensile factors of safety

Bearings.

The limiting condition for the trunnion shaft is the bearing induced contact stresses. Using the Hertzian method (Figure 78) and assuming a shaft clearance of maximum 0.25 mm to the inner diameter of the bearing, then with an aluminium shaft the maximum permissible load becomes 4241 N (Figure 79). This also assumes that the bearing ID and width is 50 mm. This load becomes the limiting factor in the minimum spacing requirements between the bearings (127 mm) of which the calculations are summarised in Figure 79. The required sizing for of the Trunnion is this shown in Figure 81. 6061 has a much lower bearing yield stress which is 1/3 that of 7075 and so precludes its use at this stage.

Finite Element Investigation.

The first model created of the canard was of 18604 tet10 elements final analysis versions were more than 80k elements. The load applied was -0.028556 N/mm^2 because the model is scaled in mm. The faces of elements in the region of the trunnion were constrained to represent a build in condition. This corresponds to a total load of 1999 N applied over a surface area of 0.07 m^2 . This would produce a load case that was more aggressive than would be seen. This is because in reality the pressure distribution over the canard is not even and so the centre of pressure of it and the model do not coincide. However, the relative positions are determinable and can be corrected for (Figure 74).

The assumption is made that applying a pressure uniformly over the surface will yield a result of sufficient accuracy to identify regions of the canard that require further investigation (Figure 82). The results for the principal stress are encouraging and show reasonable agreement with the classical calculations considering that in their case the load was point applied about the centre of pressure (Figure 83). The study did identify a stress hot spot in a region of the trunnion mount (Figure 84). As expected this would tend towards the aft side of the interface between the trunnion and wing where the bending moments are greater. As with all, this model has limitations even at this number of elements as it will discretise the region abruptly rather than model a radius. The actual model has a 3 mm fillet radius all round, with the bearing contact stresses dictating a trunnion diameter of 50 mm and the thickness of the canard at that section approximately 36 mm this put the D/d ratio at 1.4 and r/d at 0.08. As the bending and torsional moments induced but the centre of pressure are approximately the same the actual stress concentration factor will lie somewhere between the two values at approximately 1.6 i.e. the maximum stress is under 70 MPa.

Parenthetically, final models showed this to be around 60 MPa

For completeness, it is noted that a correction of the stress results needs to be made to take into account the differences in the stream-wise and span-wise moment arms. The span-wise centre of pressure is the same for M 0.9 is shown in Figure 74 along with the resultant of the constant pressure approach. The correction factor is the RMS value of the x and y coordinate ratios from the trunnion centreline.

$$= \text{SQRT}[(80/117.7)^2 \times (161/117)^2] = 0.875$$

The value of overestimation at M 0.9 is estimated about 12.5%

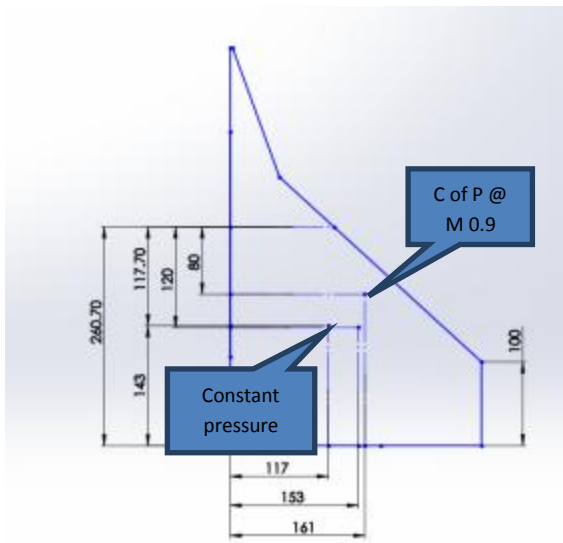


Figure 74 showing M 0.9 C of P position relative to the constant pressure resultant centre

MATERIAL ALLOWABLE STRENGTH DATA

Material Designation		7075	
Data Source Reference		Mil-Hdbk-5 Iss H Tables 3.7.4.0 (b1,b2,b3,b4,c1 c2,c3,c4,c5,d,e1, e2,f1,f2,g1,g2,g3, g4)	
Available Forms		Sheet & Plate. Bar, Rods & Shapes, rolled, drawn or cold finished. Die & Hand Forgings. Extruded Rods, Bars and Shapes. Clad Figures Included.	
Heat Treatments and Tempers		T6, T62, T651,T6510, T6511, T652, T73, T7351, T73510, T73511, T7352, T76, T7651, T76510, T76511	
Young's Modulus	X 10 ³ ksi	E	9.3
	GPa		64
Density	lb/in ³	ϖ	0.101
	g/cm ³		2.80
Ultimate Tensile Strength	ksi	F _{TU}	56
	MPa		386
Tensile Yield Strength	ksi	F _{TY}	44
	MPa		303
Ultimate Shear Strength	ksi	F _{SU}	35
	MPa		241
Ultimate Bearing Strength	ksi	F _{BRU}	84
	MPa		579
Yield Bearing Strength	ksi	F _{BRY}	68
	MPa		469

Figure 75 showing 7075 allowable properties

Canard coarse cut stress sizing calculations							
Reference dimensions							
local chord base airfoil (m)	0.374	0.328	0.283	0.237	0.191	0.146	0.100
y station (m) taken from 4mm initial offset	0	0.05	0.1	0.15	0.2	0.25	0.3
thickness of central portion (m)	0.003	0.003	0.003	0.003	0.003	0.003	0.003
triangular section max thickness either side of central portion (m)	0.013	0.011	0.010	0.008	0.007	0.005	0.004
second moment of area (I _{xx}) of triangle about centroid (m ⁴)	2.33E-08	1.38E-08	7.60E-09	3.76E-09	1.60E-09	5.36E-10	1.19E-10
area of triangular portion A (m ²)	2.45E-03	1.89E-03	1.40E-03	9.83E-04	6.41E-04	3.71E-04	1.75E-04
triangular centroid height (m)	4.36E-03	3.83E-03	3.30E-03	2.77E-03	2.23E-03	1.70E-03	1.17E-03
Bending stresses							
I _{xx} triangular = I _{xx} + Ad ²	6.99E-08	4.15E-08	2.28E-08	1.13E-08	4.79E-09	1.61E-09	3.58E-10
central portion second moment of area I _{xx} central	8.415E-10	7.38758E-10	6.36E-10	5.33E-10	4.31E-10	3.28E-10	2.25E-10
Total second moment of area 2*I _{xx} Triangular + I _{xx} central	1.407E-07	8.379E-08	4.626E-08	2.308E-08	1.001E-08	3.547E-09	9.402E-10
Maximum expected load of canard half (kN)	1.99						
bending moment arm (m)	0.172	0.122	0.072	0.022			
equivalent percentage of 300mm span	57.33%	expected to be around 60% from previous studies					
bending moment (Nm)	342.87	243.19	143.51	43.83			
Maximum local bending stress (MPa)	35.57	37.71	35.35	18.60			
Torsional stresses							
equivalent sectional constant thickness based on total second moment of area (m)	1.65E-02	1.45E-02	1.25E-02	1.05E-02	8.56E-03	6.64E-03	4.83E-03
torsional shape contant K	5.63E-07	3.35E-07	1.85E-07	9.23E-08	4.00E-08	1.42E-08	3.76E-09
local section shear/torsional centre. Measured from trailing edge (m)	0.237	0.164	0.141	0.119	0.096	0.073	0.050
distance from centre of pressure t measured from trailing edge(m)	0.18	0.18	0.18	0.18	0.18	0.18	0.18
distance from centre of pressure to local section shear centre measured from trailing edge(m)	0.06	-0.02	-0.04	-0.06	-0.09	-0.11	-0.13
torsional moment (Nm)	111.66	0.00	0.00	0.00	0.00	0.00	0.00
Torsional stress (MPa)	13.29	19.61	30.63	51.63			
Principle stresses MPa							
σ _x	35.57	37.71	35.35	18.60	$\sigma_1 = \frac{\sigma_x + \sigma_y}{2} + \sqrt{\left(\frac{\sigma_x - \sigma_y}{2}\right)^2 + \tau_{xy}^2}$ $\sigma_2 = \frac{\sigma_x + \sigma_y}{2} - \sqrt{\left(\frac{\sigma_x - \sigma_y}{2}\right)^2 + \tau_{xy}^2}$		
σ _y	0	0	0	0			
τ _{xy}	13.29	19.61	30.63	51.63			
σ ₁	39.99	46.06	53.03	61.76			
σ ₂	-4.42	-8.35	-17.69	-43.16			
Minimum FOS using σ yield 7075	13	11	9	8			

Figure 76 Showing summary of spreadsheet stress calculations at various spanwise stations

Pivot trunion	diameter (m)	0.035
second moment of area (m ⁴)	7.37E-08	
maximum bending stress at root σ_x (MPa)	81.46	
polar second moment of area (m ⁴)	1.47E-07	
maximum torsional stress (MPa)	13.26	
maximum direct shear stress (MPa)	2.76	
τ_{xy}	19.23	scf estimated at 1.2
σ_1	106.13	scf estimated at 1.5
Minimum FOS using σ yield 7075	4.74	

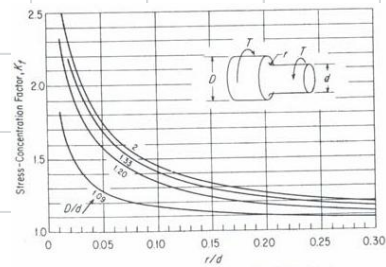


Fig. 4. Stress-concentration factor, K_t , for a filleted shaft in torsion*

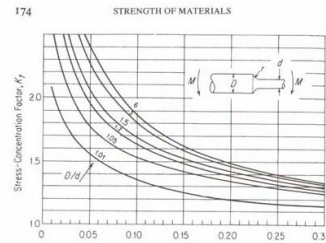


Fig. 5. Stress-concentration factor, K_t , for a shaft with shoulder fillet in bending*

Figure 77 Showing summary of pivot trunion calculations and stress concentration factors used

Cylinders in Contact (contd.)

- The equations for two cylinders in contact are also valid for:
 - Cylinder on a flat plate (a flat plate is a cylinder with an infinitely large radius)
 - Cylinder in a cylindrical groove (a cylindrical groove is a cylinder with a negative radius)

ME EN 7960 – Precision Machine Design – Contact Stresses and Deformations 7-10

Figure 78 Showing Hertzian contact stress model used

contact stress in trunnion bearings				
shaft material		aluminium		
Poisson's ratio	mu	0.3		
Young's modulus	E	6.90E+10	Pa	
K1		1.32E-11		
bearing contact face width	L	0.050	m	
diameter (assumes 0.25 mm diametric clearance)	D1	0.04975	m	
	R1	0.02488	R1=0.5D1	
bearing material		steel		
through Poisson's ratio	mu	0.28		
Young's modulus	E	2.10E+11	Pa	
K2		4.39E-12		
local radius		0.025		
(1/R ₁ +1/R ₂)		80.201		
load	F	4241	N	
Semi-width of rectangular contact area at the point of application	b	1.54E-04	m	
maximum contact pressure at the interface	Pmax	2F/πbL	351	M Pa set at 0.5 of 7075T6 bearing yield

Figure 79 showing a summary of maximum load for limiting contact stress

Bearing spacing	
Width of bearing (mm)	50
Distance from span-wise position of centre of pressure to outer bearing centre line (mm)	200
yield strength of 7071-T6 (MPa)	503
estimated bearing yield strength	704.2
working FOS	2
allowable yield strength (MPa)	352.1
outer bearing load (N)	4241
Max load at centre of pressure (N)	1993.611
inner bearing load (N) Sum up forces =Sum down Forces	2248
Distance between bearing centre-lines (mm)	177
Gap between bearings (mm)	127

Figure 80 showing a summary of the calculations to determine the minimum bearing spacing

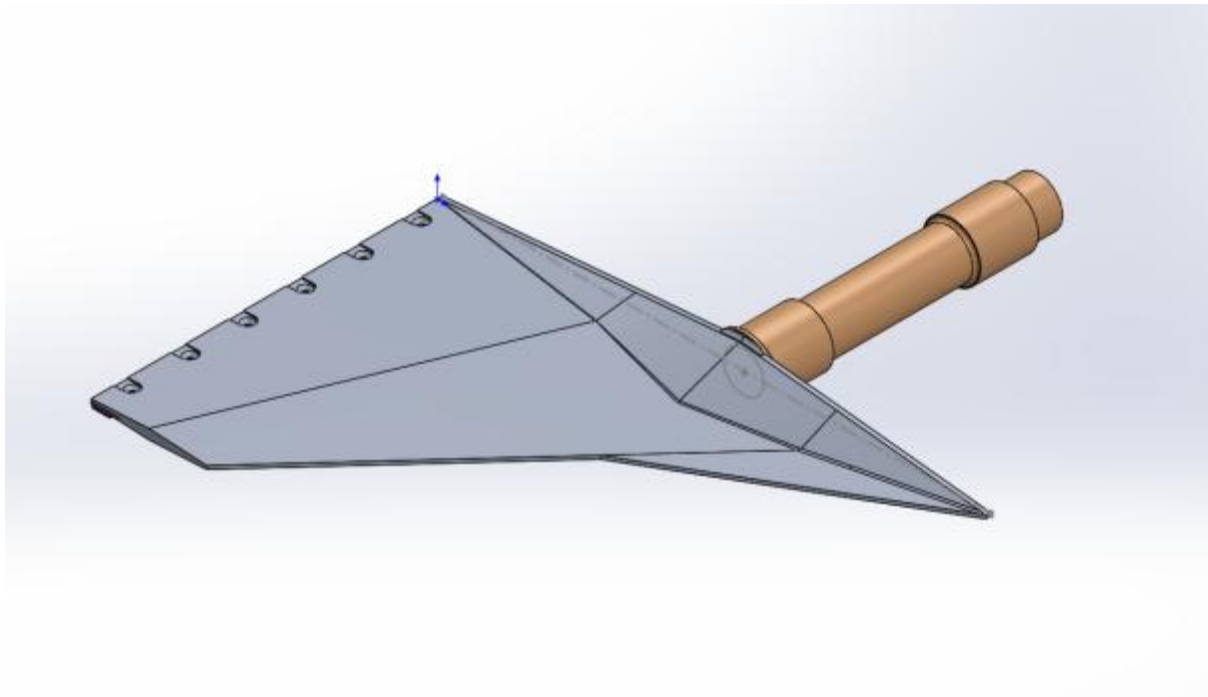


Figure 81 Showing required trunnion form

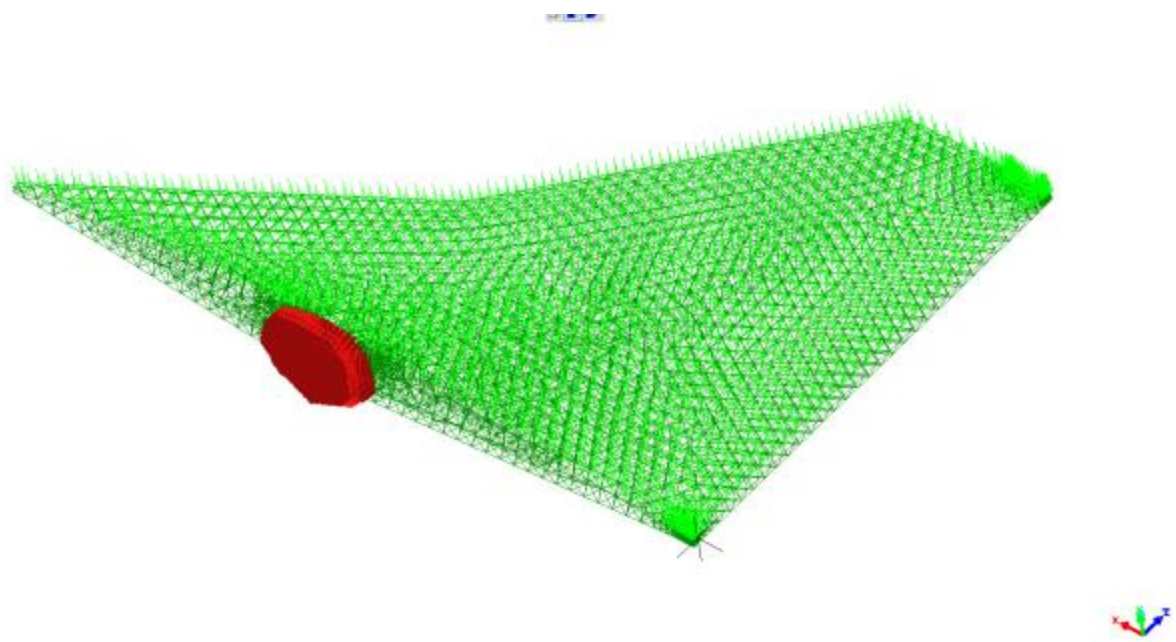


Figure 82 Showing pressure applied and constraint in trunnion region

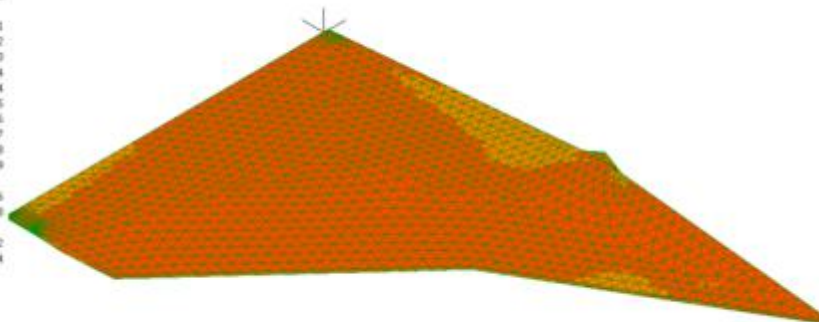
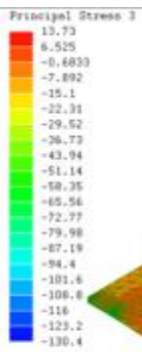
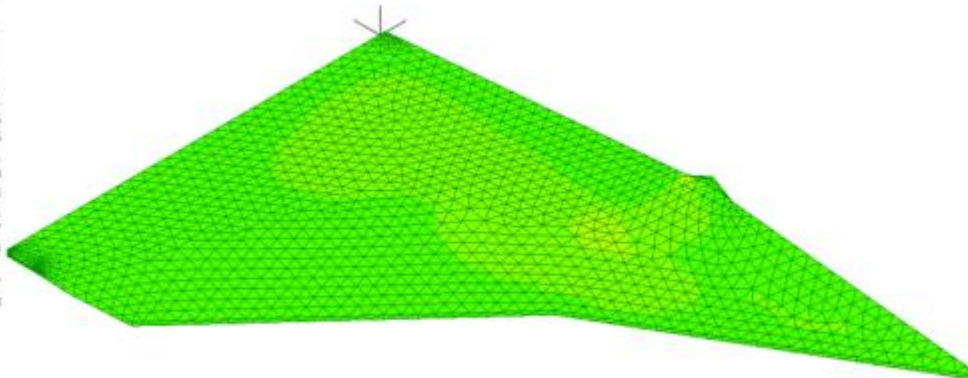
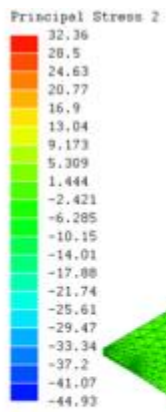
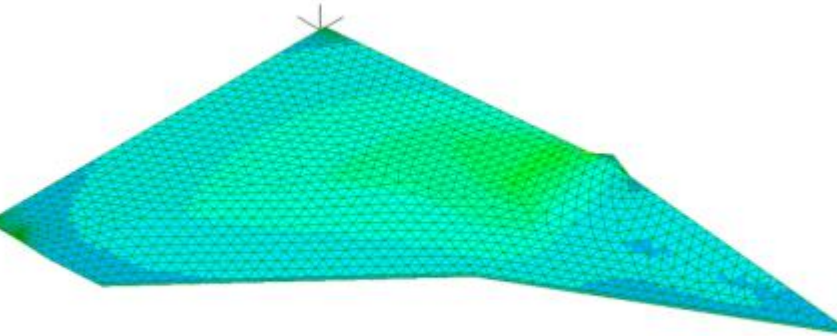
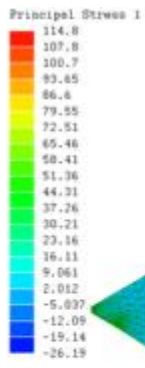


Figure 83 showing principle stress with loads and constraints as defined in Figure 83

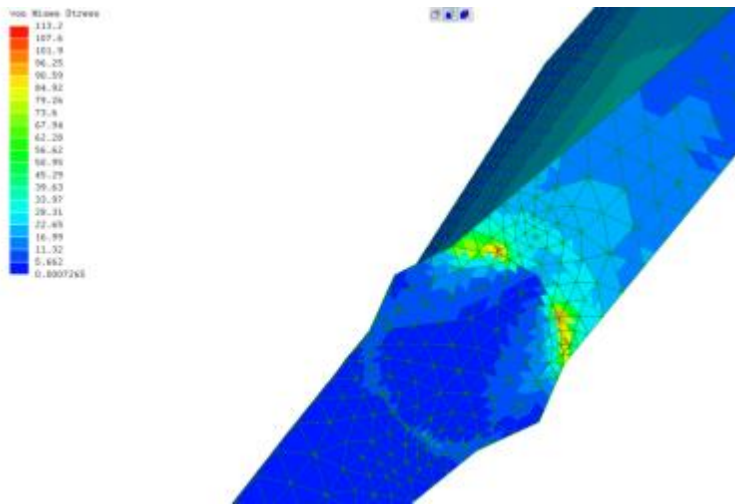


Figure 84 showing the local stress raiser around trunnion constraint.

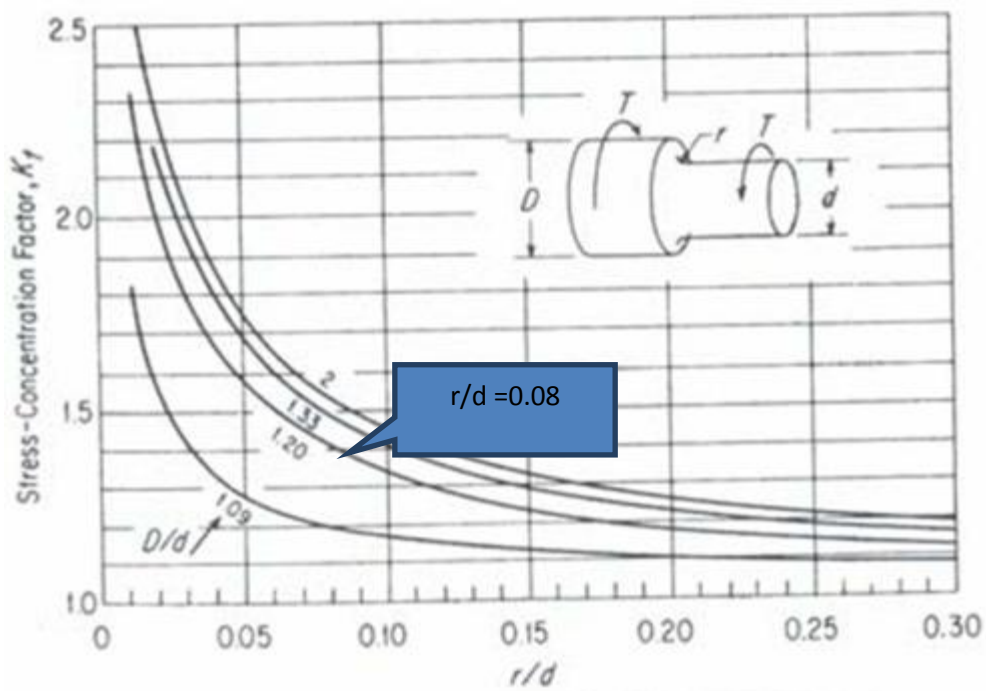


Fig. 4. Stress-concentration factor, K_t , for a filleted shaft in torsion*

Figure 85 showing stress concentration factor expected under a torsional loading

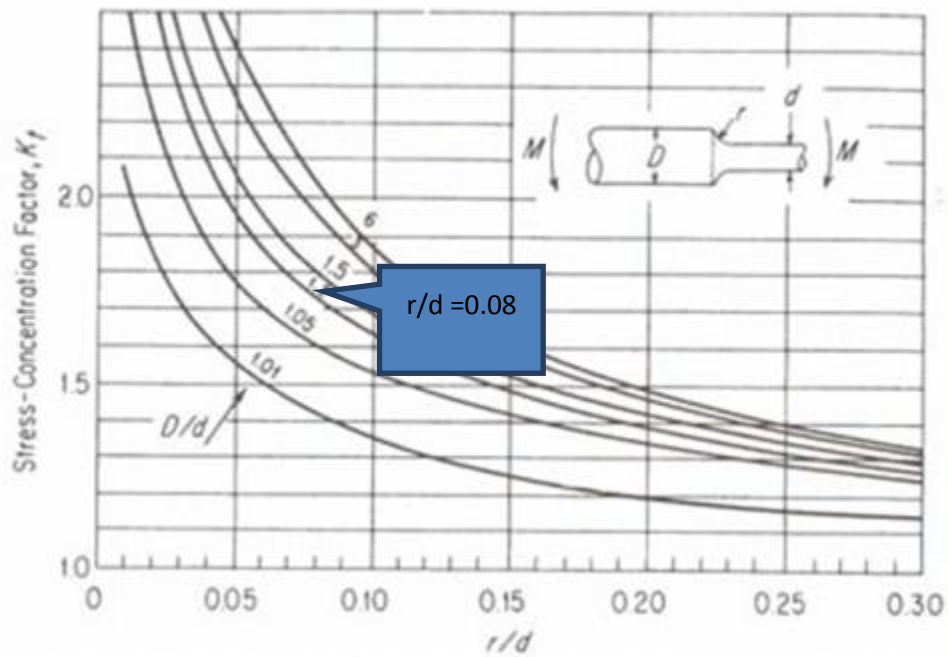


Fig. 5. Stress-concentration factor, K_t , for a shaft with shoulder fillet in bending*

Figure 86 showing the stress concentration factors expected under a bending induced moment

Divergence and Flutter.

When designing wing structures in the low to mid subsonic range if the structure is found to be strong enough, it is usually stiff enough as well. At higher velocities, sufficient strength is not sufficient, and the limitations become dependent on aeroelastic properties of the structure. This section sets out to identify potential sizing issues. The caveat to this is many of the assumptions are based on an incomplete vehicle or limited data. It is by nature an iterative process, and the result will either be to push the performance of the structure out of the expected operating realms or identify operational hot-spots to avoid.

Divergence is not a concern for this design it is a situation where the angle of attack (usually at the tips) increases with speed leading to increased lift and deflection leading to even higher angles of attack. In essence a vicious circle. Fortunately, because of the delta profile, it has significant sweepback, and because of this the wing cannot diverge. It consequently does not have a limiting divergence velocity, and analysis is unnecessary.

As for flutter, because the canard is free floating the only corrective moment about the trunnion pivot is that induced aerodynamically. Essentially the lift, which is a force, for any given speed is said to act about the centre of pressure. That has a determinable distance between in and the trunnion pivot axis thus creating a moment. That moment over the angle of attack ranges the canard is expected to operate at may be considered linear. Thus it is possible to model this as a torsional spring. When a unit load is applied to this spring at a distance between the centre of gravity and the trunnion pivot, the angle of twist can be determined.

This is the angle that is taken up as the equilibrium point between the moment induced by the mass of the canard (multiplied by g) and the centre of pressure moment previously described. From the distance of the centre of gravity and the angle of attack a vertical displacement can be determined. Thus the torsional spring may be replaced by an equivalent one, and for small angles the linearity still holds true. The natural frequency of a single degree of freedom system of spring and mass can be calculated using the formula

$$f_n = 1/(2\pi) \cdot \sqrt{k/m} \text{ (Hz)}$$

where;

f_n is the natural or resonance frequency

k is the spring constant N/m

m is the mass kg.

A study was undertaken with one side of the canard. Using the mass derived from the CAD model (2.8 kg) the centre of pressure and lift coefficient/ Radian from the ESDU graphs the natural frequency of the system could be determined. It yielded a natural frequency at M 1.3 of 61 Hz. What needs to be determined is if this value is likely to be excited. There are low, medium and high frequencies generating elements in the vehicle which depending on the speed can be sources of excitation. The high frequencies (hi order vibration) would be due to the engine. The medium by large cycling masses such as the wheels and the low due to large turbulent eddies forming (Figure 93). Because the vehicle is designed to operate at supersonic velocities, we are fortunate that only those elements upstream of the canard are likely to have an effect. Vibration due to pressure waves either as a result of the engine or turbulence at the rear of the vehicle cannot move ahead of the sonic line.

Wheel induced vortices

Upstream of the canard, there are two wheels. They have a natural frequency due to their rotation as no disc can ever be balanced perfectly. Also, due to the blockage created the airflow will be forced sideways and flow may separate. Flow separation may be attributed to the change in lift coefficient between with and without from wheel conditions on the wind tunnel testing of the Blue Flame so that it will be significant. It is likely that one of the harmonics of the vortices shed will correspond to the wheel frequency.

Turbulent prediction is difficult, even with advanced CFD techniques, as it is decidedly non-linear and is beyond the scope of this report. However, with reasoning, if the system is designed so that its natural frequency is a healthy margin and one that is not a whole number multiple of the frequency induced by the wheel then it will be a safe starting point.

The shape of the nose has an integrated fairing ahead of the wheel. If this fairing is approximated to a semi-circular section of diameter equivalent to the total wheel width approximately 0.45 m (*remembering there are two wheels side-by-side at the front*) and the rear exposed wheel behave similarly to the rear half of a circular section. A very coarse approximation can be made regarding vortex shedding frequency. This model is expected to be aggressive as a cylindrical profile will tend to shed distinct Von Karmen vortices where as the wheel acting as a fin will tend to suppress them (Figure 90). The Reynolds number varies with vehicle velocity from zero to almost 13 million. Figure 89 suggests a Strouhal number of between 0.21 and 0.28 for the range of vehicle velocities of concern.

Because $St = f \cdot L / U_{\infty}$

Where

St = Strouhal number.

F = frequency

L = characteristic length

U_{∞} = free stream velocity.

The frequency becomes the vehicle velocity x ratio of the characteristic length (0.45 m) to Strouhal Number, and this can be plotted.

Suspension Frequencies

The natural frequency of the suspension system can be determined for both the front and rear and pitching situations. This frequency will change during the run as the fuel is burned up and the mass reduces, so the values during acceleration and deceleration will be significantly different. The approach taken was to determine the rear values as these are relatively easy to quantify. Then size the front natural frequency, so it is lower than the rear, in line with race car suspension practices. As a sanity check, the Olley criteria was used whereby for a “*comfortable ride” the ratio of the bounce to pitch frequency should be less than 1.2. ** Not that any ride above about 1.5 Hz could be classed as comfortable!*

The current assumption is that the full vehicle at the start of the run has a mass of 9200 kg and the empty mass is 6400 kg. The rear suspension is a solid axle of 125 mm in diameter thus it is possible using the lumped mass approach to determine the natural frequency. This will be a range due to the mass of the vehicle and the change in distribution between the front and rear during the run. The track of the vehicle at the rear is 2.447 m and the wheelbase 12.1 m

Four conditions were modelled. Conditions A and B were with full tanks and assumed the percentage mass on the rear was 55% and 45 % respectively. Conditions C and D were with empty tanks and again with 55% and 45% assumed rear mass. A summary of the calculations is shown in Figure 87, and the results of bounce and pitch frequencies tabulated in Figure 88.

An interference diagram can be created that combines the vortex and suspension natural frequencies to identify potentially troublesome issues. Figure 94 suggests that there is a possibility of harmonics resonance with each other at low velocities, but as these are circa $M 0.1$, it is very unlikely to cause an issue. It is anticipated that one of the natural frequency of the canard will be circa 100 Hz. The value being an output of the FEA work later in this report.

As the frequencies derived, using the Strouhal Number is the highest of the system and subject to the greatest error it was decided to use the rotational frequency of the wheels as an upper limit. Figure 91 summarised the rotational frequency of the wheels for a range of Mach numbers. The maximum value is 157 Hz; Figure 92 is a summary of the spreadsheet calculations its shows that the ratio of the wheel and canard frequencies approach the value of 2 at the limit. To improve on this, a counterweight mass system is proposed. By having it in front of the trunnion pivot position Figure 100, this moves the centre of gravity of the whole system towards the trunnion and possibly beyond. It is an iterative process. The “sweet spot” is one that;

- Minimised the masses involved,
- Minimises the counterbalance moment arm, for packaging purposes and not to incite additional bending resonances in the counterbalance arm.
- Yields a natural frequency value at M 1.3 of 157 Hz or higher, else has a natural frequency at a low transient velocity.
- When a comparison is made against the natural frequency of the rotation wheel, the ratio is not a whole figure or within 10% of a whole figure.

Figure 99 summarised the result of that study and suggests the “sweet spot” is a mass of 1.47 kg with its centroid 165 to 183 mm forward of the trunnion pivot position. Figure 101 and Figure 102 are a series of sanity check calculations to determine how sensitive the arrangement would be to horizontal and vertical g-forces. If one counterbalance were required for both sides i.e. the total canard, then the mass would be doubled. Figure 103 is an attempt to explain how the canard, the Gurney and the counterbalance work as a system.

A15R SUSPENSION NATURAL FREQUENCY MODELLING							
	mass full (kg)	9200	total wheel & hub masses (kg)	1444	sprung mass (kg)	7521	
	mass empty (kg)	6400			sprung mass (kg)	4721	
	axle diameter (m)	0.125			taken as 4 x wheel disk envelope mass less axle mass		
	axle c.s.a (m ²)	0.012271846	material density (kg/m ³)	7800	axle mass(kg)	234	axle semi mass (kg)
	axle second moment of area (m ⁴)	1.19842E-05	material Young's Modulus E (Pa)	2.1E+11			
	track (m)	2.447					
	Wheel base (m)	12.1	<i>*F_{rear} / F_{front} ratio</i>	1.18	<i>*adjust to meet Olley's criteria for comfortable ride</i>		
Condition A Full fuel m 55% rear	Maximum rear sprung mass distribution	55.00%	minimum front mass distribution	45.00%	distance "b" front wheel CL to cofg (m)	6.655	distance "c" rear wheel CL to cofg
	mass rear (kg)	4137	mass front (kg)	3385			5.445
	k _{rear} (N/m)	8244581					
	F_{n rear} Hz	7.01	<i>F_{rear} / F_{front} ratio</i>	1.18			
	F_{n front} Hz	5.94			$l_y = 0.2154ML^2 = \text{pitch moment of inertia}$		
	l_y	237199			$K_{\theta} = (K_r b^2 + K_f c^2) = \text{pitch stiffness}$		
	k _{front} (N/m)	4711184			$f_{n \text{ pitch}} = \sqrt{K_{\theta} / l_y} / (2\pi) \text{ Hz}$		
	K _θ	453089276					
	f_{n pitch} (Hz)	6.96					
Condition B Full fuel 45% rear	Maximum rear sprung mass distribution	45.00%	minimum front mass distribution	55.00%	distance "b" front wheel CL to cofg (m)	5.445	distance "c" rear wheel CL to cofg
	mass rear (kg)	3385	mass front (kg)	4137			6.655
	k _{rear} (N/m)	8244581					
	F_{n rear} Hz	7.72	<i>F_{rear} / F_{front} ratio</i>	1.18			
	F_{n front} Hz	6.54					
	l_y	237199					
	k _{front} (N/m)	6994899					
	K _θ	572529391					
	f_{n pitch} (Hz)	7.82					
Condition C Empty 55% rear	Maximum rear sprung mass distribution	55.00%	minimum front mass distribution	45.00%	distance "b" front wheel CL to cofg (m)	6.655	distance "c" rear wheel CL to cofg
	mass rear (kg)	2597	mass front (kg)	2125			5.445
	k _{rear} (N/m)	8244581					
	F_{n rear} Hz	8.77	<i>F_{rear} / F_{front} ratio</i>	1.18			
	F_{n front} Hz	7.43					
	l_y	148896					
	k _{front} (N/m)	4635498					
	K _θ	449737235					
	f_{n pitch} (Hz)	8.75					
Condition D Empty 45% rear	Maximum rear sprung mass distribution	45.00%	minimum front mass distribution	55.00%	distance "b" front wheel CL to cofg (m)	5.445	distance "c" rear wheel CL to cofg
	mass rear (kg)	2125	mass front (kg)	2597			6.655
	k _{rear} (N/m)	8244581					
	F_{n rear} Hz	9.65	<i>F_{rear} / F_{front} ratio</i>	1.18			
	F_{n front} Hz	8.18					
	l_y	148896					
	k _{front} (N/m)	6858858					
	K _θ	568496045					
	f_{n pitch} (Hz)	9.83					

Figure 87 showing summary of calculations for a range of expected conditions

Summary of frequencies (Hz)	$F_{n \text{ Front}}$	$F_{n \text{ Rear}}$	$F_{n \text{ Pitch}}$	Olley's criteria for a good ride bounce to pitch frequency (front) <1.2
Condition A Full fuel m 55% rear	5.94	7.01	6.96	1.17
Condition B Full fuel 45% rear	6.54	7.72	7.82	1.19
Condition C Empty 55% rear	7.43	8.77	8.75	1.18
Condition D Empty 45% rear	8.18	9.65	9.83	1.20

Figure 88 showing a summary of bounce and pitch frequencies calculated in Figure 87

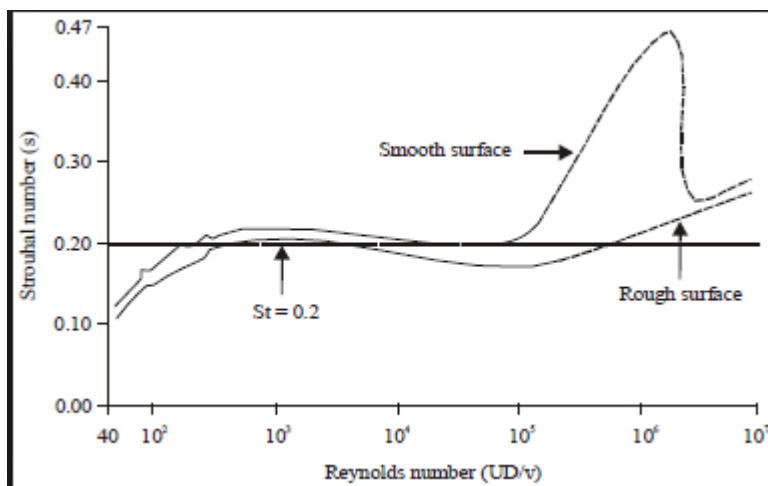


Figure 89 showing the relationship between Strouhal and Re numbers for a cylinder



Figure 90 showing vortex generation behind a cylinder with and without a fin

Mach No.		0.1	0.2	0.3	0.4	0.5	0.6	0.7	0.8	0.9	1	1.1	1.2	1.3
Wheel velocity m/s		34	68	102	136	171	205	239	273	307	341	375	409	443
wheel diameter (m)	0.9													
rotational speed Rad/s		76	152	227	303	379	455	530	606	682	758	834	909	985
rotational induced frequency 1st order Hz		12	24	36	48	60	72	84	96	109	121	133	145	157

Figure 91 showing the wheel rotational frequencies as a function of Mach No.

static pressure P_0	101325 Pa		canard 1/2 planform area $A_{1/2}$	0.07 m ²	Y		1.4		mass of 1/2 canard without trunnion CAD derived	2.82 kg		distance from trunnion pivot to CoG (non counterbalance) m CAD derived	0.096	
Mach No.	0.1	0.2	0.3	0.4	0.5	0.6	0.7	0.8	0.9	1	1.1	1.2	1.3	notes
q	709	2837	6383	11348	17732	25534	34754	45394	57451	70928	85822	102136	119867	0.5YP ₀ M ²
CL/α from ESDU	3.4438	3.4438	3.4438	3.4438	3.4438	3.4438	3.4438	3.5466	3.5466	3.8036	3.8036	3.8036	3.8036	indicate ESDU derived figure the rest are approx.
T _n centre of pressure from trunnion pivot (m)	0.080	0.080	0.080	0.080	0.080	0.080	0.080	0.080	0.080	0.120	0.120	0.120	0.120	indicate ESDU derived figure the rest are approx.
restoring torsional moment Lift x CoFP location (Nm/rad)	13.63	54.51	122.66	218.06	340.72	490.63	667.80	898.27	1136.87	2272.55	2749.79	3272.47	3840.61	A _{1/2} * q * CL/α * T _m
vertical spring constant based on mass without counterbalance	7.03E-03	1.76E-03	7.81E-04	4.39E-04	2.81E-04	1.95E-04	1.43E-04	1.07E-04	8.43E-05	4.22E-05	3.48E-05	2.93E-05	2.49E-05	twist for 1 N load
vertical component (m)	6.74E-04	1.68E-04	7.48E-05	4.21E-05	2.69E-05	1.87E-05	1.37E-05	1.02E-05	8.07E-06	4.04E-06	3.34E-06	2.81E-06	2.39E-06	based on 96 mm arm length
k vertical spring rate N/m	1.48E+03	5.94E+03	1.34E+04	2.38E+04	3.71E+04	5.34E+04	7.27E+04	9.79E+04	1.24E+05	2.48E+05	3.00E+05	3.56E+05	4.18E+05	
f _n = 1/(2π) √(k/m) (hz)	3.65	7.30	10.96	14.61	18.26	21.91	25.56	29.65	33.35	47.16	51.87	56.59	61.30	
frequency of wheel (hz)	12.06	24.12	36.18	48.24	60.30	72.36	84.42	96.48	108.54	120.60	132.66	144.72	156.79	target 127*1.15 = 146hz
check ratio of resonance frequencies for hot spots	3.30	3.30	3.30	3.30	3.30	3.30	3.30	3.25	3.25	2.56	2.56	2.56	2.56	harmonics likely at 2
mass of counterbalance (kg)	1.47	counterbalance moment arm from pivot centreline (m)	0.183	new total mass (kg)	4.29	new CoG position from trunnion pivot	0.000	remember counterbalance is in front of pivot						
new k vertical spring rate N/m	6.03E+05	2.41E+06	5.43E+06	9.65E+06	1.51E+07	2.17E+07	2.96E+07	3.98E+07	5.03E+07	1.01E+08	1.22E+08	1.45E+08	1.70E+08	
New natural frequency f _n = 1/(2π) √(k/m) (hz)	59.68	119.36	179.04	238.72	298.40	358.08	417.76	484.51	545.08	770.65	847.72	924.78	1001.85	
check ratio of resonance frequencies for hot spots	0.20	0.20	0.20	0.20	0.20	0.20	0.20	0.20	0.20	0.16	0.16	0.16	0.16	1.47 kg @ 183 mm is a sweet spot!

Figure 92 showing the natural frequencies for the “as is” system without counterbalance

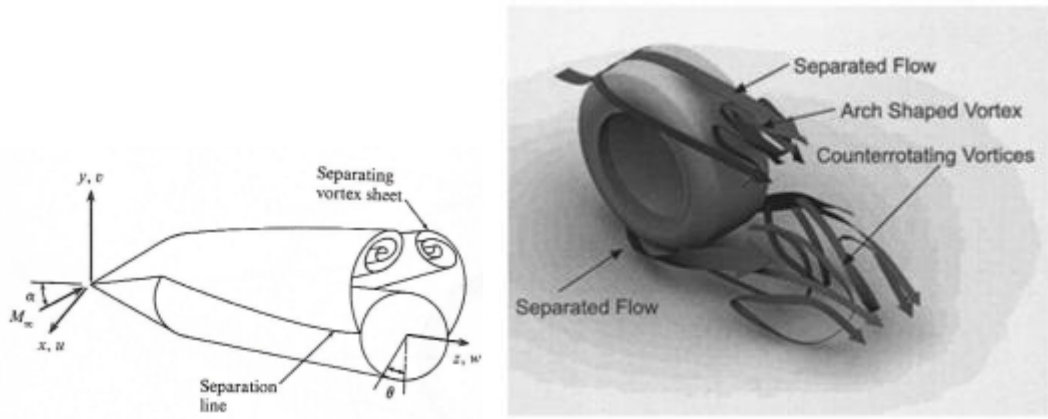


Figure 93 Showing low-frequency vortices due to form and around a rotating wheel

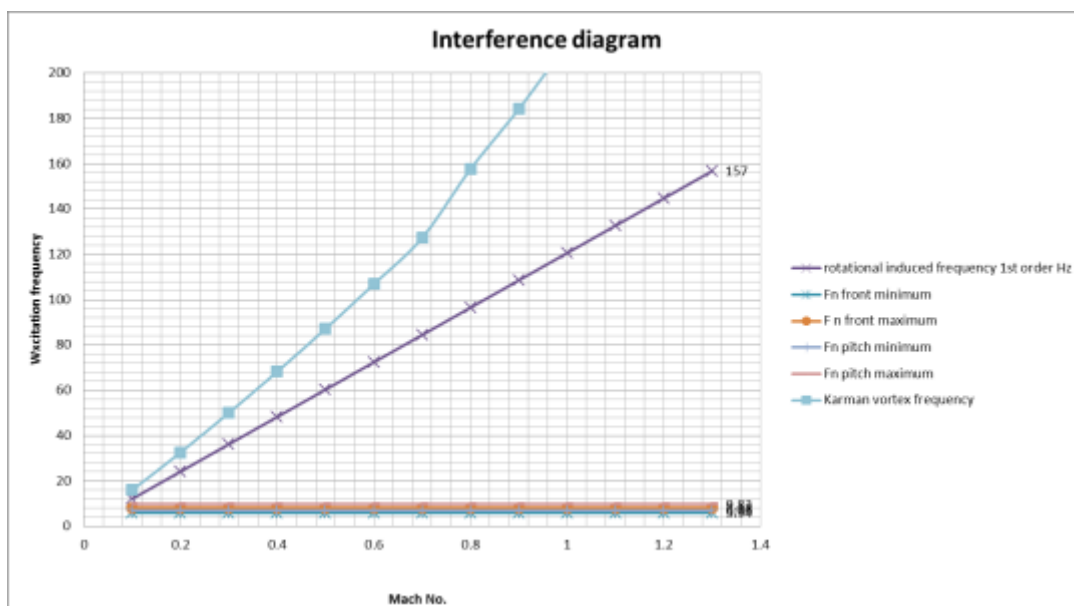


Figure 94 showing interference diagram of suspension and vortex frequencies

Bending and torsional natural frequencies.

The first step for this analysis was to create a coarse cut model to determine if bending resonance frequencies were likely to be an issue.

From the CAD data, the centroid of the semi-planform was 68.31 mm from the root, and this corresponds to a local chord of 311 mm.

The second moment of area for this section $I_{xx} = 6.814 \times 10^{-8}$ (Figure 97) This is less than the value for the trunnion section at the root and is conservative and would underestimate the natural frequency.

Using the beam deflection equation for a cantilever beam with a point load the system spring constant (k) may be determined.

$$\delta_{\max} = PL^3/(3EI_{xx})$$

P is the unit load 1 N

L = is the length = .0863m

E = Youngs Modulus for Aluminium 69×10^{09}

$$\delta_{\max} = 2.25 \times 10^{-8} \text{m}$$

$$\text{So } k = 1/\delta_{\max} = 44250646 \text{N/m}$$

Again from $f_n = 1/(2\pi) \cdot \sqrt{k/m}$ (Hz)

$f_n = 632$ Hz. Out of the range of interest.

The displacement magnitude was determined during the FEA analysis of which the majority was displacement in the vertical direction (Figure 96). The spring constant at the tip using this deflection of $1999/0.001924 = 1.03$ MN/m. The corresponding frequency based on a mass of 2.82 kg is $f_n = 96$ Hz.

Correcting the model for the differences between the centre of mass and the centre of the uniformly apply pressure (totalling 1999 N), this would raise the system stiffness by $1/0.875$ to 103 Hz.

This corresponds to a vortex shedding frequency at speed between M 0.8 and M 0.9. In reality, though it is unlikely, as the canard will not be situated in the vortex created by the existence of the front wheels.

It is too high above and too near in the axial direction for the vortex to have had sufficient time to expand to a radius that would cause interference.

Additionally, the acceleration and deceleration curves (Figure 135) suggest transversing a velocity increment of M0.1 in the high subsonic region will be measured in seconds. That isn't sufficient time for full flutter to manifest itself.

Based on these findings to create a natural frequency of the panel above M 1.3 would require a system k of 2.75×10^6 . Because the stiffness of the system is a function of the sectional second moment of area of the panel, this would suggest an across the board increase in the value of a factor of 2.66 is required.

The required sections of the double diamond profile are shown in Figure 98 and may be compared with the original values in Figure 97. The issue becomes the sectional thickness especially at the tip which is over 13%. Apart from being a significant rise in drag, the nature of the profile at subsonic velocities will lead to early separation of the flow shedding Von Karman type vortices resulting in additional flutter issues. To summarise, the double diamond will probably *"not cut the mustard!"*

The results from this study indicate the minimal sectional properties required, especially at the tip. An elliptical section for the same t/c will yield a higher second moment of area value when compared to the double diamond shape. Based on a minimum requirement of $2.5 \times 10^{-9} \text{ m}^4$ at the tip this yield an elliptical thickness of 8% which would be acceptable. Furthermore truncating the semi-span by 10 mm should add sufficient margin to push the natural frequency out of the potential excitation range.

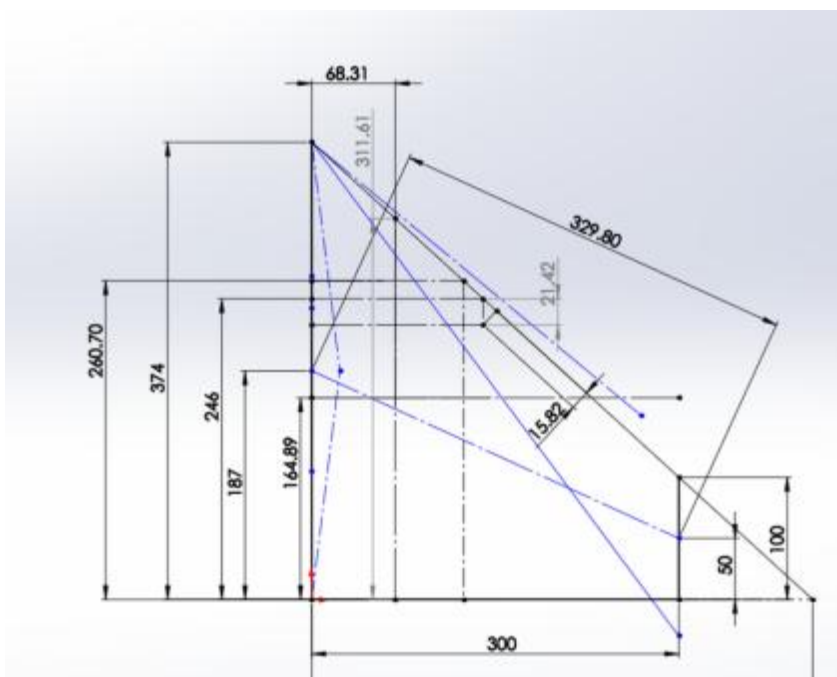


Figure 95 Chord at 68.31 mm using simplified profile

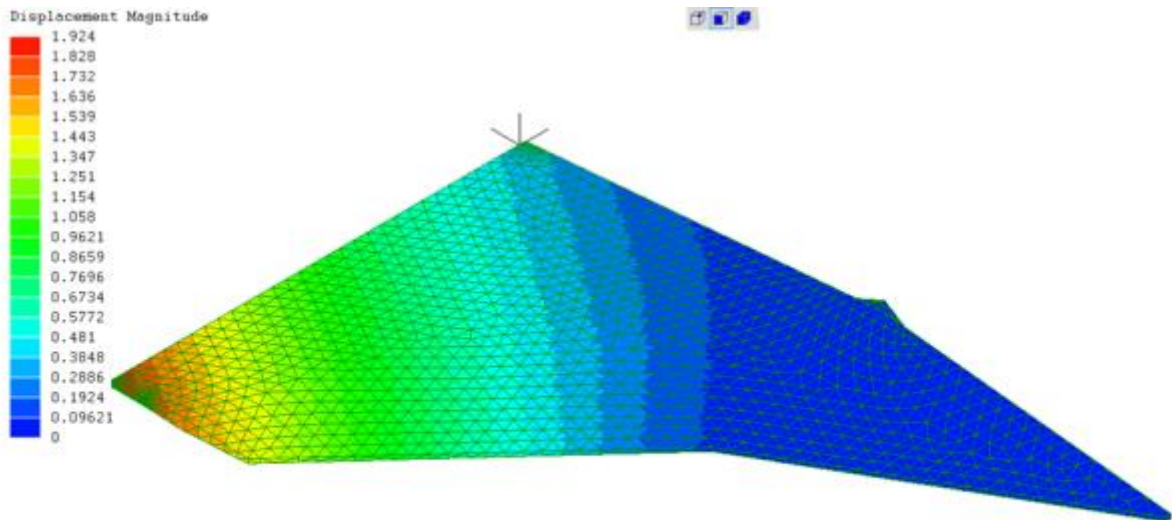


Figure 96 showing FEA derived tip deflection.

Reference dimensions								
local chord base airfoil (m)	0.035	0.374	0.328	0.283	0.237	0.191	0.146	0.100
y station (m) taken from 4mm initial offset	-0.003	0	0.05	0.1	0.15	0.2	0.25	0.3
thickness of central portion (m)		0.003	0.003	0.003	0.003	0.003	0.003	0.003
triangular section max thickness either side of central portion (m)	7%	0.013	0.011	0.010	0.008	0.007	0.005	0.004
second moment of area (I_{xx}) of triangle about centroid (m^4)		2.33E-08	1.38E-08	7.60E-09	3.76E-09	1.60E-09	5.36E-10	1.19E-10
area of triangular portion A (m^2)		2.45E-03	1.89E-03	1.40E-03	9.83E-04	6.41E-04	3.71E-04	1.75E-04
triangular centroid height (m)		4.36E-03	3.83E-03	3.30E-03	2.77E-03	2.23E-03	1.70E-03	1.17E-03
Bending stresses								
$I_{xx \text{ triangular}} = I_{xx} + Ad^2$		6.99E-08	4.15E-08	2.28E-08	1.13E-08	4.79E-09	1.61E-09	3.58E-10
central portion second moment of area $I_{xx \text{ central}}$		8.42E-10	7.39E-10	6.36E-10	5.33E-10	4.31E-10	3.2779E-10	2.25E-10
Total second moment of area $2 * I_{xx \text{ Triangular}} + I_{xx \text{ central}}$	7.37E-08	1.407E-07	8.379E-08	4.626E-08	2.308E-08	1.001E-08	3.547E-09	9.402E-10

Figure 97 showing the calculated second moment of area values for double wedge version

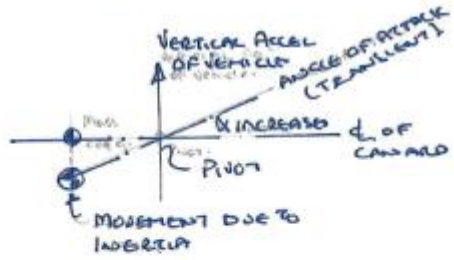
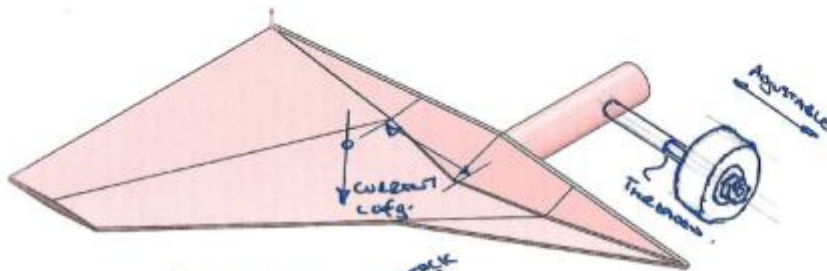
<i>Reference dimensions</i>	Double diamond profile						
local chord base airfoil (m)	0.374	0.328	0.283	0.237	0.191	0.146	0.100
y station (m) taken from 4mm initial offset	0	0.05	0.1	0.15	0.2	0.25	0.3
thickness of central portion (m)	0.003	0.003	0.003	0.003	0.003	0.003	0.003
correction factor	1.39	1.39	1.39	1.4	1.4	1.41	1.47
triangular section max thickness either side of central portion (m)	0.018	0.016	0.014	0.012	0.009	0.007	0.005
second moment of area (I_{xx}) of triangle about centroid (m^4)	6.26E-08	3.72E-08	2.04E-08	1.03E-08	4.38E-09	1.50E-09	3.79E-10
area of triangular portion A (m^2)	3.40E-03	2.62E-03	1.94E-03	1.38E-03	8.97E-04	5.24E-04	2.57E-04
triangular centroid height (m)	6.07E-03	5.32E-03	4.58E-03	3.87E-03	3.13E-03	2.40E-03	1.72E-03
Bending stresses							
$I_{xx \text{ triangular}} = I_{xx} + Ad^2$	1.88E-07	1.12E-07	6.13E-08	3.09E-08	1.31E-08	4.51E-09	1.14E-09
central portion second moment of area $I_{xx \text{ central}}$	8.415E-10	7.38758E-10	6.36E-10	5.33E-10	4.31E-10	3.28E-10	2.25E-10
Total second moment of area $2 * I_{xx \text{ Triangular}} + I_{xx \text{ central}}$	3.763E-07	2.238E-07	1.232E-07	6.241E-08	2.672E-08	9.351E-09	2.497E-09
Target second moment of area	3.74E-07	2.23E-07	1.23E-07	6.14E-08	2.66E-08	9.43E-09	2.50E-09
sectional thickness percentage	10.53%	10.64%	10.79%	11.07%	11.37%	11.93%	13.29%

Figure 98 showing revised sectional thickness requirements for double diamond version to avoid flutter

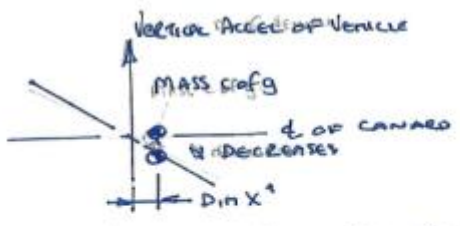
static pressure P_s	101325 Pa		center 1/2 plan form area $A_{1/2}$	0.07 m ²	Y		1.4	mass of 1/2 center without trunnion CAD derived		2.82 kg	distance from trunnion pivot to CoR (non counterbalance) m CAD derived	0.096	
Mach No.	0.1	0.2	0.3	0.4	0.5	0.6	0.7	0.8	0.9	1	1.1	1.2	1.3 notes
q	709	2837	6383	11348	17732	25534	34754	45394	57451	70928	85822	102136	119867 0.51 P ₀ M ²
CL/α from ESDU	3.4438	3.4438	3.4438	3.4438	3.4438	3.4438	3.4438	3.5466	3.5466	3.8036	3.8036	3.8036	3.8036 indicate ESDU derived figure the rest are approx.
T _m centre of pressure from trunnion pivot (m)	0.080	0.080	0.080	0.080	0.080	0.080	0.080	0.080	0.080	0.120	0.120	0.120	0.120 indicate ESDU derived figure the rest are approx.
restoring torsional moment Lift x CoP location (Nm/rad)	13.63	54.51	122.66	218.06	340.72	490.63	667.80	898.27	1136.87	2272.55	2749.79	3272.47	3840.61 A _{1/2} * q * CL / α * T _m
vertical spring constant based on mass without counterbalance	7.03E-03	1.76E-03	7.81E-04	4.39E-04	2.81E-04	1.95E-04	1.43E-04	1.07E-04	8.43E-05	4.22E-05	3.48E-05	2.93E-05	2.49E-05 twist for 1 N load based on 96 mm arm length
vertical component (m)	6.74E-04	1.68E-04	7.48E-05	4.21E-05	2.69E-05	1.87E-05	1.37E-05	1.02E-05	8.07E-06	4.04E-06	3.34E-06	2.81E-06	2.39E-06
k vertical spring rate N/m	1.48E+03	5.94E+03	1.34E+04	2.38E+04	3.71E+04	5.34E+04	7.27E+04	9.79E+04	1.24E+05	2.48E+05	3.00E+05	3.56E+05	4.18E+05
f _n = 1/(2π) * √(k/m) (hz)	3.65	7.30	10.96	14.61	18.26	21.91	25.56	29.65	33.35	47.16	51.87	56.59	61.30
frequency of wheel (hz)	12.06	24.12	36.18	48.24	60.30	72.36	84.42	96.48	108.54	120.60	132.66	144.72	156.79 target 127*1.15 =146hz
check ratio of resonance frequencies for hot spots	3.30	3.30	3.30	3.30	3.30	3.30	3.30	3.25	3.25	2.56	2.56	2.56	2.56 harmonics likely at 2
mass of counterbalance (kg)	1.47	counterbalance moment arm from pivot centreline (m)	0.183	new total mass (kg)	4.29	new CoR position from trunnion pivot	0.000	remember counterbalance is in front of pivot					
new k vertical spring rate N/m	6.03E+05	2.41E+06	5.43E+06	9.65E+06	1.51E+07	2.17E+07	2.96E+07	3.98E+07	5.03E+07	1.01E+08	1.22E+08	1.45E+08	1.70E+08
New natural frequency f _n = 1/(2π) * √(k/m) (hz)	59.68	119.36	179.04	238.72	298.40	358.08	417.76	484.51	545.08	770.65	847.72	924.78	1001.85
check ratio of resonance frequencies for hot spots	0.20	0.20	0.20	0.20	0.20	0.20	0.20	0.20	0.20	0.16	0.16	0.16	0.16 1.47kg @183 mm is a sweet spot!

Figure 99 summarising the initial counterbalance sizing calculations

Dim X. WANTS TO REJUST BRITING
 TO PUSH TRANSLATIONAL RESONANCE FREQUENCY
 HIGH ENOUGH TO BE OUT OF WHEEL EXCITATION
 FREQUENCY CIRCA. 127 Hz @ M1-B.



"AS IS" WITHOUT COUNTERWEIGHT
 NOSE LIPS. TRANSLAT A of A INCREASES
 NOT = DESIRABLE

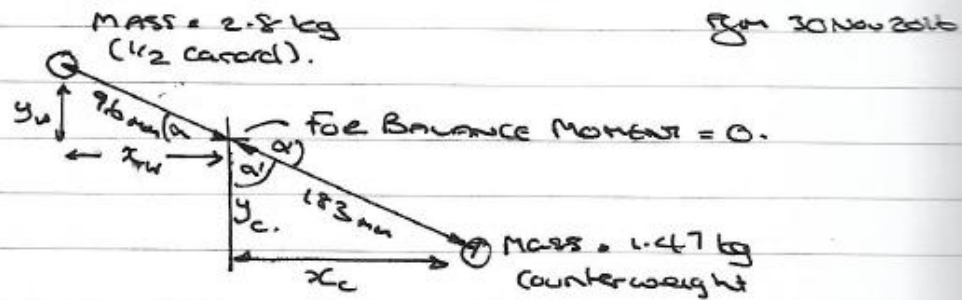


"SHOULD BE" WITH COUNTERWEIGHT
 NOSE LIPS A of A NEUTRALIZED (DECREASE)
 DESIRABLE

BT 26 NOV 2014

Figure 100 showing the counterbalance concept

SAFETY CHECK ON COUNTERBALANCE EFFECT DURING RUN & EXPECTED 'g' LOADS.



EQUATING MOMENTS. $\sum a_c w_m = c_w m$

$$2.8 \times g \times 96 = 1.47 \times g \times 183 \quad (10 \text{ mm})$$

$$= 268.8g = 269g. \quad \text{essentially } 0!$$

FOR ACCEL & DECEL. AT ANY g. HORIZONTAL

FOR NO CHANGE MOMENTS SHOULD EQUATE & SUM = 0.

$$2.8 \times g \times 96 \sin \alpha = 1.47g \times 183 \sin \alpha. \quad \text{Cancelling Common terms}$$

$$2.8 \times 96 = 1.47 \times 183$$

$$269 = 269. \quad \text{ie. equate.}$$

FOR BUMP & REBOUND. VERTICAL ACCELERATION.

\sum Moments UP = \sum Moments down

$$\Rightarrow 2.8 \times g \times 96 \cos \alpha = 1.47g \times 183 \cos \alpha.$$

cancelling common terms.

$$2.8 \times 96 = 1.47 \times 183$$

$$269 = 269. \quad \text{ie. equate}$$

CONCLUSION. WHEN MASS BALANCE IS POSITIONED STATICALLY SO IT BALANCES THE CANARD HORIZONTALLY

ANY ACCELERATION IN ANY DIRECTION IE

bump, rebound, accel or decel will not change the angle of attack

A PERFECT BALANCE IS IDEAL THOUGH DAMPENING WILL HELP WITH TRANSIENTS.

Figure 101 showing calculations to check sensitivity to lateral and vertical g-forces

SENSITIVITY CHECK.

MAKE THE COUNTERBALANCE LEVER 163mm INSTEAD OF 183mm. Now moments don't equate.

DIFFERENCE IN MOMENTS

$$2.86g \times 96 \neq 1.47g \times 163 \quad (\text{Nmm})$$

$$268.8 = 239.6 + C.$$

the correcting constant C must be made up by the moment created by the wing lift about the centre of pressure relative to the trunnion of. This varies with MACH No.

For say MOA. The sums are as follows.

"MACH 0.9 chosen as this is MAX decel due to full flap deployment & estimated α 3.87g (max). Actually its m1.0 but that is a singularity and very difficult to compute.

$$\alpha \text{ MO.9 lift curve slope/degree} = 0.062 \left(\frac{C_L}{\alpha} \right).$$

Centre of Pressure About trunnion of α MO.9 = 80mm.

$$\text{So } C = 268.8 - 239.6 = 29.2/g \text{ Nmm}$$

$$\text{and } \alpha \text{ } 3.87g = 29.2 \times 3.87 = 113 \text{ Nmm.}$$

$$\text{So } 113 = 0.062 \times 0.07 \times 57451 \times 80 \times \alpha$$

\uparrow area of control $\frac{1}{2}$ \uparrow dynamic pressure

$$113 = 19947 \alpha \quad \therefore \alpha < 1^\circ.$$

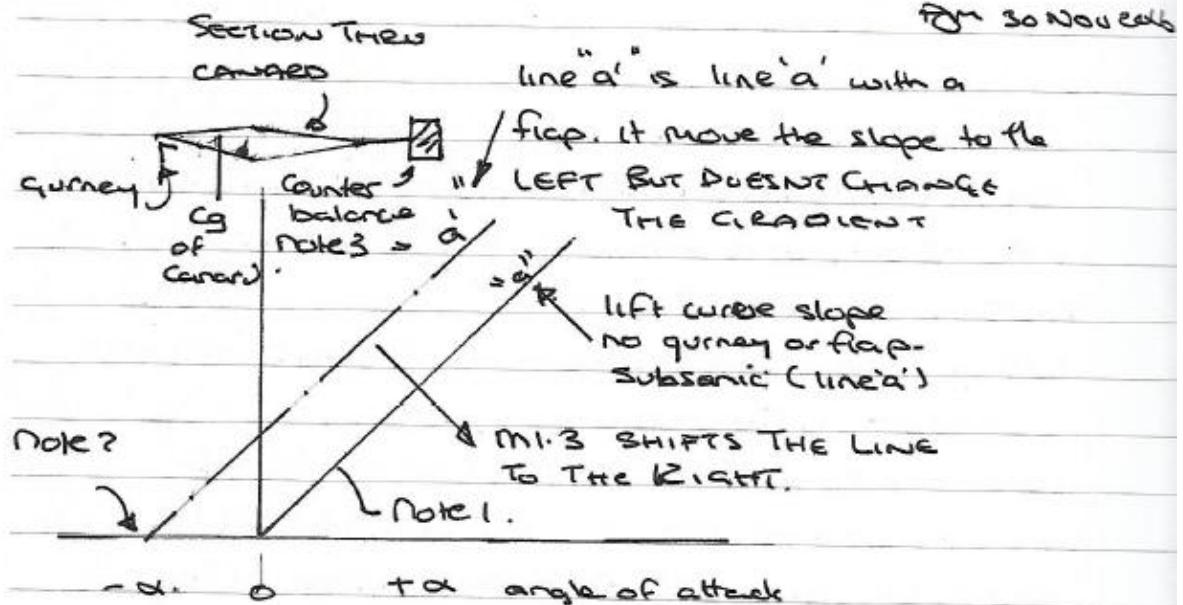
$$\text{At } \alpha \text{ MO.7. decel} = 1.04g \quad \frac{C_L}{\alpha} = 0.06/\text{deg.}$$

$$q = 34745 \quad \text{thus } \alpha = < 1^\circ.$$

It doesn't appear to be too sensitive.

Figure 102 showing the calculations to check sensitivity to lateral and vertical g-forces cont.

How The GURNEY & COUNTERBALANCE WORKS



Notes.

1. THE SLOPE OR RATE OF CHANGE OF LIFT WITH ANGLE ($\frac{C_L}{\alpha}$) DETERMINES THE FORCE (WHEN \times WITH AREA & q) & the distance of centre of pressure from trailing \times Lift = restoring couple.
- 2 THE GURNEY HEIGHT determines or sets THE RUNNING ANGLE OF ATTACK.
- 3 THE COUNTERBALANCE SETS STATIC POSITION OF CANARD. INCREASES SYSTEM natural frequency & negates longitudinal & vertical g forces.

Figure 103 showing how the canard with Gurney & counterbalance work

Excitation directly by the canard due to the aerodynamic induced characteristics.

A sanity check was carried out about excitation frequencies induced as a result of;

- The creation of leading edge vortices as a result mainly of the delta configuration
- The creation of Von-Karman-like shedding vortices due to the Gurney flap acting as a plate normal to airflow.

Two empirical formulas were used for estimation of the leading edge induced vortices as shown in Figure 104. The only difference being the constant used. As it is a function of the local Reynolds number, sections were studied at the root chord, the point at which the LERX intersects with the main lifting surface leading edge, the Mean aerodynamic chord (MAC) and the tip chord. The results suggest that the frequencies are too high to excite the structure or create a “lock-in” situation.

“Lock-in” occurs when the frequency of excitation equals the natural frequency of the structure.

The gurney flap used a model based on a flat plate normal to the airflow, values for the Strouhal number are well documented and the value chosen was 0.115. The frequency is a function of the local velocity, Strouhal number and the inverse of the square root of the gurney flap area. Three Gurney flap heights were chosen, 2, 4 and 6%; the results suggest that shedding frequencies will also be too high to excite the structure (Figure 106).

DELTA LEADING EDGE VORTEX FREQUENCIES									
	Reynolds number	68459	*Vx		speed of sound	341	m/s		
	Mach No.	0.6	0.7	0.8	0.9	1	1.1	1.2	1.3
	local chord (m)	Re							
ROOT	0.474	6.64E+06	7.75E+06	8.85E+06	9.96E+06	1.11E+07	1.22E+07	1.33E+07	1.44E+07
LERX	0.32	4.48E+06	5.23E+06	5.98E+06	6.72E+06	7.47E+06	8.22E+06	8.96E+06	9.71E+06
MAC	0.246	3.45E+06	4.02E+06	4.59E+06	5.17E+06	5.74E+06	6.32E+06	6.89E+06	7.47E+06
TIP	0.1	1.40E+06	1.63E+06	1.87E+06	2.10E+06	2.33E+06	2.57E+06	2.80E+06	3.03E+06
Gad-El-Hak empircally derived Stroudhal numbers									
ROOT		0.63	0.58	0.55	0.51	0.49	0.47	0.45	0.43
LERX	$St = \frac{1625}{\sqrt{Re}}$	0.77	0.71	0.66	0.63	0.59	0.57	0.54	0.52
MAC		0.88	0.81	0.76	0.71	0.68	0.65	0.62	0.59
TIP		1.37	1.27	1.19	1.12	1.06	1.01	0.97	0.93
Gad-El-Hak empircally derived frequency (Hz)									
ROOT		272	294	314	333	351	369	385	401
LERX	$St = fL / U_{\infty}$	491	530	567	601	634	664	694	722
MAC		728	786	841	892	940	986	1030	1072
TIP		2809	3034	3244	3441	3627	3804	3973	4135
Lowson empircally derived Stroudhal Numbers									
ROOT		1.00	0.93	0.87	0.82	0.77	0.74	0.71	0.68
LERX	$St = \frac{2577}{\sqrt{Re}}$	1.22	1.13	1.05	0.99	0.94	0.90	0.86	0.83
MAC		1.39	1.29	1.20	1.13	1.08	1.03	0.98	0.94
TIP		2.18	2.02	1.89	1.78	1.69	1.61	1.54	1.48
Lowson empircally derived frequency (Hz)									
ROOT		432	466	498	529	557	585	611	635
LERX	$St = fL / U_{\infty}$	778	841	899	953	1005	1054	1101	1146
MAC		1155	1247	1333	1414	1491	1563	1633	1700
TIP		4455	4812	5144	5456	5751	6032	6300	6558

Figure 104 showing a summary of frequencies vs. Mach No. Due to Leading edge vortex generation

GURNEY FLAP INDUCED VORTEX FREQUENCIES									
						speed of sound	341	m/s	
	Mach No. (U_∞)	0.6	0.7	0.8	0.9	1	1.1	1.2	1.3
	Velocity (m/s)	205	239	273	307	341	375	409	443
	local chord (m)								
MAC (m)	0.246	Gurney cross sectional area. A (m^2)	panel span (m)	0.30	Strouhal No. flat plate normal to flow	0.115	CD	1.17	
Gurney percentage	2.00%	1.48E-03							
	4.00%	2.95E-03							
	6.00%	4.43E-03							
Frequency = $ST \cdot U_\infty / \sqrt{A}$	2.00%	612	715	817	919	1021	1123	1225	1327
Frequency = $ST \cdot U_\infty / \sqrt{A}$	4.00%	433	505	577	650	722	794	866	938
Frequency = $ST \cdot U_\infty / \sqrt{A}$	6.00%	354	413	471	530	589	648	707	766

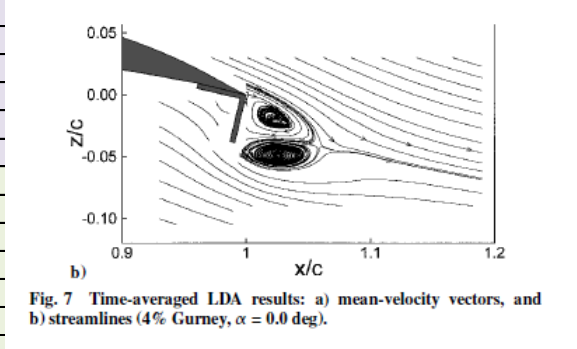


Figure 105 showing estimated Gurney flap induced frequencies

Converging onto a final solution

In this solution the airfoil section is elliptical. It reinforces the trunnion area using an ogive form. The resulting improvement in the second and polar moments of area compared to the double wedge solution allows for a thinner section. Currently, this is 6%. The mass excluding the trunnion shaft is at 2885g which means the natural frequencies will be similar. However, the overall system resonance frequencies will depend upon the length of the trunnion shaft; its torsional stiffness and the distance from the counterbalance to the wing root. Essentially, the longer this distance, the greater the torque wind up, angular displacement and lower the natural frequency.

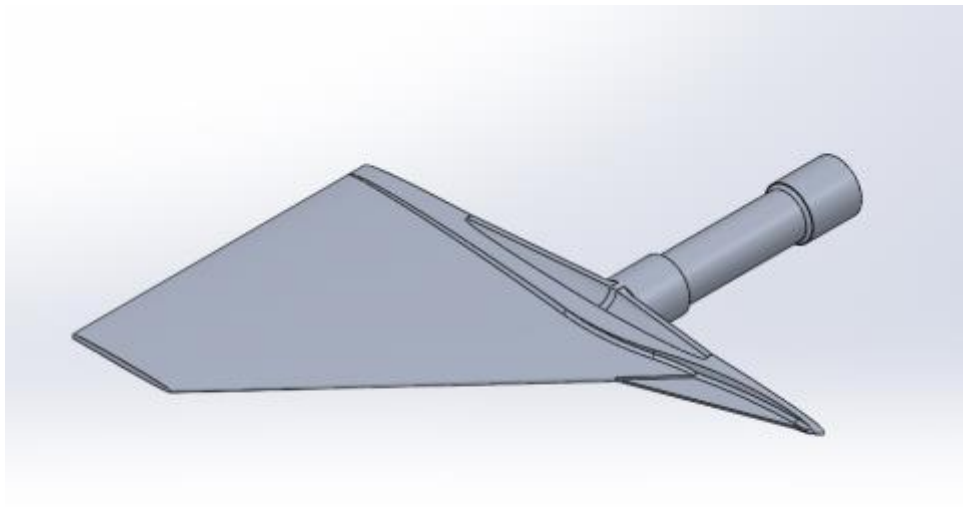


Figure 106 showing V7.3

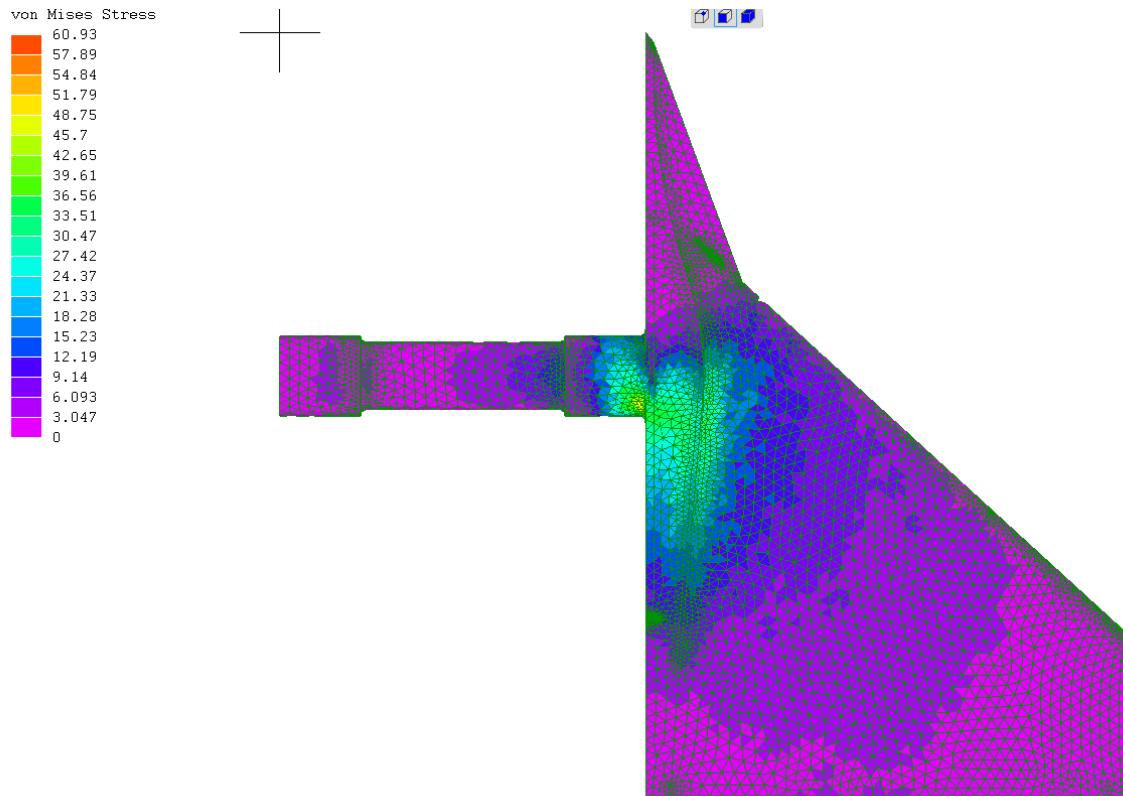


Figure 107 showing Von Mises stresses for v7.3

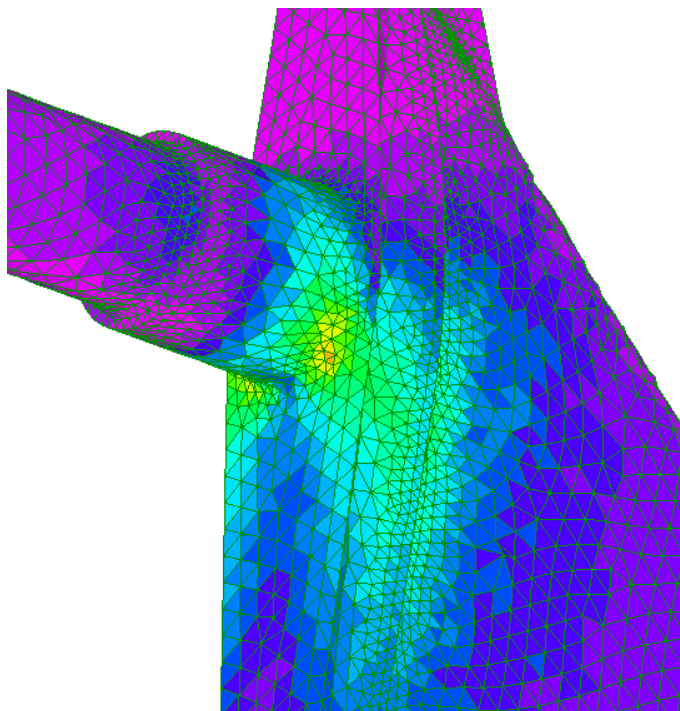


Figure 108 showing local enlargement around trunnion interface V7.3

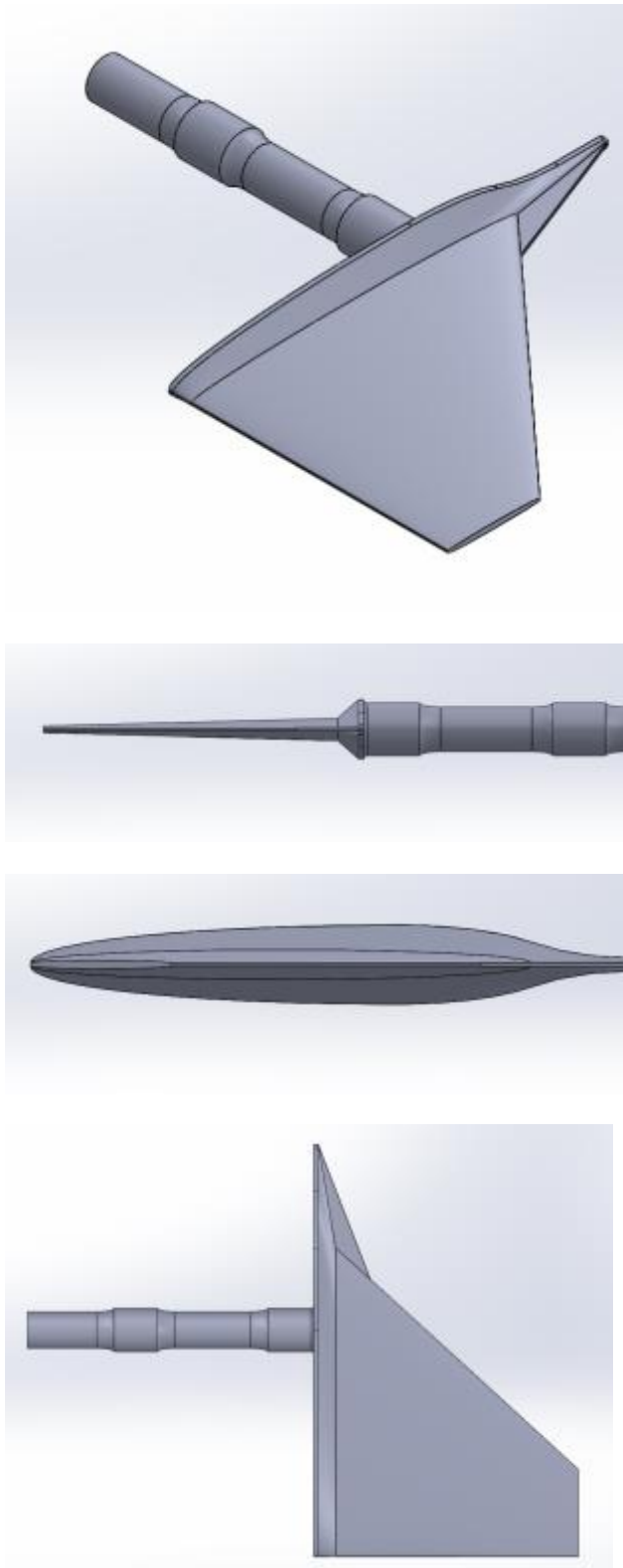


Figure 109 showing various orthographic views of V 7.5

Displacement Magnitude

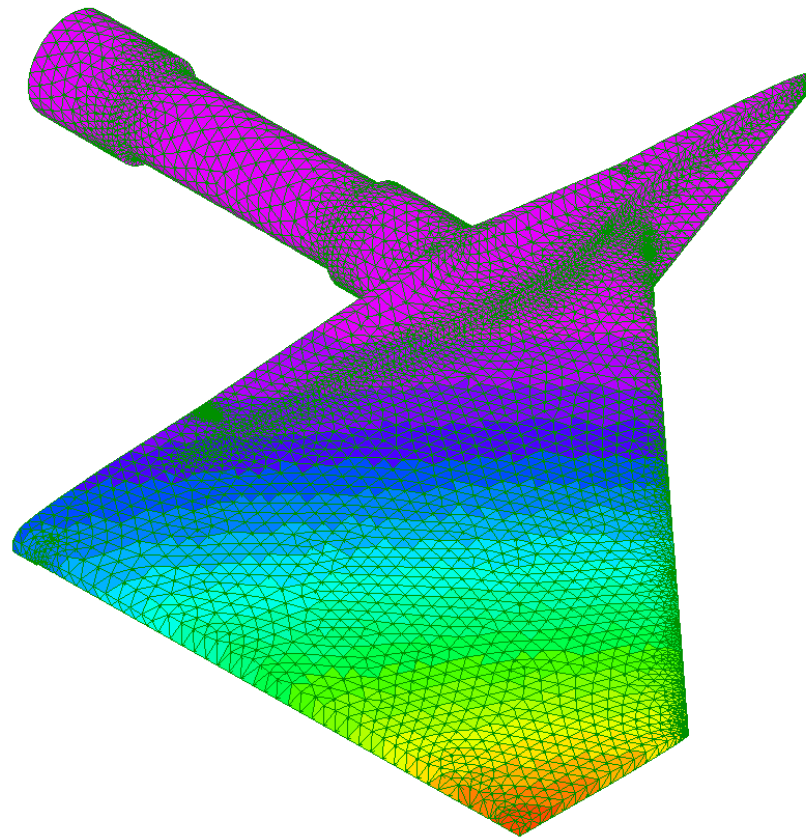
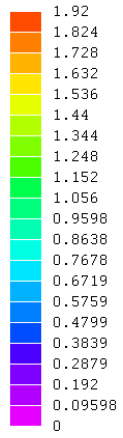


Figure 110 showing maximum displacement @ <2 mm for V 7.5

von Mises Stress

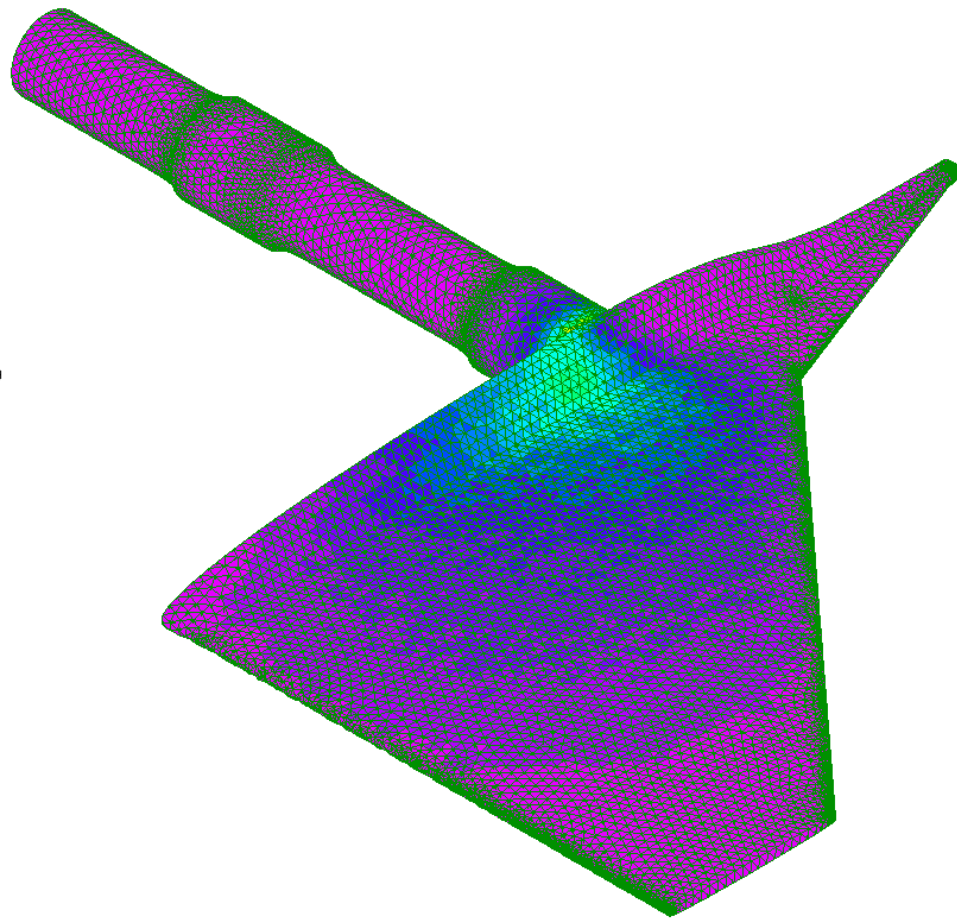
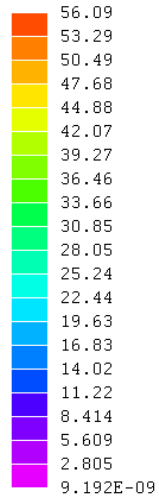


Figure 111 showing Von Mises stresses V7.5

von Mises Stress

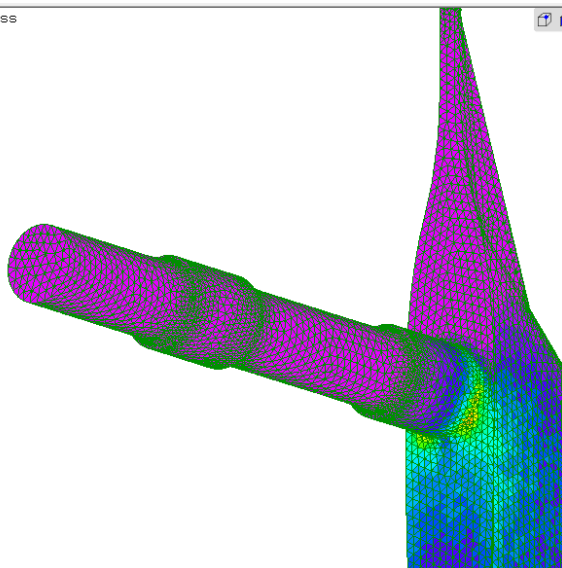
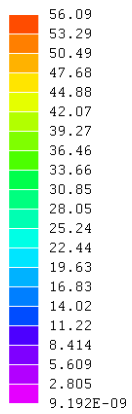


Figure 112 showing localised view of trunnion von Mises stresses V 7.5

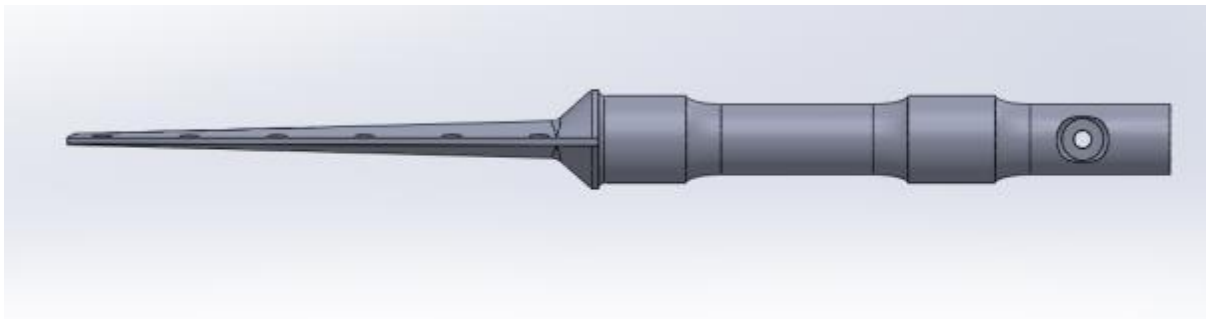
Version 8.2

I thought it was starting to get very industrial looking so revisited it all again in the version 8 series. The main changes were that instead of an ogive shaped root I went for the elliptical/bi-convex form. As it turned out, there were potentially some model frequencies that excited the area around the LERX, and as such this stiffened them up. The total mass excluding the trunnion is 2.98 kg. That also doesn't include the bolts and Gurneys. The airfoil section is now an ellipse for the front 50% and bi-convex curve for the rear.

The orthographic views for V 8.2 shown in Figure 113 and Figure 114 and the isometric Figure 115.

The maximum displacement is 1.71 mm at the tip with the 1999 N loading applied as pressure. This the spring constant is 1.169×10^6 N/m yielding a natural frequency of 99 Hz

Realistically, those frequencies above those generated by the suspension are transient. At 1000 mph the measured mile is achieved in 3.6 seconds, so it is highly unlikely that any excitation will lead to failure simply because there isn't sufficient time to overcome the effects of inertia. At the sub 10 Hz, there are some pitch induced frequencies which could excite the canard angularly. Those modes are shown in Figure 120 with the displacement being concentrated around the LERX. These are small displacements, and the frequency is tempered by the polymer doughnut dampener attached to the front suspension, making any excitation frequencies in fact transient.



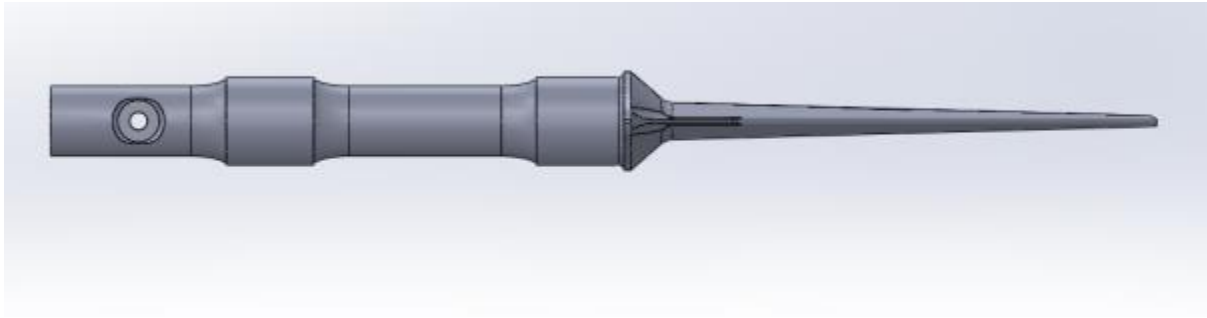


Figure 113 showing various orthogonal views of V 8.2

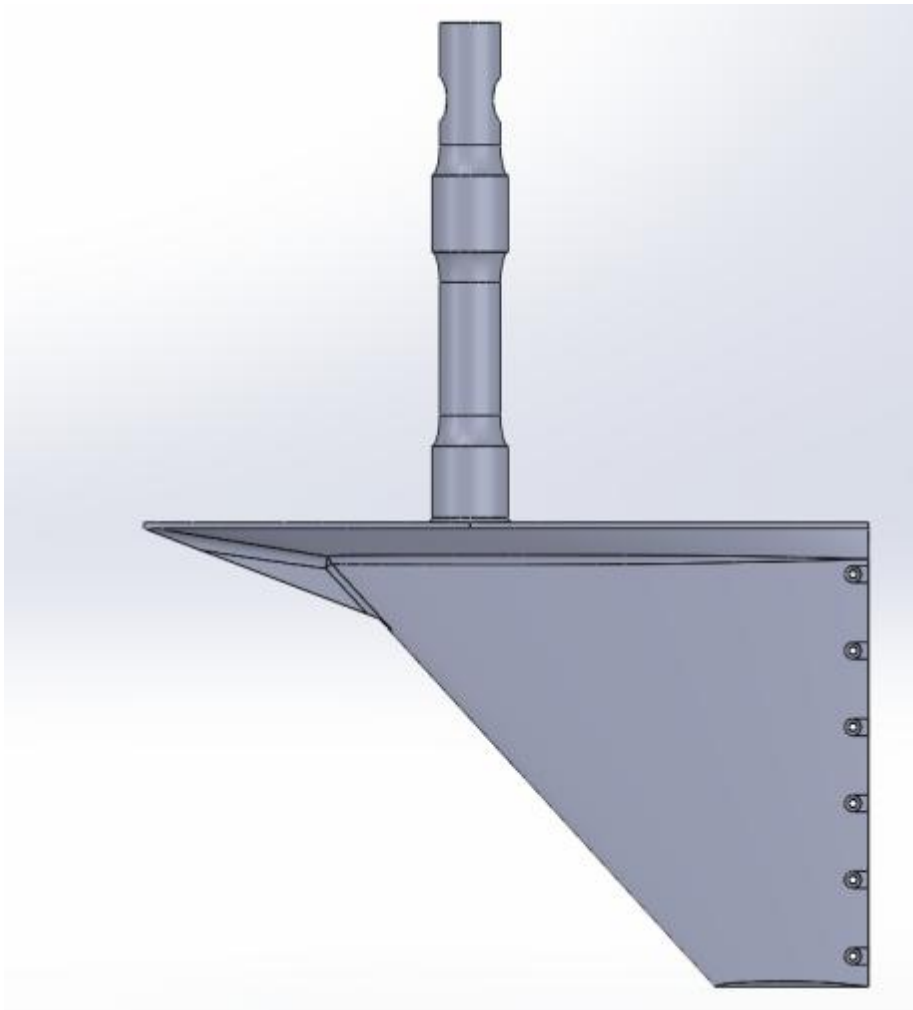


Figure 114 plan view V 8.2

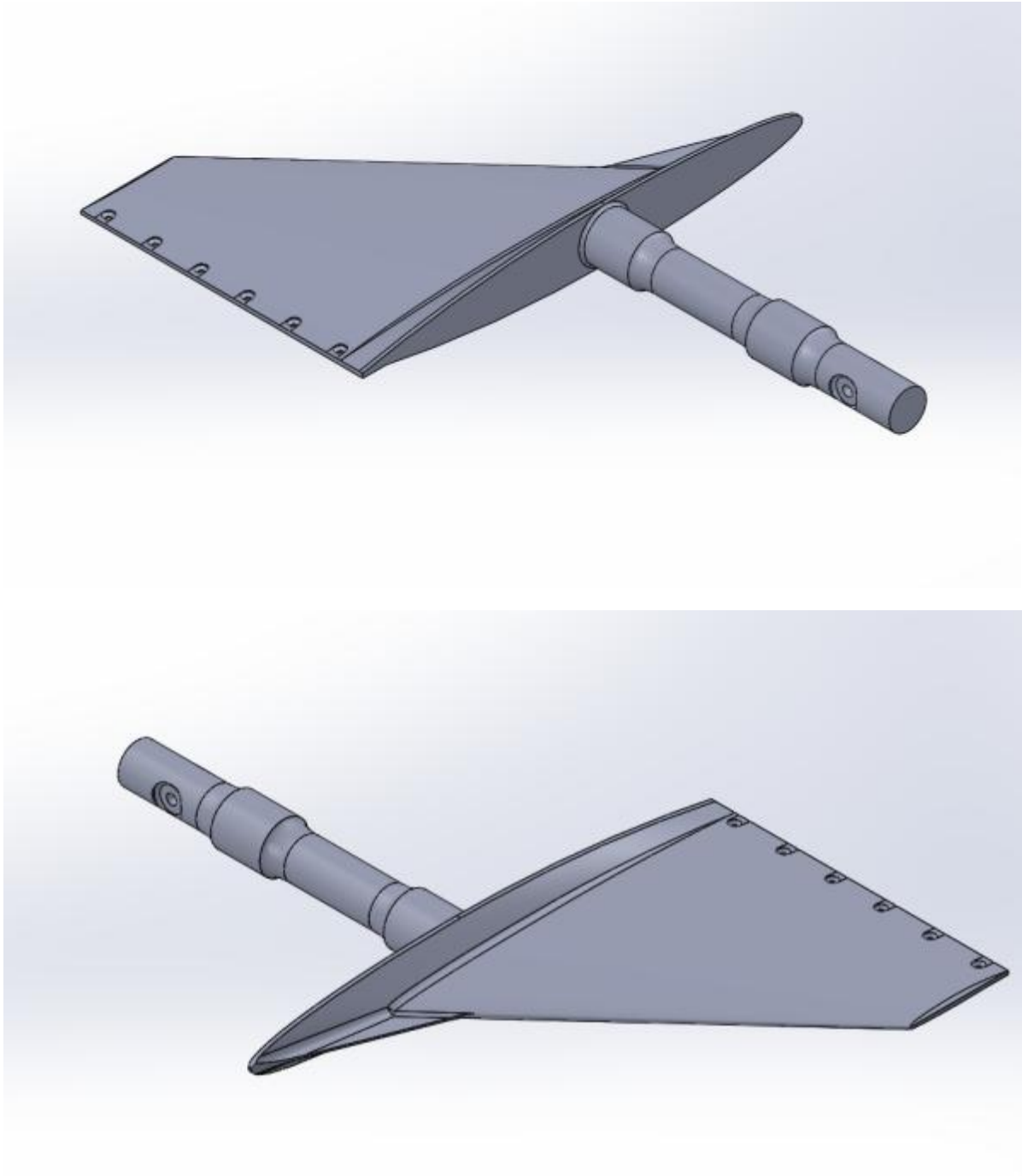


Figure 115 isometric views of V8.2

Displacement Magnitude

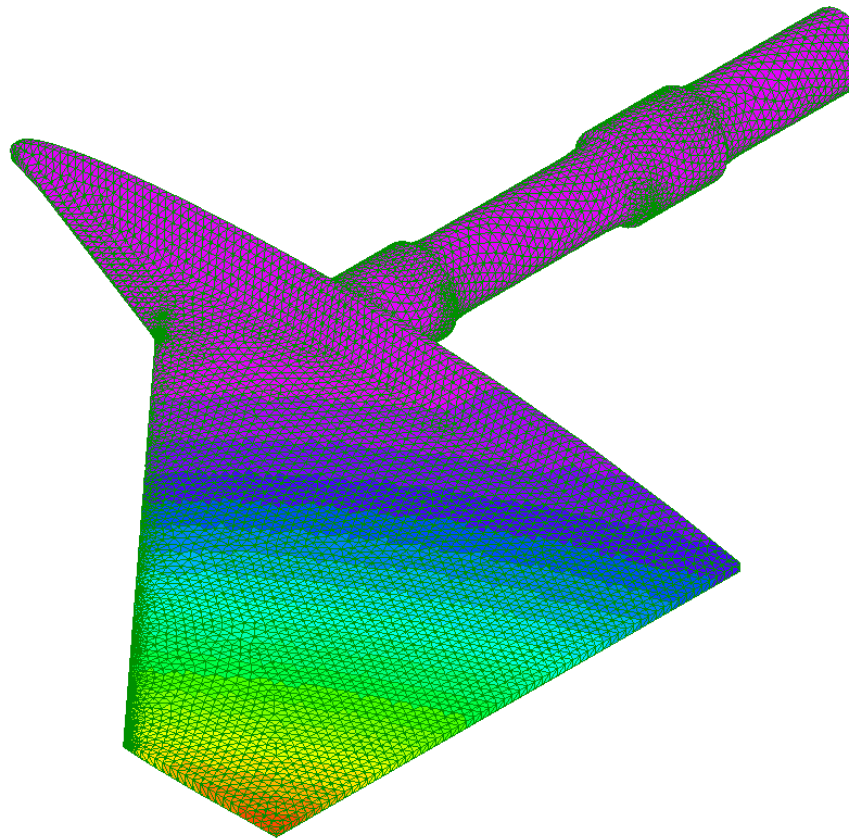
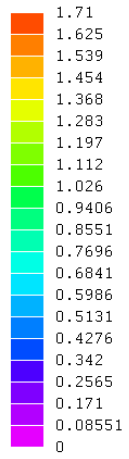


Figure 116 showing maximum displacement V 8.2

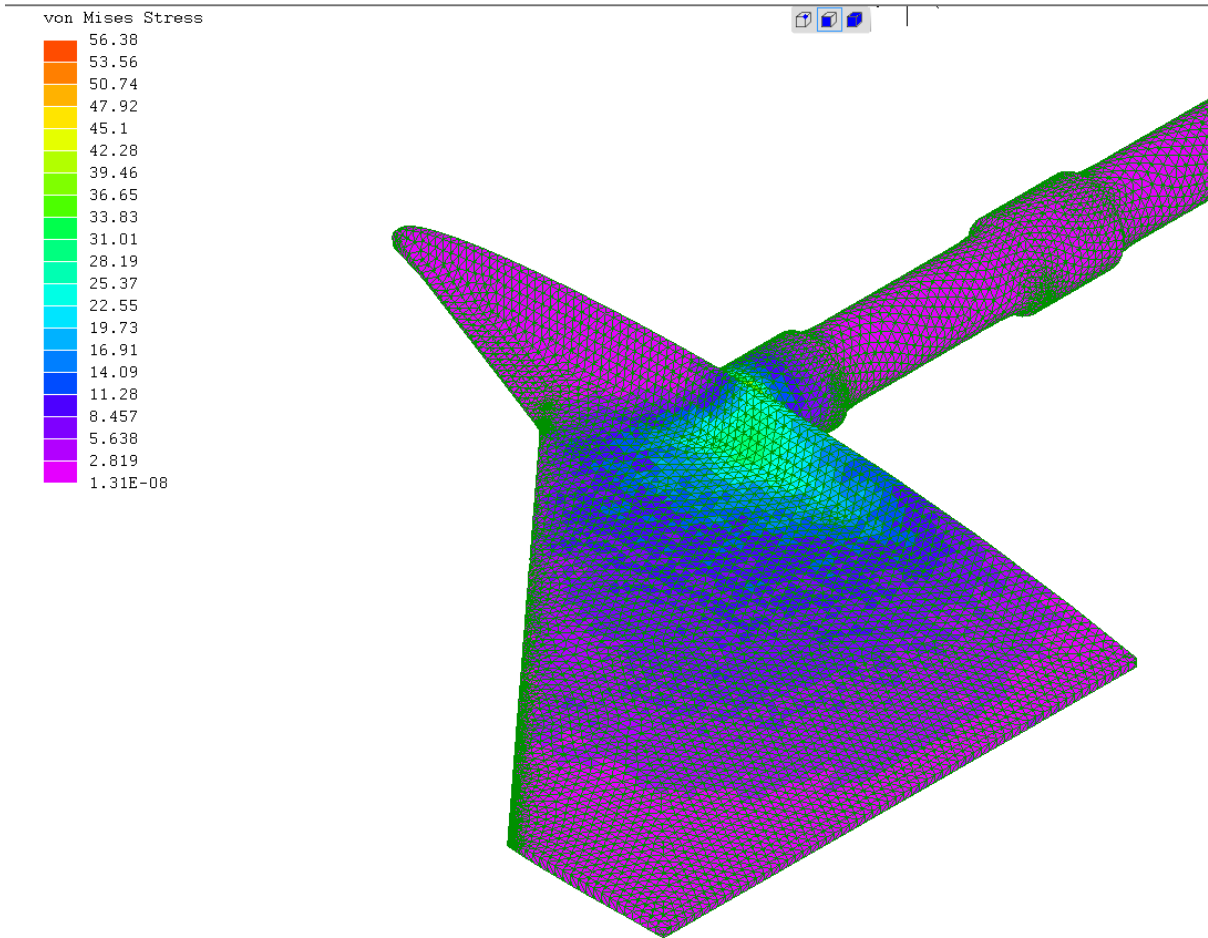


Figure 117 Von Mises stresses V 8.2

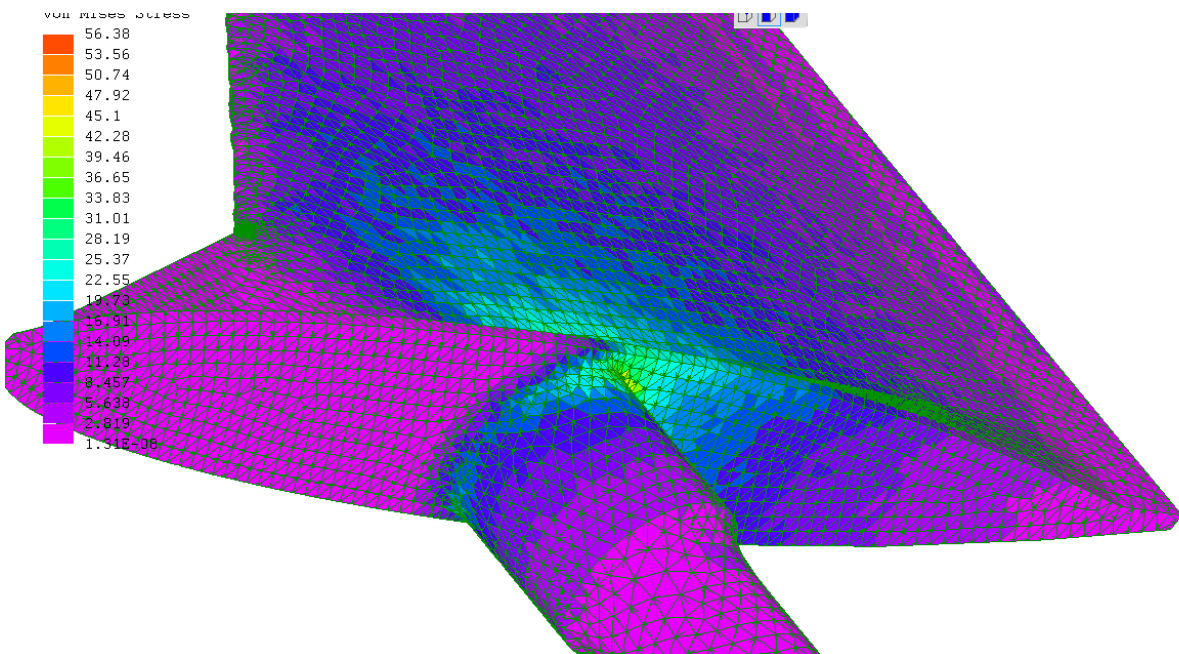


Figure 118 localised trunnion Von Mises stress v 8.2

von Mises Stress

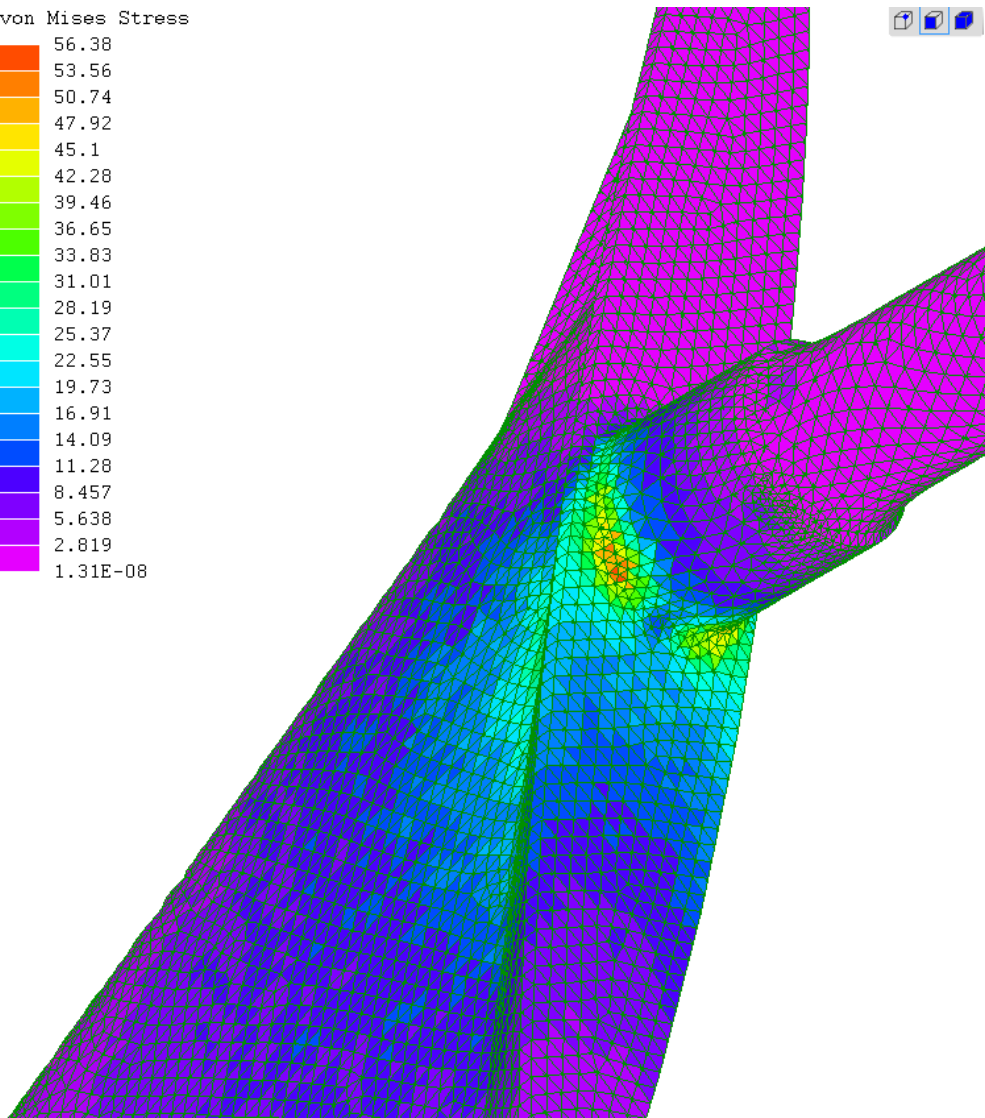
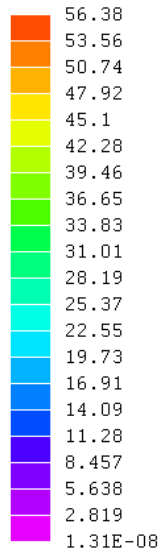


Figure 119 localised trunnion Von Mises stress v 8.2

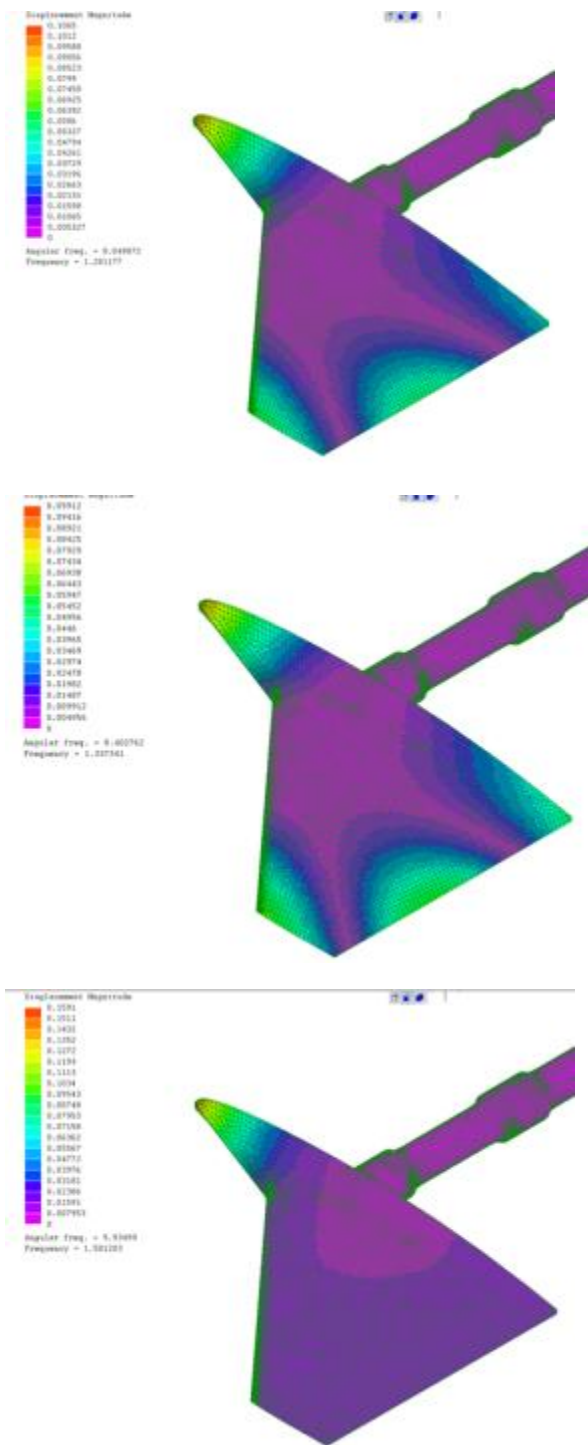


Figure 120 showing angular resonance frequencies falling within the 6.96 t 9.83 Hz range

Appendix A

This section is an extract from a study that models the aero- performance of the vehicle. An abridged version is included in this report for completeness because the results determine the maximum loads seen by the canard. The complete study aims to create some aerodynamic empirical models of the AI5R. It initially studies the Blue Flame and then compares the results against the wind tunnel results of Tom Morel's MSc study. Once the experimental and empirical methods correlate, this is then applied to the Aussie Invader 5R vehicle.

Base Drag and Airbrake effect on Canard requirements

There is a change in the front/rear wheel weight distribution is as a result of the increase in base drag during deceleration. That base drag increase is as a result of the change in airflow at the rear because the loss of energy introduced into the flow as a result of the engine exhaust. Once the engine shuts off, the energy is injected into the air at the rear of the vehicle is lost, and the flow becomes unstable.

The other factor is the airbrakes; They are designed to significantly increase the base area and cause further separation and drag at the rear of the vehicle. The high location of the airbrakes when deployed introduces a moment counteract that moment the canard needs to be deflected downwards (i.e. a negative AofA). The degree of deflection with being significant but well within the working range of the canard due to its low aspect ratio. This study determines what angle the canard needs to be deployed at to mitigate the unfavourable moments.

Because of similarities in the configuration, the CFD study by Wang was reviewed. There was a significant disparity between this thesis and the original Morel especially when it came to lift predictions. Some of this may be attributed to the dimensional differences between Morel's wind tunnel model and the final version of the Blue Flame. However, the drag figures showed good correlations, and it is assumed that they are insensitive to the differences in the two models used.

By investigating the results, identifying the drag engine on and off values and then using the same assumption about rolling resistance C_D values for base drag at a range of Mach numbers were determined. Note that Wang's results at $M 0.7$ seems somewhat spurious. The moments expected during engine off; airbrake deployment, etc. (Figure 123.)

The base drag is significantly affected by the base area which is measured at the rear of the vehicle. In this analysis, the cross section the boat tail design of the Blue Flame was specifically designed to

minimise this and drag as a whole. The value of the area (Blue flame 0.37m^2 see Figure 121) is significantly smaller than AI5R (1.029m^2 see Figure 125 and Figure 126), so one would expect deceleration figures to be considerably higher. The deployment of the airbrakes adds directly to this base area.

The moments assumed for the AI5R may be found in Figure 122.

Empirical formulae for the estimation of base drag values for rockets out of ground effect is shown Figure 124, and the results are similar which suggests the assumptions are reasonable. The total drag is summarised in Figure 127. As part of the investigation, a check was made to ensure that the Reynolds number for the airbrakes were sufficiently high enough. The biggest factor on drag created by the airbrake is the deployment speed And angle.

The assumed airbrake deployment angles are shown in Figure 128. Essentially the full deflection of 60 degrees doesn't occur until the vehicle is subsonic circa $M0.9$. The total drag based on that deployment angle profile is shown in Figure 129.

The drag induced moment calculations are shown in Figure 130. The lift coefficient for the proposed canard is shown in Figure 131. And the necessary wing parameters to offset the moments induced in Figure 132. This defines the canard angle at around minus 8 degrees.

The peak values are slightly less than the first cut estimation derived some time ago when the airbrakes were initially designed. The aim was not to exceed a value of 4g deceleration(Figure 133, Figure 134 and Figure 135). Pragmatically the time to deploy has a finite value, and from $M1.3$ it is estimated that following the deployment angle profile would only give the mechanism approximately 3 seconds to go from zero to 60 degrees. Parenthetically, Bloodhound SSC airbrake system deploys to 60 degrees in 4 seconds and the maximum with retardation peaking at around 3.7g.

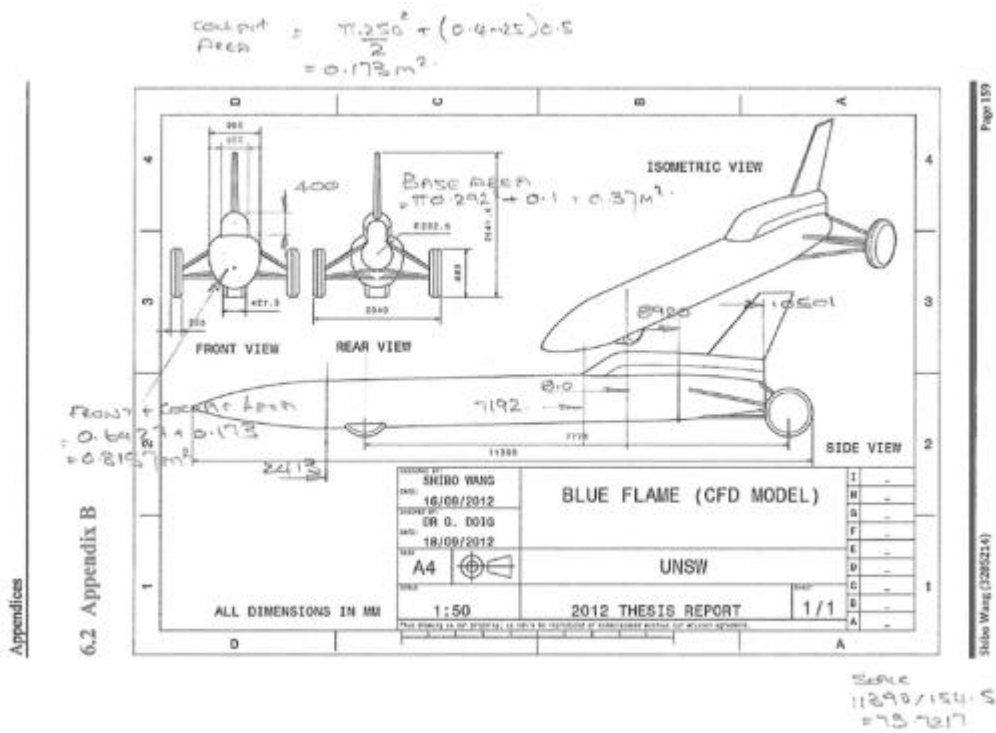


Figure 121. Showing base area of Blue Flame

Blue Flame			mass (lb)	6000	mass (kg)	2722	
Mach number a	0.6	0.7	0.8	0.9	1	1.1	1.2
dynamic pressure $q = 0.5 \gamma \rho a^2$	25534	34754	45394	57451	70928	85822	102136
Tip cone area (m ²)	0.65	reference	6.96ft ³				
Drag rocket on (kN)	9.86	15.3	21.96	34.05	51.185	72.69	94.55
Calculated rolling resistance(kN)	2.12	2.83	3.64	4.56	5.6	6.72	7.97
Drag without rolling resistance (kN)	7.74	12.47	18.32	29.49	45.585	65.97	86.58
CD based on cone CSA 6.95ft ²	0.47	0.56	0.63	0.79	1.00	1.19	1.31
Drag rocket off (kN)	11.99	16.44	26.32	41.13	62.2	82.97	103.42
Delta rocket off-on (kN)	2.13	1.14	4.36	7.08	11.015	10.28	8.87
Base area (m ²)	0.37						
CD Base drag	0.23	0.09	0.26	0.33	0.42	0.32	0.23

Figure 123 Showing summary of base drag C_D

Base drag is caused by a low-pressure area created at the base of the rocket or in any place where the body radius diminishes rapidly enough. The magnitude of the base drag can be estimated using the empirical formula [18, p. 23]

$$(C_{D*})_{base} = \begin{cases} 0.12 + 0.13M^2, & \text{if } M < 1 \\ 0.25/M, & \text{if } M > 1 \end{cases} \quad (3.94)$$

The base drag is disrupted when a motor exhausts into the area. A full examination of the process would need much more detailed information about

Mach no	0.6	0.7	0.8	0.9	1	1.1	1.2	1.3
CD base subsonic	0.1668	0.1837	0.2032	0.2253	0.25			
CD base supersonic					0.25	0.227273	0.208333	0.192308

Figure 124 Showing simplified rule to quantify base drag

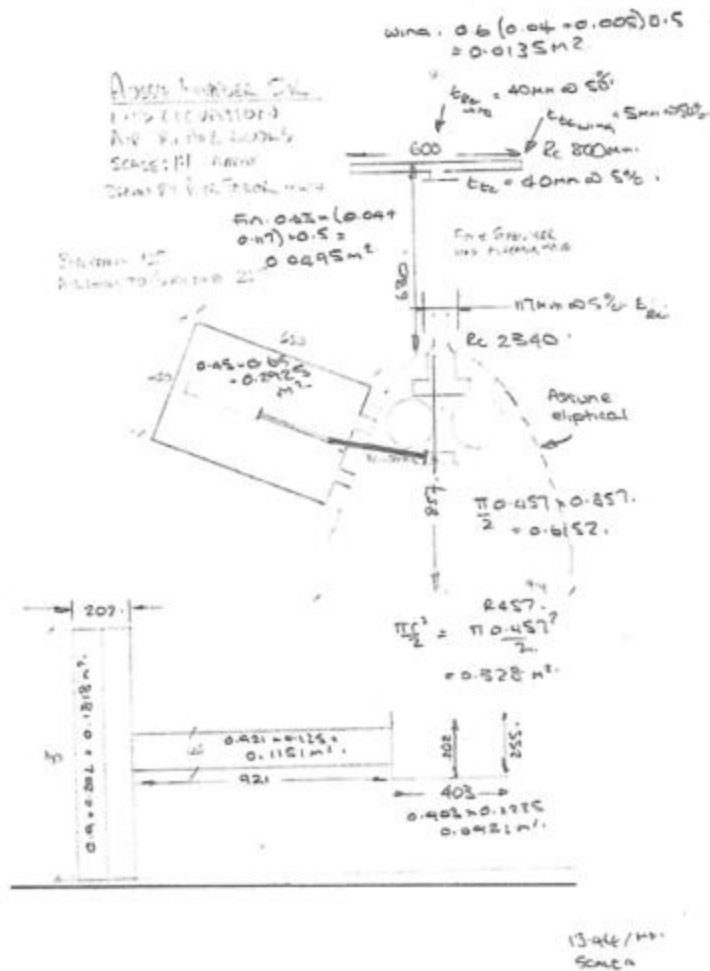


Figure 125 Showing cross section through AI5R at rear

AI5R wave drag area at rear				
region	qty	area (m ²)	Total (m ²)	
wheels	2	0.1818	0.3636	
axle	2	0.115125	0.23025	
axle mount	1	0.086041	0.086041	
lower body half	1	0.328059	0.328059	
upper body half	1	0.615201	0.615201	
tail fin	1	0.049455	0.049455	
tailplane	1	0.0135	0.0135	
Total			1.686106	
base area (m ²)			1.029301	
airbrake	2	0.2925	0.585	used for wave drag calculations
endplate factor	1.68			
airbrake effective area			0.9802	for Cd calculations only

Figure 126 showing rear cross-sectional area of AI5R

Cd reference area (m ²)	0.78							
Mach no	0.6	0.7	0.8	0.9	1	1.1	1.2	1.3
airbrake deployment angle	60	60	60	60	45	30	15	0
wave drag effect area factor	0.87	0.87	0.87	0.87	0.71	0.50	0.26	0.00
wave drag incremental area (m ²)	0.51	0.51	0.51	0.51	0.41	0.29	0.15	0.00
expected wave drag multiplier	0	0	0	1.30	1.25	1.17	1.09	1.00
dynamic pressure q = 0.5γ*Pa2	25534	34754	45394	57451	70928	85822	102136	119867
CD (derived from BF)	0.47	0.56	0.63	0.79	1.00	1.19	1.31	1.31
wave drag increment as a result of airbrake deployment (kN)				10.68	13.49	13.80	9.38	0.00
Cd of airbrake deployed	1.01	1.06	1.16	1.34	1.19	0.78	0.35	0.00
Drag (kN)	25.36	36.00	51.64	75.60	82.60	65.20	34.72	0.00
base drag incremental area (m ²)	0.51	0.51	0.51	0.51	0.41	0.29	0.15	0.00
base drag multiplier	1.49	1.49	1.49	1.49	1.40	1.28	1.15	1.00
base drag Cd	0.23	0.09	0.26	0.33	0.42	0.32	0.23	0.00
incremental base drag (kN)	12.94	17.61	23.00	29.11	29.34	25.11	15.47	0.00
Mach no	0.6	0.7	0.8	0.9	1	1.1	1.2	1.3
total drag increase (kN)	38.30	53.60	74.64	115.39	125.42	104.11	59.57	0.00

compressiblity corrected

Figure 127 Showing a summary of total drag vs. Mach No. for assumed airbrake deployment angle.

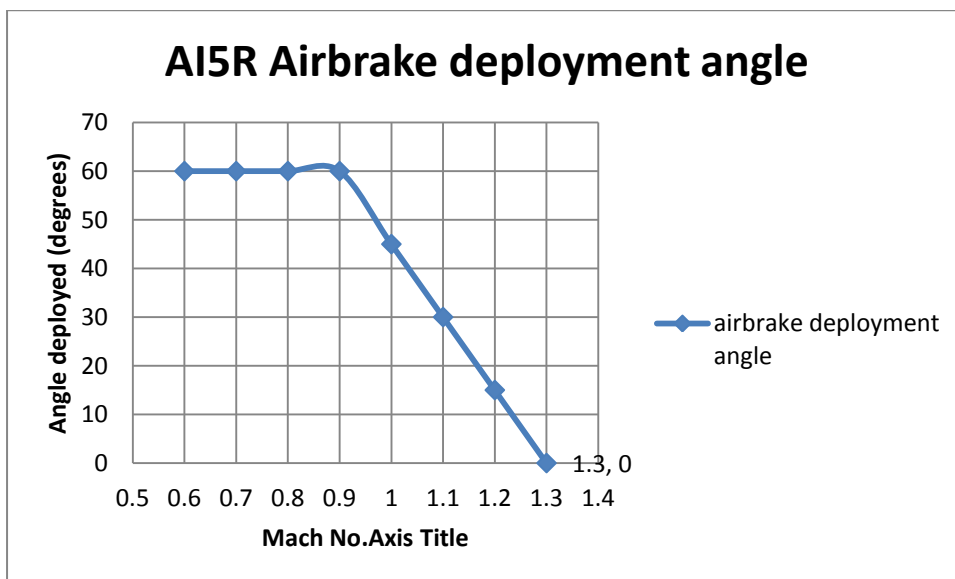


Figure 128 Showing airbrake deployment angle related to Mach No.

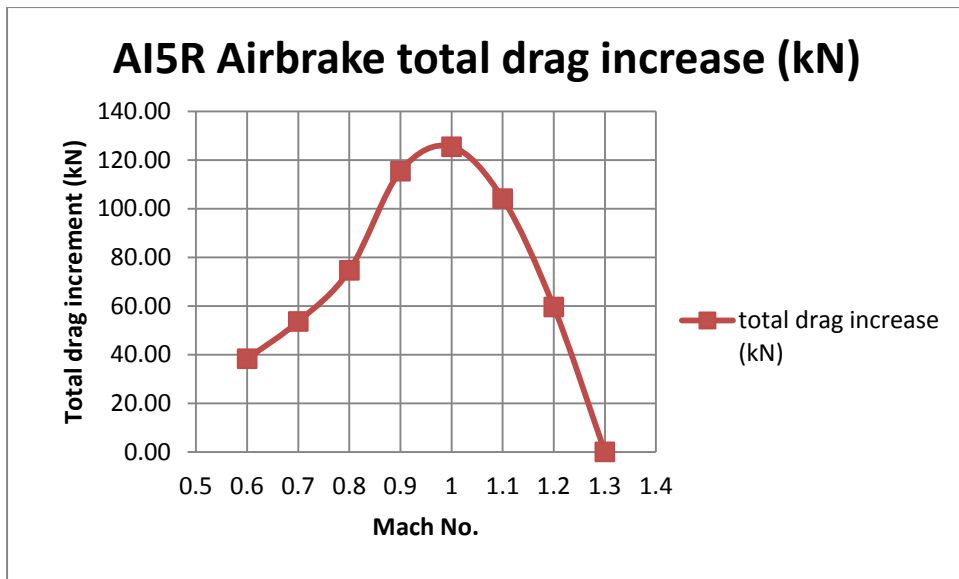


Figure 129 Showing the airbrake induced total vehicle drag

Aussie Invader 5R							
tip cone area . A. (m ²)	0.78		airbrake area total (m ²)	0.585			
Base area (m ²)	1.03		Base drag noment arm (m)	1.1779	assumed centroid of area		
Mach No	0.6	0.7	0.8	0.9	1	1.1	1.2
dynamic pressure q = 0.5Y*Pa ²	25534	34754	45394	57451	70928	85822	102136
CD (derived from BF)	0.47	0.56	0.63	0.79	1.00	1.19	1.31
CD base drag power off (value from BF)	0.23	0.09	0.26	0.33	0.42	0.32	0.23
Aero Drag (inc. wave) (kN) CdqA	9.33	15.04	22.09	35.56	54.96	79.54	104.40
additional drag component airbrake (kN)	0.00	0.00	0.00	10.68	13.49	13.80	9.38
total aero drag (kN)	9.33	15.04	22.09	46.24	68.45	93.34	113.77
Aero drag moment arm from rear wheel ground contact point (m)	1.11	assume 60% centreline and 40% base area centroid		centre of gravity postion (m)	1.008		
aero drag moment (kNm)	10.36	16.69	24.52	51.33	75.98	103.61	126.28
Base drag (kN)	5.93	3.17	12.13	19.70	30.64	28.60	24.68
additional base drag area as a result of airbrake deployment (kN)	12.94	17.61	23.00	29.11	29.34	25.11	15.47
Base drag moment (kNm)	15.24	20.74	27.09	34.29	34.56	29.57	18.22
airbrake force (kN)	25.36	36.00	51.64	75.60	82.60	65.20	34.72
moment arm(m)	1.7	scaled					
airbrake induced moment (kNm)	43	61	88	129	140	111	59
centre of gravity induced moment (kNm)	-58	-78	-117	-171	-211	-214	-197
Total moment induced ACW (kNm)	10	20	22	44	40	30	7
front canard moment arm (m)	10.935						
total downforce required by canard (kN)	0.95	1.87	2.03	3.99	3.70	2.77	0.60

Figure 130 Showing calculations to determine the necessary moments required from the canard vs Mach No.

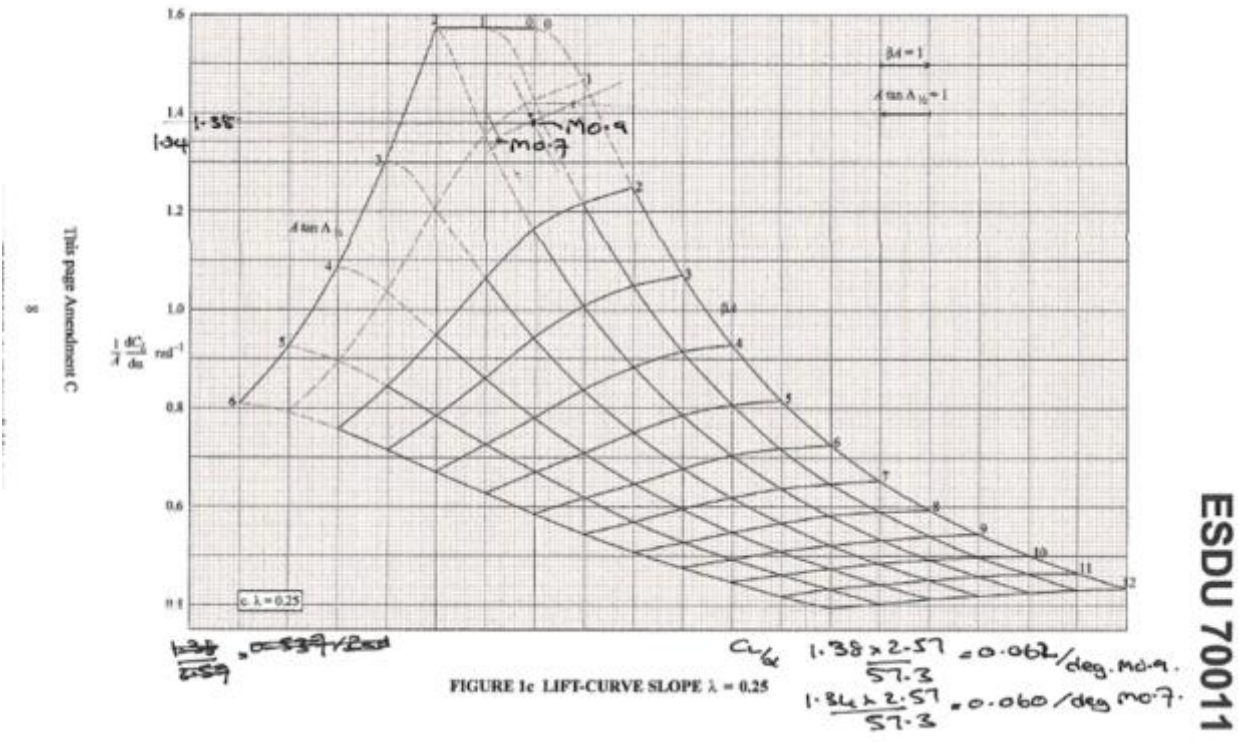


Figure 131. Showing ESDU plot to determine canard lift curve rate at M0.7 and M 0.9

Canard wing sizing (out of ground effect)				
design deflection (degrees nose down)				
wing lift coefficient/degree	0.062	using esdu 70011		
target load to produce (kN)	3.99	M0.9		
q	57451	M1.0		
ground effect	no			
mach cone angle (radians)	0.877636	50 degrees		
sweepback angle (degrees)				
root chord (m)	0.37			
tip chord (m)	0.10			
semi -span (m)	0.30	ignores body		
total area (m ²) both sides	0.14			
aspect ratio	2.52			
downforce created per degree (N)	508.58			
deflection required to neutralise drag effect	7.84	degrees		

Figure 132 Showing wing parameters required offsetting moments induced during deceleration

Aussie Invader 5R							
tip cone area . A. (m ²)	0.78		mass (kg)	5500			
Base area (m ²)	1.03						
Mach No	0.6	0.7	0.8	0.9	1	1.1	1.2
dynamic pressure q = 0.5γ*Pa ²	25534	34754	45394	57451	70928	85822	102136
CD (derived from BF)	0.47	0.56	0.63	0.79	1.00	1.19	1.31
CD base drag power off (value from BF)	0.23	0.09	0.26	0.33	0.42	0.32	0.23
Aero Drag (inc. wave) (kN) CdqA	9.33	15.04	22.09	35.56	54.96	79.54	104.40
Base drag (kN)	5.93	3.17	12.13	19.70	30.64	28.60	24.68
Additional Base drag due to airbrake deployment (kN)	12.94	17.61	23.00	29.11	29.34	25.11	15.47
airbrake force (kN)	25.36	36.00	51.64	75.60	82.60	65.20	34.72
Rolling resistance (kN)	4.28	5.72	7.36	9.22	11.32	13.58	16.11
Total drag (kN)	57.84	77.53	116.21	169.17	208.86	212.03	195.37
deceleration (m/s ²)	10.52	14.10	21.13	30.76	37.97	38.55	35.52
AWC moment induced by mass (kNm)	-58.30	-78.15	-117.14	-170.53	-210.53	-213.73	-196.93
Mach No	0.6	0.7	0.8	0.9	1	1.1	1.2
deceleration (g)	1.07	1.44	2.15	3.14	3.87	3.93	3.62

Figure 133. Showing a summary of deceleration calculations

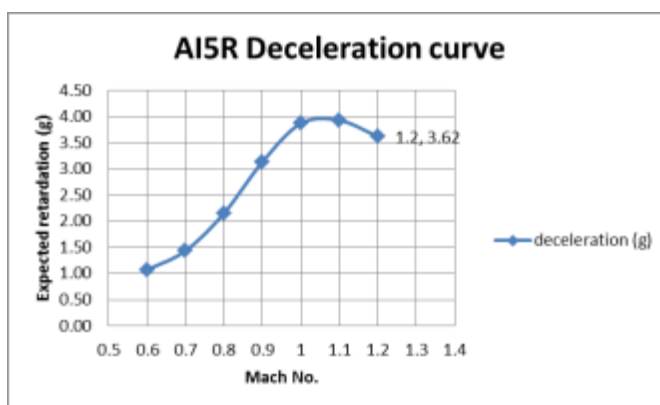


Figure 134 Showing a plot of deceleration (g) expected at various Mach No.

AI5R Time taken to decelerate (s)							
Mach No	0.6	0.7	0.8	0.9	1	1.1	1.2
velocity a=341m/s	205	239	273	307	341	375	409
deceleration a (m/s ²)	10.52	14.10	21.13	30.76	37.97	38.55	35.52
Time to reduce speed by M0.1 interval (s)		2.42	1.61	1.11	0.90	0.88	0.96
cumulative time to decelerate (s)		5.46	3.85	2.74	1.84	0.96	0

Figure 135 Showing estimation of deceleration times.



References.

Gosh, I wish I had written them down as I was doing this work. Good job this isn't a college dissertation, or my old professor would have gone bananas!. I have an extensive library of very old aerodynamics and engineering books I have collected over the years. I do not attempt to pass anything off as my own, though I will modestly take credit for the epiphany when it came to modelling the Gurney based on centreline theory. Most of the work comes from the effort of aerodynamicists in the 50's and 60's. They are the real unsung hero's, with brains the size of planets.

If you have any questions or comments or need to know something specific, fire them across to me at the address below.

Acknowledgements.

Sometimes because of the business of life we forget to say thank you so here goes.

Thank you to;

Karl at Lisa who is so modest he didn't want thanking, but is always there to answer my questions at what are ridiculous times of the day for him.

Jonathan Cassey, who was at the ready to help me out when my NetGen meshing software just wasn't behaving. We finally solved it by saving the Solidworks file as a .stl then ran it through an earlier version of Gmsh before importing into Lisa to create the model. Convolutated I know, but it worked.

Ricard Keller, you have shared so much about the Blue Flame to so many, and have always been willing to help. If it weren't for you, the work that I had been doing that led to Appendix A would have been impossible.

Mark Chapman, Chief Engineer on the Bloodhound project. Despite being immensely busy, he is never more than a phone call away.

Peter Taylor, who is suspect gets lumbered with doing the "mud flap" sketches I ask from time to time. Without them, I would stop dead in my tracks.

Brett Boughton, who despite having a new love in his life, has taken the time to read the daft versions, has asked many good questions and is great to throw ideas across to. You help me see the wood when trees surround me.

Rosco McGlashan, because without you this venture wouldn't happen and there wouldn't be anything to keep me out of mischief!

If I forgot anyone, please let me know, it's a result of my error not lack of appreciation, and I will add you to this list

Many thanks

Paul Martin